

# Revisiting Seismic Energy of Shallow Tremors: Amplifications due to Site and Propagation Path Effects Near the Nankai Trough

Shunsuke Takemura<sup>1</sup>, Kentaro Emoto<sup>2</sup>, and Suguru Yabe<sup>3</sup>

<sup>1</sup>Earthquake Research Institute, the University of Tokyo

<sup>2</sup>Kyushu University

<sup>3</sup>Geological Survey of Japan, National Institute of Advanced Industrial Science and Technology (AIST)

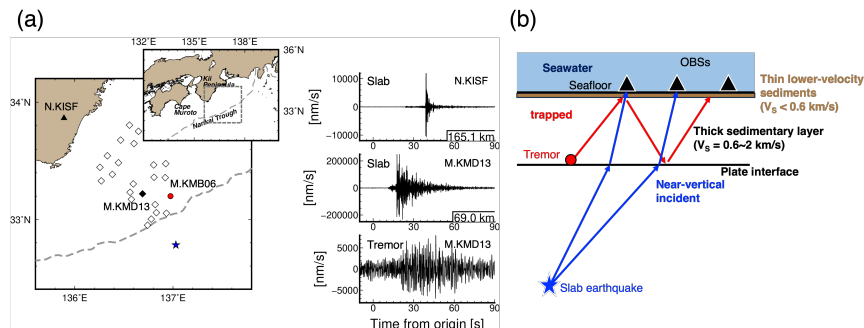
April 12, 2024

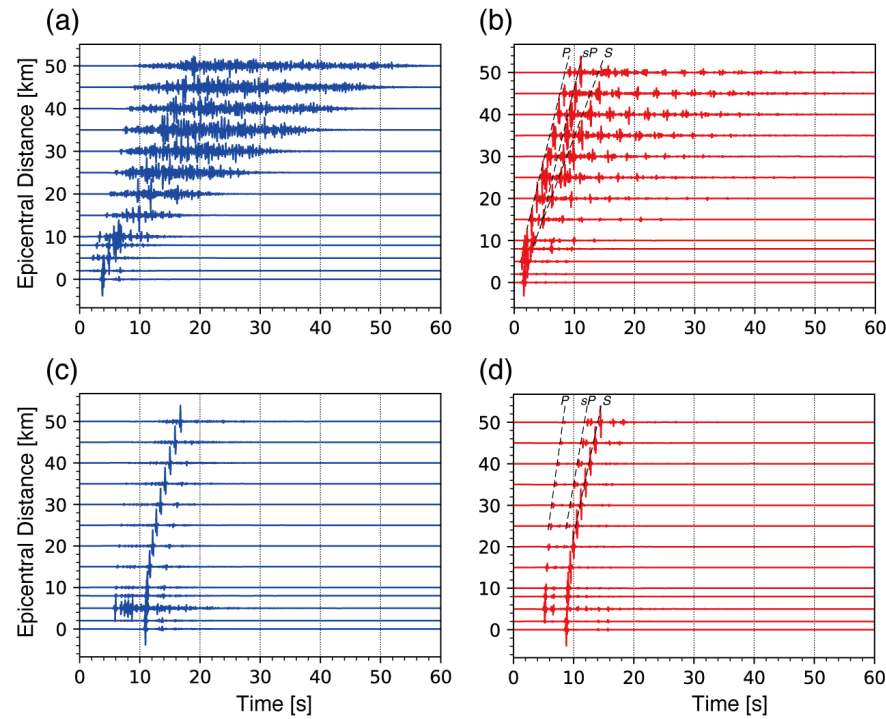
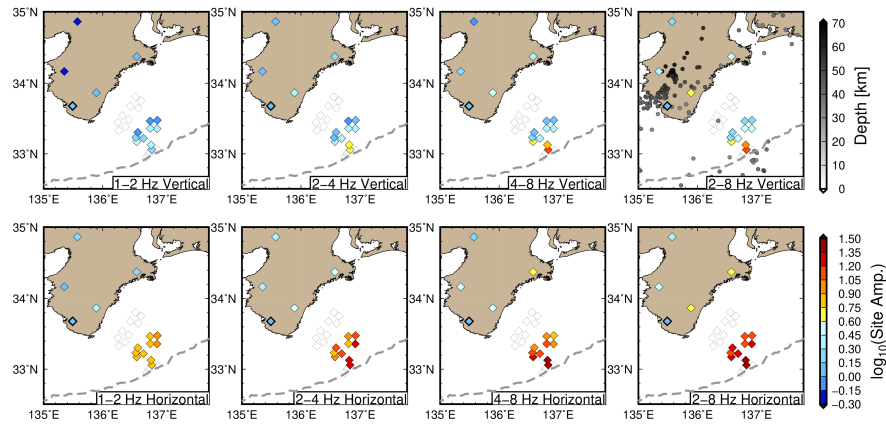
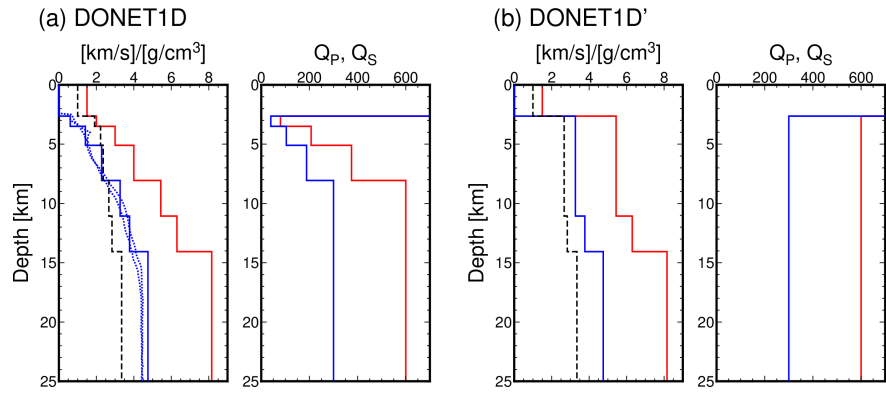
## Abstract

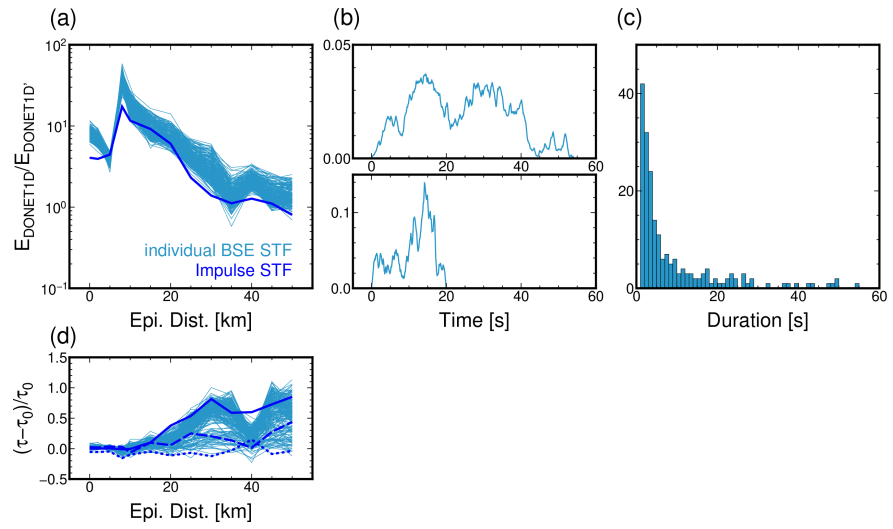
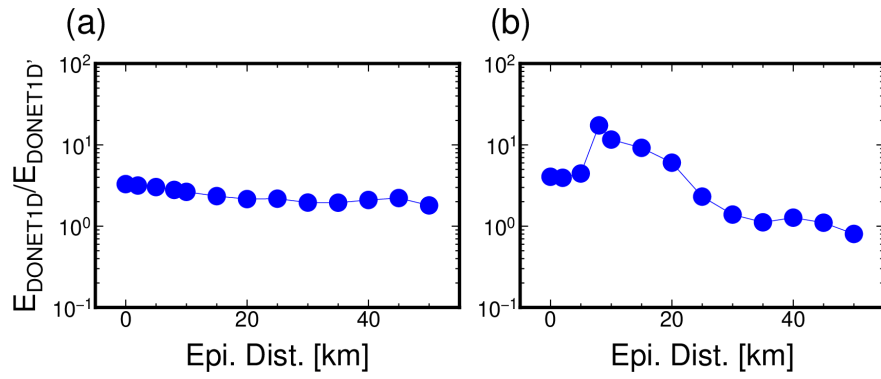
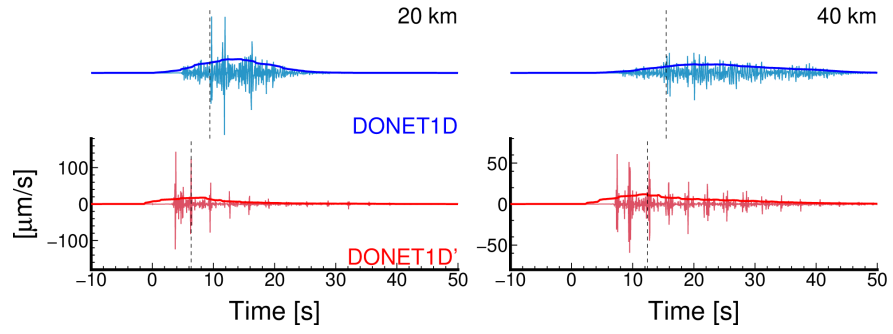
We investigated the effects of the propagation path and site amplification of shallow tremors along the Nankai Trough. Using far-field S-wave propagation from intraslab earthquake data, the amplification factors at the DONET stations were 5–40 times against an inland outcrop rock site. Thick (~5 km) sedimentary layers with VS of 0.6–2 km/s beneath DONET stations have been confirmed by seismological studies. To investigate the effects of thick sedimentary layers, we synthesized seismograms of shallow tremors and intraslab earthquakes at seafloor stations. The ratios of the maximum amplitudes from the synthetic intraslab seismograms between models with and without thick sedimentary layers were 1–2. This means that the estimated large amplifications are primarily controlled by thin lower-velocity (< 0.6 km/s) sediments just below the stations. Conversely, at near-source ([?] 20 km) distances, 1-order amplifications of seismic energies for a shallow tremor source can occur due to thick sedimentary layers. Multiple S-wave reflections between the seafloor and plate interface are contaminated in tremor envelopes; consequently, seismic energy and duration are overestimated. If a shallow tremor occurs within underthrust sediments, the overestimation becomes stronger because of the invalid rigidity assumptions around the source region. After 1-order corrections of seismic energies of shallow tremors along the Nankai Trough, the scaled energies of seismic slow earthquakes were 10<sup>-10</sup>–10<sup>-9</sup> irrespective of the region and source depth. Hence, the physical mechanisms governing seismic slow earthquakes can be the same, irrespective of the region and source depth.

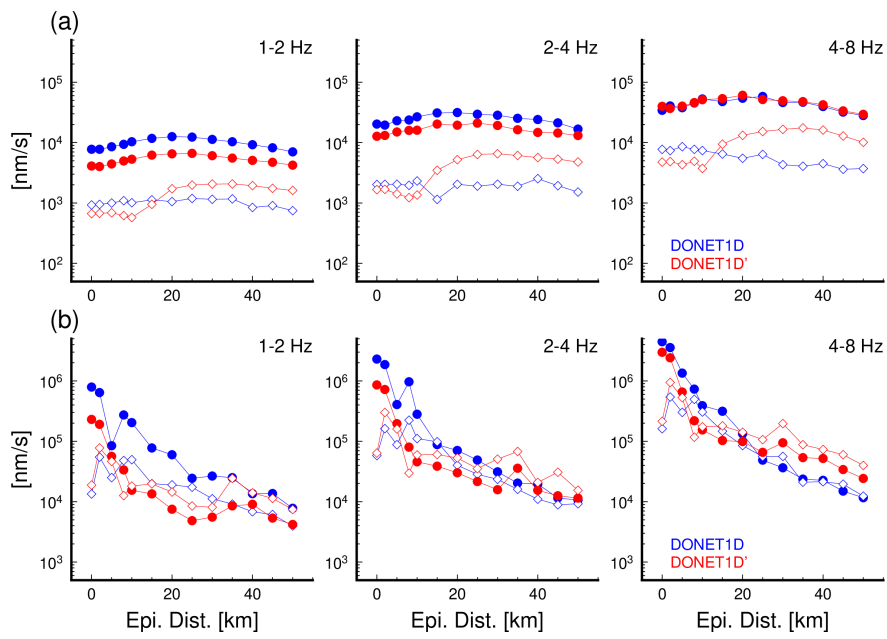
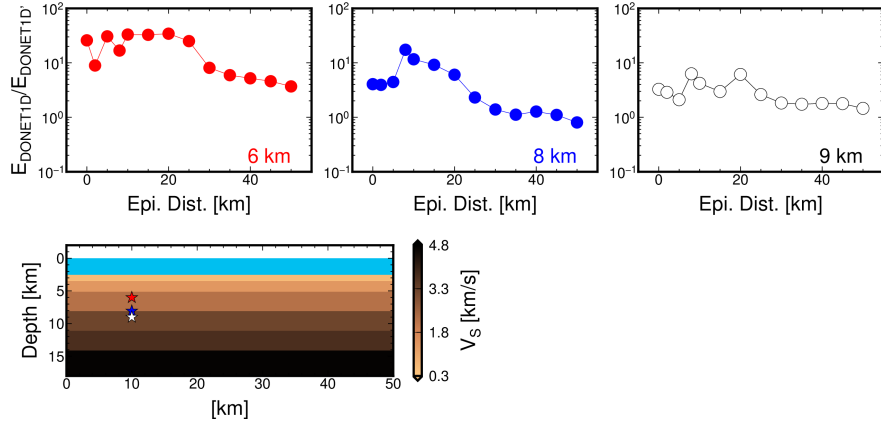
## Hosted file

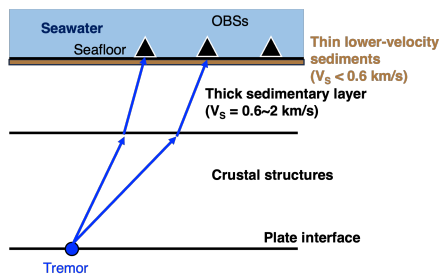
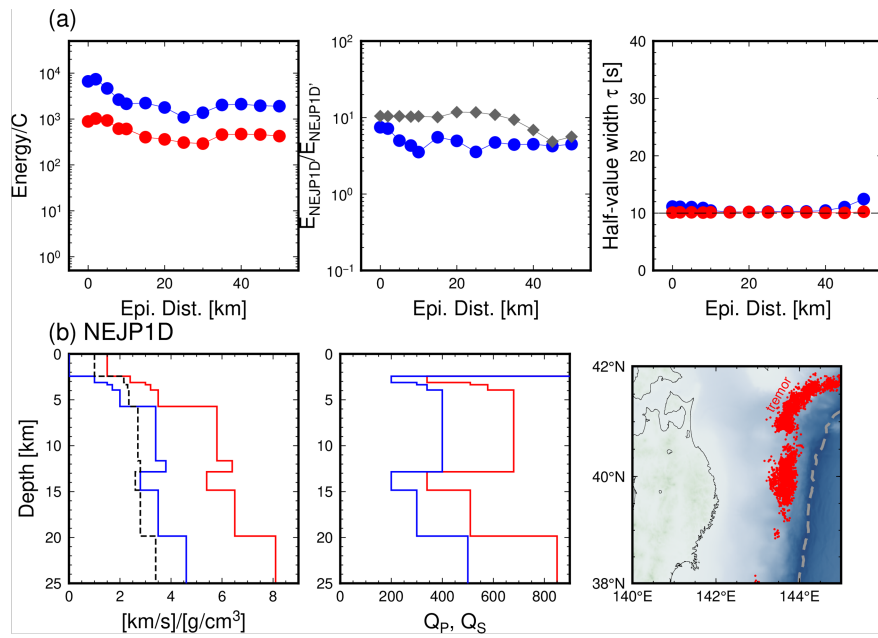
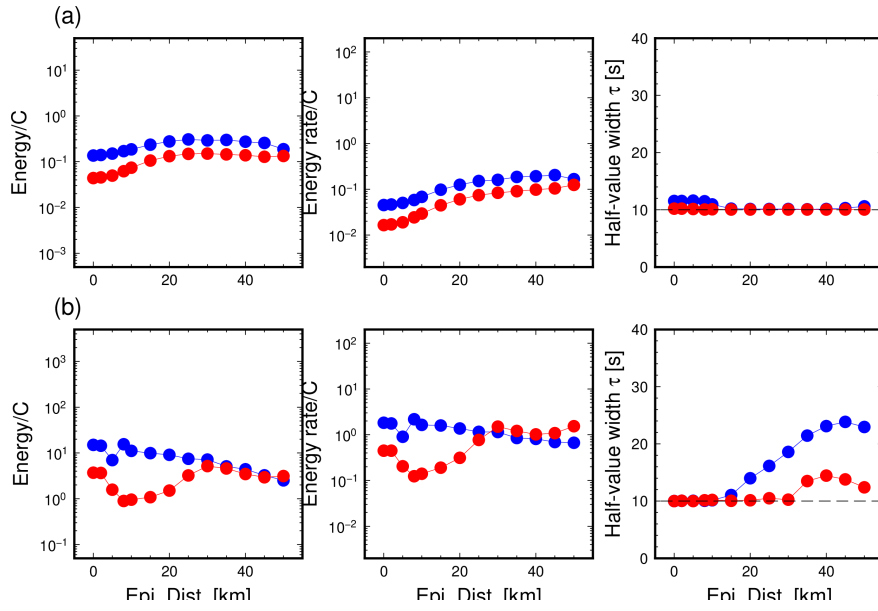
2023\_TakemuraEmotoYabe\_JGR\_R1\_v2\_clean.docx available at <https://authorea.com/users/539748/articles/735245-revisiting-seismic-energy-of-shallow-tremors-amplifications-due-to-site-and-propagation-path-effects-near-the-nankai-trough>

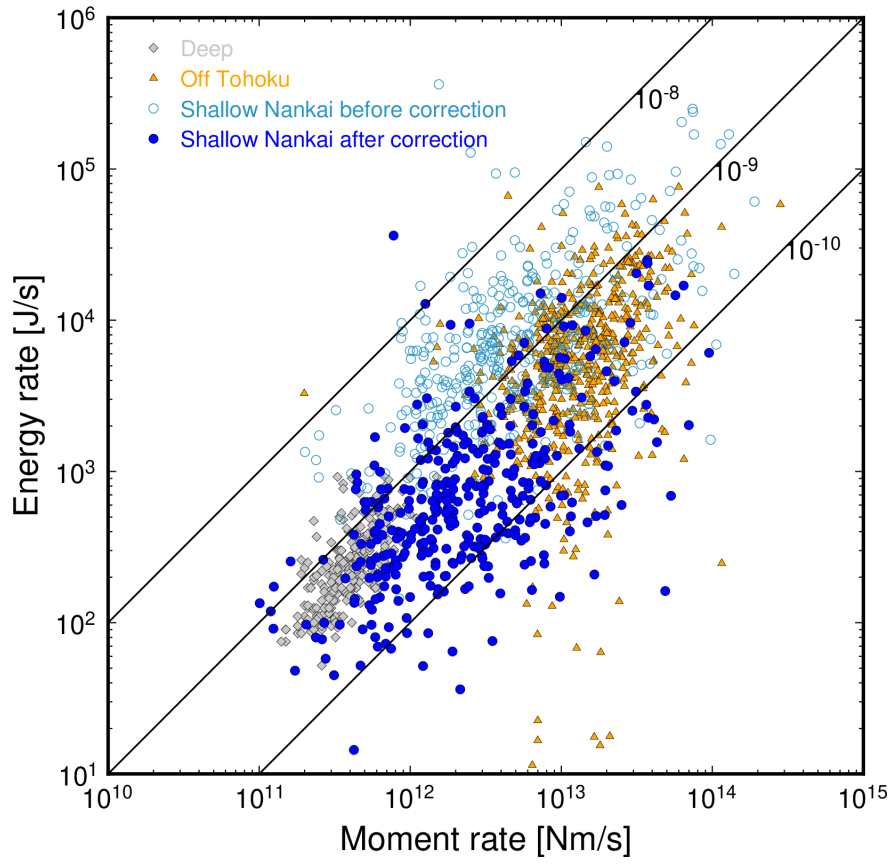












1  
2  
3 **Revisiting Seismic Energy of Shallow Tremors: Amplifications due to Site and**  
4 **Propagation Path Effects Near the Nankai Trough**  
5

6 **Shunsuke Takemura<sup>1</sup>, Kentaro Emoto<sup>2</sup>, and Suguru Yabe<sup>3</sup>**

7 <sup>1</sup> Earthquake Research Institute, the University of Tokyo, 1-1-1 Yayoi, Bunkyo-ku, Tokyo 113-  
8 0032, Japan

9 <sup>2</sup> Geophysics, Graduate School of Science, Tohoku University, 6-3, Aramaki-aza-aoba, Aoba-ku,  
10 Sendai 980-8578, Japan

11 <sup>3</sup> Geological Survey of Japan, National Institute of Advanced Industrial Science and Technology,  
12 Tsukuba Central 7, 1-1-1 Higashi, Tsukuba, Ibaraki 305-8567, Japan

13  
14 Corresponding author: Shunsuke Takemura ([shunsuke@eri.u-tokyo.ac.jp](mailto:shunsuke@eri.u-tokyo.ac.jp))  
15  
16

17 **Key Points:**

- 18 • Effects of path and site on the seismic energy estimation of slow earthquakes at shallow  
19 plate boundaries were investigated.
- 20 • The assumption of far-field body waves without thick sediments causes an  
21 overestimation of seismic energies for shallow tremors.
- 22 • Scaled energies of seismic slow earthquakes at both shallow and large depths range from  
23  $10^{-10}$  to  $10^{-9}$ .  
24  
25

## 26 **Abstract**

27 We investigated the effects of the propagation path and site amplification of shallow  
28 tremors along the Nankai Trough. Using far-field *S*-wave propagation from intraslab earthquake  
29 data, the amplification factors at the DONET stations were 5–40 times against an inland outcrop  
30 rock site. Thick (~5 km) sedimentary layers with  $V_S$  of 0.6–2 km/s beneath DONET stations have  
31 been confirmed by seismological studies. To investigate the effects of thick sedimentary layers,  
32 we synthesized seismograms of shallow tremors and intraslab earthquakes at seafloor stations.  
33 The ratios of the maximum amplitudes from the synthetic intraslab seismograms between models  
34 with and without thick sedimentary layers were 1–2. This means that the estimated large  
35 amplifications are primarily controlled by thin lower-velocity (< 0.6 km/s) sediments just below  
36 the stations. Conversely, at near-source ( $\leq 20$  km) distances, 1-order amplifications of seismic  
37 energies for a shallow tremor source can occur due to thick sedimentary layers. Multiple *S*-wave  
38 reflections between the seafloor and plate interface are contaminated in tremor envelopes;  
39 consequently, seismic energy and duration are overestimated. If a shallow tremor occurs within  
40 underthrust sediments, the overestimation becomes stronger because of the invalid rigidity  
41 assumptions around the source region. After 1-order corrections of seismic energies of shallow  
42 tremors along the Nankai Trough, the scaled energies of seismic slow earthquakes were  $10^{-10}$ – $10^{-9}$   
43 irrespective of the region and source depth. Hence, the physical mechanisms governing seismic  
44 slow earthquakes can be the same, irrespective of the region and source depth.

45

## 46 **Plain Language Summary**

47 The deployment of campaigns and permanent ocean bottom seismometers (OBSs) has  
48 enabled us to investigate the activity and physical properties of offshore seismic phenomena. Our  
49 knowledge of offshore subsurface structures is still limited; consequently, many studies have  
50 used conventional analysis methods with the simplest assumptions. Using observed and synthetic  
51 seismograms near the Nankai Trough, we found a limitation in the conventional analysis method  
52 applied to OBS data. Thick sedimentary layers, which have been confirmed by seismological  
53 studies along the Nankai Trough just below the OBSs, cause an approximately 1-order  
54 overestimation of source parameters for seismic phenomena occurring around the shallow plate  
55 boundary. This overestimation may have occurred during the seismic energy estimation of  
56 shallow slow earthquakes in Hikurangi, Costa Rica, and Mexico. After correcting for the effects  
57 of thick sedimentary layers, we found that the scaled energies of seismic slow earthquakes were  
58  $10^{-10}$ – $10^{-9}$  irrespective of the region and source depth. This suggests that the physical  
59 mechanisms governing seismic slow earthquakes can be the same, regardless of region and  
60 source depth.

61

## 62 **1 Introduction**

63 Slow earthquakes, which are intermediate slip modes between ordinary (fast) earthquakes  
64 and stable sliding, are often observed around megathrust zones worldwide (Obara & Kato, 2016).  
65 Ordinary and slow earthquakes are distributed separately along plate boundaries (e.g., Dixon et  
66 al., 2014; Nishikawa et al., 2023; Plata-Martinez et al., 2021; Takemura, Okuwaki, et al., 2020;  
67 Vaca et al., 2018). Interactions between megathrusts and slow earthquakes have also been  
68 reported in various regions (e.g., Baba et al., 2020; Kato et al., 2012, 2016; Vaca et al., 2018;

69 Voss et al., 2018). Therefore, the activity patterns and physical mechanisms of slow earthquakes  
70 have been studied. Slow earthquakes obey a scaling law that differs from that of ordinary  
71 earthquakes (Ide et al., 2007; Ide & Beroza, 2023). Thus, slow earthquakes may be controlled by  
72 physical mechanisms that are different from those of ordinary earthquakes. Slow earthquakes can  
73 be observed in the seismic and geodetic data. In this study, we focused on slow earthquakes  
74 detected by seismometers, called “seismic slow earthquakes.” Because of noise signals at  
75 microseism (0.1–1 Hz) bands, seismic slow earthquakes appear separately in the 0.01–0.1 and 1–  
76 10 Hz bands. The lower- and higher-frequency seismic slow earthquakes are referred to as very  
77 low-frequency earthquakes (VLFs) and low-frequency earthquakes (LFEs), respectively.  
78 Tremors can be considered successive occurrences of LFEs (Brown et al., 2009; Ide, 2021;  
79 Shelly et al., 2007). Swarms of LFEs/tremors and VLFs during geodetic slow earthquakes  
80 (slow slip events) have often been observed (e.g., Bartlow et al., 2011; Itoh et al., 2022; Obara et  
81 al., 2004; Rogers & Dragert, 2003). The observed characteristics of slow earthquakes in various  
82 subduction zones have been summarized in review papers (Beroza & Ide, 2011; Tomoaki  
83 Nishikawa et al., 2023; Obara, 2020; Obara & Kato, 2016; Schwartz & Rokosky, 2007).

84 The source parameters of seismic slow earthquakes have been extensively studied  
85 worldwide to discuss their physical characteristics. The seismic moments of seismic slow  
86 earthquakes can be obtained from an analysis of the VLFE frequency bands (Ide & Yabe, 2014;  
87 Ito et al., 2009; Maury et al., 2016, 2018; Sugioka et al., 2012; Takemura, Baba, Yabe, Emoto, et  
88 al., 2022; Takemura, Obara, et al., 2022; Takeo et al., 2010). Because seismograms in the VLFE  
89 bands have lower sensitivity to finer structural heterogeneities and can be easily simulated even  
90 for a three-dimensional (3D) model (e.g., Fichtner et al., 2009; Komatitsch et al., 2002; Maeda et  
91 al., 2017), their estimations are stable for both shallow and deep VLFEs. However, because  
92 seismic wave scattering due to small-scale (< several kilometers) heterogeneities becomes  
93 dominant at frequencies above 1 Hz (Sato et al., 2012), the source parameters of tremors cannot  
94 be deterministically estimated using the observed waveforms. Thus, the seismic energies of  
95 tremors have been estimated using smoothed velocity envelopes and the assumption of far-field  
96 body waves in an infinite homogeneous medium (e.g., Annoura et al., 2016; Maury et al., 2018;  
97 Wech, 2021; Yabe & Ide, 2014). The scaled energy, which is the ratio of the seismic energy to  
98 the seismic moment, characterizes the dynamics of earthquake faulting (Kanamori & Rivera,  
99 2006). Owing to the observational gap of an intermediate (0.1–1 Hz) frequency band, the scaled  
100 energy of seismic slow earthquakes can be calculated as the ratio of the seismic energy of a  
101 tremor/LFE divided by the seismic moment of the accompanying VLFE.

102 Slow earthquakes have been detected in several regions of Japan. Deep slow earthquakes  
103 occur at depths of 30–40 km depth, near the interface of the subducted Philippine Sea Plate.  
104 These signals were observed in the inland seismic networks Hi-net and F-net (Aoi et al., 2020;  
105 National Research Institute for Earth Science and Disaster Resilience, 2019c, 2019b). The  
106 observed seismic moment rates of the deep VLFEs and the energy rates of the deep tremors are  
107 in the range of  $10^{11}$ – $10^{12}$  Nm/s and  $10^1$ – $10^3$  J/s, respectively. The scaled energy of deep slow  
108 earthquakes ranges from  $10^{-10}$  to  $10^{-9}$  (Ide et al., 2008; Ide & Maury, 2018; Ide & Yabe, 2014),  
109 significantly less than that of ordinary earthquakes (approximately  $3 \times 10^{-5}$ ; Ide & Beroza, 2001).  
110 Such a 4-order difference in the scaled energy between ordinary and slow earthquakes also  
111 suggests different governing mechanisms for both slip phenomena.

112 Permanent networks of ocean bottom seismometers (OBSs) have been in development  
113 since 2010 (see Aoi et al., 2020; National Research Institute for Earth Science and Disaster

114 Resilience, 2019a, 2019d). These networks enable us to investigate the source properties of  
115 shallow VLFs and tremors near the Nankai Trough and Japan Trench. The depths of shallow  
116 seismic slow earthquakes are  $\leq 10$  and 10–20 km, respectively. High-frequency seismograms at  
117 OBSs contain large site amplifications due to the low-velocity sediments beneath the OBSs.  
118 Figure 1a shows sample waveforms at the offshore DONET (M.KMD13) and inland F-net  
119 (N.KISF) stations during an intraslab earthquake. After correcting for the geometrical spreading  
120 of the body waves, the maximum amplitude at M.KMD13 was still approximately eight times  
121 larger than that at N.KISF. This was due to site amplification at M.KMD13.

122 Site amplification factors for an inland rock site have been estimated to accurately  
123 estimate the physical properties of offshore earthquake phenomena using OBSs. Because the  
124 signals of shallow tremors are too weak at inland rock sites (see Figure 1 of Takemura, Hamada,  
125 et al., 2023), site amplifications are typically estimated based on near-vertical incident body  
126 waves from intraslab earthquakes (blue arrows in Figure 1b). Although vertical *S*-wave  
127 amplitudes at OBSs tend to be weakly amplified, amplification factors of 5–30 against an inland  
128 rock site in horizontal components have been observed in previous studies (Kubo et al., 2018,  
129 2020; Takemura, Emoto et al., 2023; Yabe et al., 2019). *S*-wave energy is generally dominant in  
130 horizontal components. These site amplification factors include the effects of thick sedimentary  
131 layers with  $V_S$  of 0.6–2 km/s and thin sediments of  $V_S < 0.6$  km/s just below OBSs (see Figure  
132 1b). Thick sedimentary layers beneath the DONET stations have been confirmed in  
133 seismological studies (e.g., Akuhara et al., 2020; Kamei et al., 2012; Tonegawa et al., 2017). The  
134 resolutions of sedimentary layers estimated based on seismological methods are several hundred  
135 meters. Thus, thicknesses of unmodeled thin lower-velocity ( $V_S < 0.6$  km/s) sediments may be  
136 less than several hundred meters. Although the propagation paths between intraslab earthquakes  
137 and shallow tremors were expected to be significantly different (Figure 1b), the obtained site  
138 amplifications were used in site corrections for shallow tremor waveforms. After site corrections,  
139 the seismic energies of the shallow tremors were obtained in the same manner as those of the  
140 deep tremors (Nakano et al., 2019; Tamaribuchi et al., 2022; Yabe et al., 2019, 2021). The  
141 seismic energy rates of the shallow tremors range from  $10^3$  to  $10^6$  J/s. The scaled energies of  
142 shallow tremors exhibited regional differences:  $10^9$ – $10^8$  off Cape Muroto and southeast of the  
143 Kii Peninsula and  $10^{10}$ – $10^9$  off the Kii Channel and along the Japan Trench. Although these  
144 values are similar to those of deep slow earthquakes, there is a depth difference in the scaled  
145 energies (0–1 order difference) beneath and off the Kii Peninsula. This depth difference in scaled  
146 energy could be considered a result of differences in temperature and pressure at shallow ( $< 150$   
147  $^{\circ}\text{C}$ ,  $< 0.2$  GPa) and deep ( $> 300$   $^{\circ}\text{C}$ , 1 GPa) depths (Yabe et al., 2019).

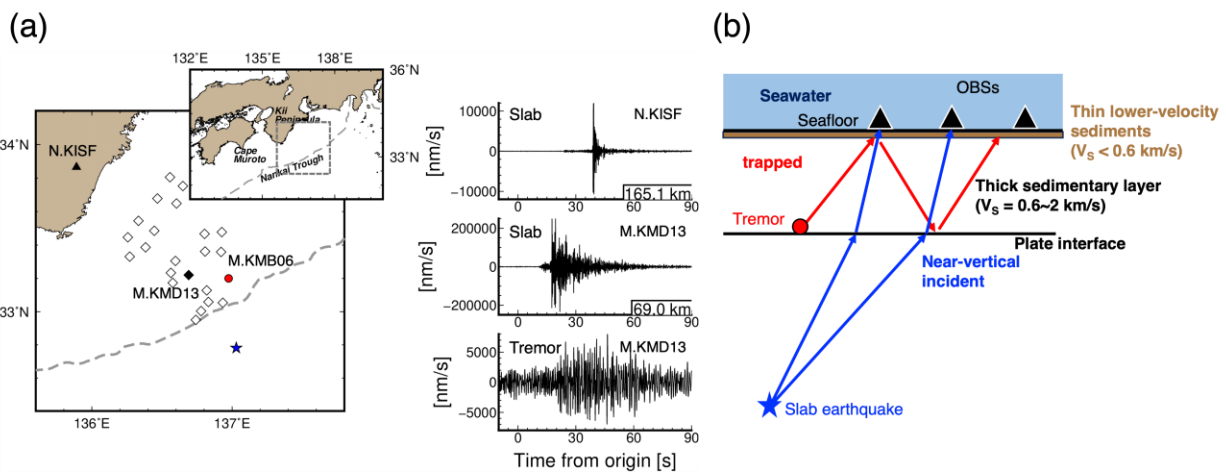
148 Recent numerical studies have revealed that the characteristics of high-frequency seismic  
149 waves around shallow plate boundaries are complicated because of thick low-velocity  
150 sedimentary layers (Takemura, Emoto, et al., 2023; Takemura, Yabe, et al., 2020). The bottom-  
151 right panel of Figure 1a shows a sample waveform of a shallow tremor. This long-duration and  
152 spindle-shaped envelope is caused not only by complicated long-duration moment rate functions  
153 but also by envelope broadening due to the thick sedimentary layer in this region. This envelope  
154 broadening can be significant if seismic sources are located just below thick sedimentary layers.  
155 Typical ordinary earthquakes tend to occur at deeper depths, and thus envelope broadening due  
156 to thick sedimentary layers becomes weak. Observations of shallow slow earthquakes are still  
157 limited in the world (summarized in Takemura, Hamada, et al., 2023), but similar phenomena  
158 can be expected in near-source OBS observations within Nankai, Mexico, Costa Rica and  
159 Hikurangi subduction zones. In these regions, shallow tremors often occur at shallower ( $\leq 10$

160 km) depths (e.g., Baba et al., 2021; Plata-Martinez et al., 2021; Tamaribuchi et al., 2022; Todd et al., 2018). However, the latter effects have yet to be incorporated into conventional methods of seismic energy estimation.

163 In this study, to better understand seismic slow earthquakes at shallow depths, we investigated the effects of thick sedimentary layers on high-frequency seismic waves at OBSs using both observed DONET and synthetic seismograms. The Results section first provides us site amplifications at DONET stations estimated via the conventional method using observed intraslab earthquakes. These site amplifications could include both effects of thick low-velocity and thin lower-velocity sediments. We synthesized high-frequency seismograms at the OBSs from an intraslab earthquake and a shallow tremor using a wavenumber integration program code and local one-dimensional (1D) velocity models. The shallow tremors along the Nankai Trough occur around the basement of thick sedimentary layers (approximately 8km), while intraslab earthquakes tend to be located at depths of 20-40 km. We investigated the depth-dependent propagation path effects of thick sedimentary layers using synthetic seismograms with and without thick sedimentary layers. Synthetic seismograms clearly demonstrate differences in amplifications due to path effects owing to source depth. A comparison between the estimated site amplifications from observations and the effects of thick sedimentary layers from synthetics provided the major cause of the site amplifications at OBSs. We then evaluated the amplification of seismic energies for shallow tremors caused by thick sedimentary layers.

179 In Discussions section, we discuss seismic energy amplifications due to an invalid assumption of heterogeneities around the seismic source. The precise determination of the source depths of shallow slow earthquakes remains challenging, but the rigidity in seismic energy estimation has been typically assumed to 33 GPa as the crustal property. Seismic and scaled energies of seismic slow earthquakes were estimated in various regions of Japan. Based on the resultant seismic energy amplifications of shallow tremors, we revisited the scaled energies of seismic slow earthquakes in Japan.

186  
187



188

189 **Figure 1.** (a) Examples of high-frequency seismograms at offshore (M.KMD13) and inland  
190 (N.KISF) stations. The upper and middle right panels are high-frequency (> 1 Hz) EW-

191 component seismograms during an intraslab earthquake, which occurred at a depth of 39 km at  
 192 3:19 on May 22, 2020 (JST). The right bottom panel shows a high-frequency (> 1 Hz) EW-  
 193 component seismogram during a shallow tremor, which occurred at 10:19 on December 12, 2020  
 194 (JST). The blue star and red circle represent epicenters of an intraslab earthquake and a shallow  
 195 tremor, respectively. (b) Schematic illustration of propagation paths from seismic sources to  
 196 OBSs southeast of the Kii Peninsula region.

197

## 198 **2 Data and Methods**

199 We used continuous velocity seismograms recorded at the DONET (National Research  
 200 Institute for Earth Science and Disaster Resilience, 2019a) and F-net (National Research Institute  
 201 for Earth Science and Disaster Resilience, 2019b) stations. Almost of F-net broadband  
 202 seismometers were deployed at outcrop rock sites; thus, F-net data can be used as a reference for  
 203 site correction. Takemoto et al. (2012) pointed out that the characteristics of S-wave  
 204 amplifications are similar at all F-net stations for various frequency ranges. Each DONET node  
 205 contains four to five seismic stations. Detailed information on both the networks is available in  
 206 Aoi et al. (2020). We did not use the M.KMA and KME nodes because of their distances from  
 207 the shallow tremor sources. We also did not use unburied DONET stations (KMC11 and  
 208 KMC12). To estimate the site amplifications at the DONET stations, we used data from 140  
 209 intraslab earthquakes that occurred from April 2016 to December 2022. The origin time,  
 210 hypocenter locations, and magnitudes were obtained from a unified hypocenter catalog provided  
 211 by the Japan Meteorological Agency (JMA). The JMA magnitudes ranged 3.0–5.1. We measured  
 212 the maximum S-wave amplitudes at the F-net and DONET stations. We estimated the site  
 213 amplification factors of the DONET stations based on the method by Yabe et al. (2019).  
 214 Assuming far-field body wave propagation in a homogeneous media, the S-wave amplitude at  
 215 the  $j$ -th station from the  $i$ -th intraslab earthquake can be expressed as follows:

$$\ln(A_{ij}) = \ln(S_i) - \ln(\sqrt{4\pi}R_{ij}) - \alpha R_{ij} + \ln(G_j) \#(1)$$

216 where  $S_i$  is a source term,  $R_{ij}$  is hypocentral distance,  $\alpha$  is the attenuation factor of  $\pi f/QV_S$ ,  
 217 and  $G_j$  is a site amplification factor at the  $j$ -th station. We set the site amplification factor of the  
 218 N.KMTF to 1. This equation can then be solved using the least-square method.

219 We synthesized seismograms assuming a 1D velocity structure model to investigate the  
 220 propagation path effects near the Nankai Trough. The 1D  $P$ -wave model around the DONET  
 221 stations by Nakano et al. (2013) was used. The S-wave velocity, density, and anelastic  
 222 attenuation were obtained by assuming the empirical laws proposed by Brocher (2005, 2008).  
 223 We named this model “DONET1D” (Figure 2a). In DONET1D, the interface of the Philippine  
 224 Sea Plate is located at a depth of 8.07 km. DONET1D agreed with the 1D S-wave velocity  
 225 models beneath M.KMB06 and M.KMD13 by Tonegawa et al. (2017) (blue dashed lines in  
 226 Figure 2a). Thick (~5 km) sedimentary layers with  $V_S$  of 0.6–2.3 km/s exist beneath M.KMB and  
 227 M.KMD. Using the local 3D model, Takemura, Yabe et al. (2020) and Takemura, Emoto, et al.  
 228 (2023) demonstrated that the major cause of complicated high-frequency seismic wave  
 229 propagation southeast off the Kii Peninsula is thick sedimentary layers, rather than other  
 230 heterogeneities (such as bathymetry, the subducted Philippine Sea Plate, seawater, and small-  
 231 scale velocity heterogeneities). In addition, shallow tremors and VLFE epicenters are located  
 232 around the M.KMB and M.KMD nodes (Nakano et al., 2018; Takemura, Obara, et al., 2022;

233 Tamaribuchi et al., 2022; Yamamoto et al., 2022). Thus, modeling using DONET1D can provide  
 234 the average characteristics of high-frequency seismic wave propagation within shallow tremor  
 235 regions along the Nankai Trough.

236 To investigate the effects of thick sedimentary layers, we prepared another 1D model,  
 237 DONET1D' (Figure 2b) in which the physical parameters of the sedimentary layers were  
 238 replaced with those of the oceanic crust. The Green's functions using both 1D models can be  
 239 evaluated by employing the wavenumber integral calculations using the open-source code  
 240 "Computer programs in Seismology" (CPS; Herrmann, 2013). The seismic sources were  
 241 assumed to be a low-angle thrust mechanism (strike/dip/rake = 270°/10°/90°) at a depth of 8.07  
 242 km and a normal fault mechanism (strike/dip/rake = 300°/45°/-120°) at a depth of 40 km. These  
 243 are the typical mechanisms of shallow tremors and intraslab earthquakes in this region. Seismic  
 244 moment  $M_0$  was fixed at  $3.98 \times 10^{13}$  Nm (moment magnitude  $M_w$  3.0).

245 We also simulated seismic wave propagation within the same models using the open-  
 246 source finite-difference method code OpenSWPC (Maeda et al., 2017) to obtain high-frequency  
 247 seismic wave propagation in 3D volumes. The 3D simulation model covered  $105 \times 30 \times 75$  km<sup>3</sup>  
 248 and was discretized using a uniform grid of 0.015 km. We employed a perfectly matched layer  
 249 boundary condition to reduce artificial reflections from the model boundaries. The 64-s seismic  
 250 wave propagation was calculated using 80,000 time steps. In the OpenSWPC simulations, to  
 251 obtain stable and accurate seismic wave propagation in 3D media, we assumed a single-cycle  
 252 Küpper wavelet with a duration of 0.25 s rather than an impulse source time function (STF) to  
 253 reduce numerical instability. Short-duration STFs were assumed in both CPS and OpenSWPC  
 254 synthetics. The simplest tests with a short-duration test can represent seismic wave propagation  
 255 from a shallow LFE source. Although short-duration seismic slow earthquakes have recently  
 256 been reported (Toh et al., 2023), this assumption may be invalid for realistic tremor synthetics.  
 257 Therefore, we examined the effects of complicated STFs using the Brownian slow earthquake  
 258 (BSE) model (Ide, 2008; Ide & Maury, 2018).

259 Using theoretical  $S$ -wave traveltimes ( $T_S$ ) in 1D models, we measured the maximum  $S$ -  
 260 wave amplitudes for each filtered velocity seismogram from times starting at  $T_S-1$  to reduce the  
 261 effects of the zero-phase Butterworth filter. The seismic energies were calculated using  
 262 smoothed velocity envelopes as a typical tremor analysis. We could not identify  $P$  and  $S$  phases  
 263 from the spindle-shape tremor waveforms (Figure 1a). First, we applied a bandpass filter with  
 264 passed frequencies of 2–8 Hz, which are typically used in seismic energy estimations for  
 265 tremors/LFEs. The vector sum of the three-component envelopes was calculated. A 5-s moving  
 266 average was applied to obtain smooth envelopes. Owing to the lack of clear  $P$ - and  $S$ -wave  
 267 onsets, smoothed envelopes are typically used as  $S$ -waves for the location and energy analyses of  
 268 the tremors. The half-value width,  $\tau(t_2-t_1)$ , of the smoothed envelope was measured as the  
 269 source duration. The normalized seismic energy  $E_{ij}/C_{ij}$  at the  $j$ -th station was calculated using the  
 270 following equation:

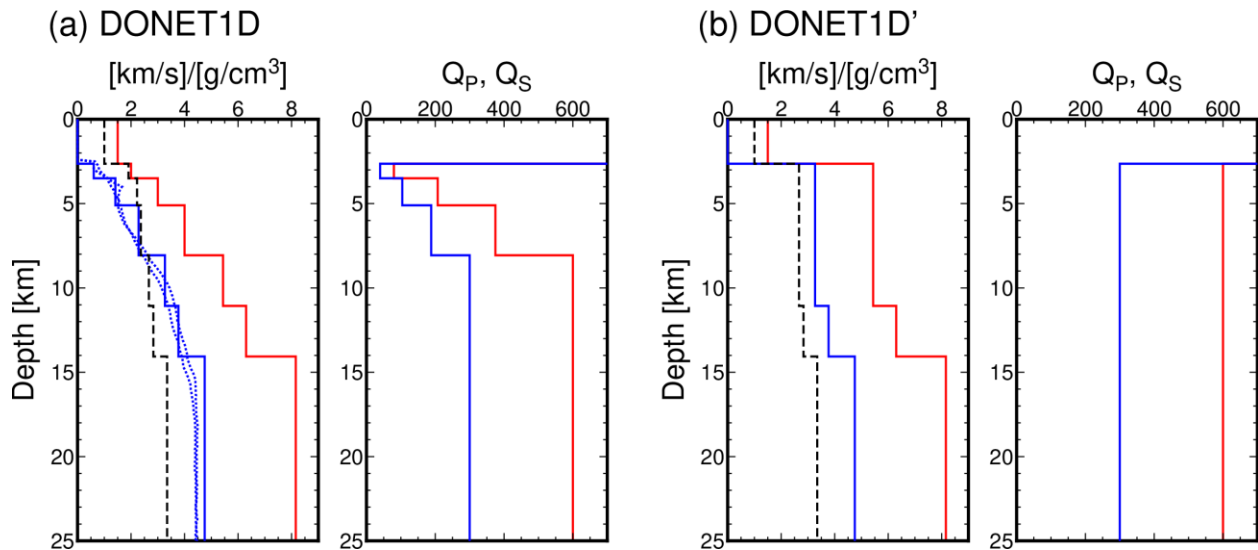
$$\frac{E_{ij}}{C_{ij}} = R_{ij}^2 \int_{t_1}^{t_2} v^2(t) dt \quad \#(2)$$

271 where  $R_{ij}$  is the hypocentral distance from the  $i$ -th source to the  $j$ -th receiver. The  $t_2$  and  $t_1$   
 272 are times of half-value width starting and ending, respectively. The constant,  $C$ , is expressed as  
 273 follows:

$$C_{ij} = 2\pi\rho V_S \exp\left(\frac{2f_c Q^{-1} R_{ij}}{V_S}\right) \#(3)$$

274 where  $V_S$  is the  $S$ -wave velocity,  $\rho$  is density  $f_c$  is the central frequency, and  $Q$  is a quality factor.  
 275 In previous studies,  $V_S$  and  $\rho$  were typically fixed as 3.5 km/s and 2.7 g/cm<sup>3</sup>, respectively. These  
 276 values are based on the assumption of far-field body wave propagation in an infinite  
 277 homogeneous medium with a rigidity of 33 GPa. The effects of the source radiation pattern were  
 278 also neglected because of high-frequency seismic wave propagation at regional distances  
 279 (Takemura et al., 2009, 2016; Takemura, Yabe, et al., 2020; Trugman et al., 2021). We evaluated  
 280  $E_{ij}/C_{ij}$  for DONET1D and DONET1D' because  $C_{ij}$  became common at stations with the same  
 281 distances. The estimated  $Q$  at 2–8 Hz was approximately 800 (results shown in the next section)  
 282 and was not dominant in the energy estimation.

283



284

285 **Figure 2.** Assumed 1D velocity structure models. (a) DONET1D model constructed from the 1D  
 286  $P$ -wave model of Nakano et al. (2013) and empirical laws of velocity structures (Brocher, 2005,  
 287 2008). (b) DONET1D', where physical parameters within sedimentary layers are replaced with  
 288 those within the oceanic crust. The red and blue colors represent  $P$ - and  $S$ -waves, respectively.  
 289 The dashed lines are density as a function of depth. The blue dotted lines in (a) are  $S$ -wave  
 290 velocity models beneath M.KMB06 and M.KMD13 (locations shown in the map of Figure 1a)  
 291 by Tonegawa et al. (2017).

292

## 293 3 Results

### 294 3.1. Site amplifications at DONET OBSs based on the conventional method

295 Figure 3 shows the estimated site amplification factors at the F-net and DONET stations.  
 296 Both vertical and horizontal site amplifications at N.KMTF (bold diamonds) were fixed as 1. We  
 297 estimated the site amplifications of the 1–2, 2–4, and 4–8 Hz frequency bands. We additionally  
 298 estimated those at frequencies of 2–8 Hz because the analysis of tremor signals is typically

299 performed using this frequency band. Our site amplification factors agree well with those in  
 300 previous studies (Kubo et al., 2018; Yabe et al., 2019). The amplification factors of the  
 301 horizontal component range from 5 to 40, while those of the vertical component range from 0.5  
 302 to 3, except for the stations near the Nankai Trough. Differences between the horizontal and  
 303 vertical components were also reported for the *S*-wave coda H/V ratio by Takemura et al. (2023).  
 304 The estimated *Q* values at 1–2, 2–4, 4–8, and 2–8 Hz were 254, 481, 933, and 795, respectively.  
 305 The estimated site amplifications and *Q* values were obtained from the Zenodo repository (see  
 306 “Open Research”).

307

### 308 **3.2. Characteristics of synthetic seismograms with/without thick sedimentary layers**

309 Figure 4 shows the synthetic velocity seismograms of DONET1D and DONET1D'. A  
 310 bandpass filter with frequencies of 2–8 Hz was used. The seismic waves from a shallow tremor  
 311 source were effectively trapped within thick sedimentary layers (Takemura, Yabe, et al., 2020);  
 312 consequently, the onset of the *P*- and *S*-waves became unclear, and strong envelope broadening  
 313 occurred (Figure 4a). In the model without sedimentary layers (Figure 4b), clear *P*- and *S*-wave  
 314 onsets were observed. *sP* converted and multiple reflected waves from the sea surface were  
 315 observed. From Movies S1 and S2, we can confirm the characteristics of the seismic wave  
 316 propagation mentioned above. Reverberations within the sedimentary and seawater layers were  
 317 clearly imaged in the simulated wavefield (Movie S1). However, we could not recognize  
 318 individual phases from the results of DONET1D (Figure 4a). For a slab earthquake source  
 319 (Figure 4c, d), although the traveltimes of the *P*- and *S*-waves were delayed because of the thick  
 320 sedimentary layer, *P* and *S* wavetrains were clearly identified in both models. Movies S3 and S4  
 321 present the seismic wave propagation for intraslab earthquake cases.

322

### 323 **3.3. Amplifications of maximum *S*-wave amplitudes and seismic energies**

324 Examples of the filtered seismograms for a shallow tremor source are shown in the top  
 325 panels of Figure 5. Unclear *P*- and *S*-wave onsets and envelope broadening are observed in  
 326 DONET1D (blue lines). Envelope broadening in the smoothed envelopes of DONET1D (blue  
 327 bold lines in Figure 5) is caused by the contamination of reflected *S*-waves between the seafloor  
 328 and basement of the sedimentary layers (plate interface). These reflected *S*-waves contaminate  
 329 the smoothed tremor envelopes of DONET1D. In DONET1D' (red lines), *P*- and *S*-wave signals  
 330 were clear and impulsive. The reflection phases from the sea surface were repeatedly confirmed  
 331 after *S* arrival. The smoothed envelopes in DONET1D' (red bold lines) contain not only the *S*-  
 332 wave content but also those of *P*- and reflected waves from the sea surface. At an epicentral  
 333 distance of 20 km, the maximum amplitude of the smoothed envelope in DONET1D was several  
 334 times larger than that of DONET1D'. This amplitude difference decreased at a distance of 40  
 335 km; however, the envelope duration in DONET1D remained longer.

336 Figure 6 shows the maximum *S*-wave amplitudes at 1–2, 2–4, and 4–8 Hz for the shallow  
 337 tremor and intraslab earthquake. The blue and red symbols represent the results from DONET1D  
 338 and DONET1D', respectively. For an intraslab earthquake, the differences in the horizontal  
 339 maximum *S*-wave amplitudes between DONET1D and DONET1D' were practically constant  
 340 irrespective of the distance. The differences in an intraslab source between DONET1D and  
 341 DONET1D' decreased with increasing frequency. The ratios of the horizontal maximum *S*-wave

342 amplitudes between DONET1D and DONET1D' were approximately 1–2 at 1–2 and 2–4 Hz,  
343 implying that the observed large horizontal amplifications (Figure 3) were mostly caused by thin  
344 lower-velocity ( $V_S < 0.6$  km/s) sediments just below the DONET stations (brown areas in Figure  
345 1b). These distance-independent differences can easily be corrected using the estimated site  
346 amplification factors from a method assuming far-field *S*-wave propagation. However,  
347 complicated differences in the maximum *S*-wave amplitudes between the models appeared for a  
348 shallow tremor source (Figure 6b). At 1–2 and 2–4 Hz, the horizontal *S*-wave amplitudes were  
349 2–13 times amplified at distances of 5–20 km (near-source OBSs). The differences in horizontal  
350 *S*-wave amplitudes also decreased with increasing frequency and distance. The effects of thick  
351 sedimentary layers on the maximum *S*-wave amplitudes for shallow tremors and intraslab  
352 earthquakes differed completely.

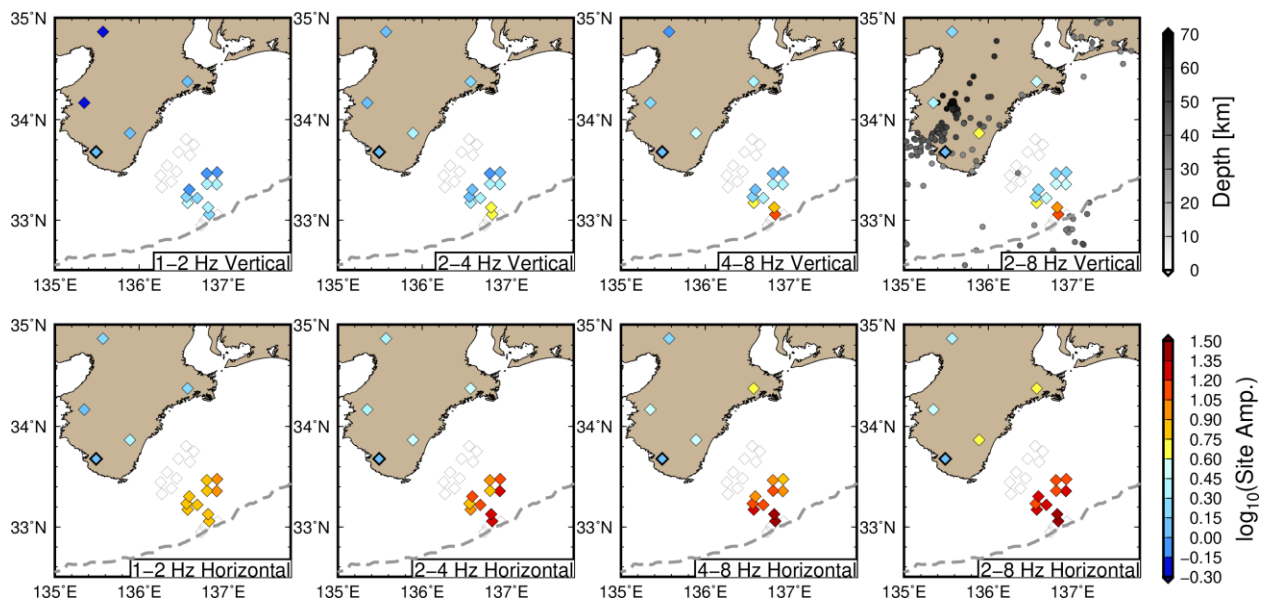
353 Figure 7 shows the normalized seismic energy  $E/C$  at each distance. As previously  
354 mentioned, the seismic energies of shallow tremors were evaluated using velocity envelopes at  
355 2–8 Hz. Although an impulse STF was assumed in the CPS synthetics, a 10-s half-value width  
356 (dashed lines in the right panels in Figure 7) was expected because of the 5-s moving average  
357 smoothing. As  $C$  is common at stations at the same distance, the ratios of the seismic energies of  
358 DONET1D and DONET1D' (amplification factor for seismic energy) (Figure 8) reflect the  
359 amplification factors of the seismic energies at each station. The differences for an intraslab  
360 earthquake (Figures 7a and 8a) were nearly constant (2–3 times), irrespective of the distance.  
361 These results indicate that the seismic energies for an intraslab earthquake can be estimated using  
362 the conventional method. Distance-dependent features of seismic energy amplification were  
363 observed for the shallow tremor source (Figures 7b and 8b). At distances of  $\leq 5$  km (the region  
364 just above a source), we observed an amplification factor of approximately 4. This is slightly  
365 larger than that of an intraslab source (3.3) but can be considered a vertical incident amplification  
366 factor. Large ( $> 5$ ) seismic energy amplifications were observed at distances of 5–20 km.  
367 Reflected *S*-waves from the sediment/oceanic crust boundary (plate boundary) appeared  
368 repeatedly (Movie S1) in DONET1D, although such phases were not observed in DONET1D'  
369 (Movie S2). The smoothed velocity envelopes in DONET1D contained such reflections;  
370 consequently, large energy amplifications occurred at distances of 5–20 km.

371 According to previous studies of shallow slow earthquakes (Masaru Nakano et al., 2018;  
372 Sugioka et al., 2012; Takemura et al., 2019; Takemura, Hamada, et al., 2023), we considered that  
373 shallow tremors could be molded by a low-angle thrust faulting mechanism around the plate  
374 boundary. In this case, *S*-wave energies can be weakened at distances of 5–20 km due to the four-  
375 lobe *S*-wave source radiation pattern (red symbols in Figures 6b and 7b). Four-lobe *S*-wave  
376 amplitude pattern are gradually distorted as increasing frequency and distance because of seismic  
377 wave scattering due to small-scale heterogeneities (e.g., Imperatori & Mai, 2013; Morioka et al.,  
378 2017; S. Takemura et al., 2009, 2016). Takemura, Yabe, et al. (2020) demonstrated that in the  
379 cases of seismic sources just below or within thick sedimentary layer, trapping seismic wave  
380 energies within thick sedimentary layers also cause distortion of four-lobe *S*-wave amplitude  
381 pattern. Thus, significant amplifications of seismic energies for shallow tremor appear at  
382 distances of 5–20 km. At distances  $> 20$  km, *S*-waves propagated horizontally, and the  
383 amplification of seismic energy weakened with increasing distance. Seismic energy  
384 amplifications of a shallow tremor at distances less than 5 km are similar as those for an intraslab  
385 earthquake.

386 Stronger attenuation compared with the empirical law has been estimated at shallower  
 387 depths (e.g., Abercrombie, 1997; Eberhart-Phillips et al., 2014; Yoshida et al., 2023). Thus, we  
 388 additionally synthesized seismograms using DONET1Dq, where  $Q_S$  value within the shallowest  
 389 layer was replaced from 39.8 to 20. Figure S1 shows seismic energy amplifications of  
 390 DONET1Dq. Amplifications of seismic energies become weaker from the original DONET1D,  
 391 but amplifications due to the propagation path within thick sedimentary layers are still significant  
 392 at epicentral distances of 5-20 km. Although our knowledge of  $Q_S$  structures at shallower depths  
 393 is limited, propagation-path amplification tends to be dominant in shallow tremor seismograms  
 394 at distances of 5-20 km.

395 To evaluate the effects of the STFs, we synthesized them based on the BSE model (Ide,  
 396 2008; Ide & Maury, 2018). We prepared 200 BSE model STFs with a characteristic time  $\alpha$  of  
 397  $0.01 \text{ s}^{-1}$ , which were normalized as each seismic moment of 1. These STFs were convolved using  
 398 Green's functions in DONET1D and DONET1D'. The resultant ratios of the seismic energies of  
 399 DONET1D and DONET1D' are illustrated in Figure 9a. Figure 9b shows two examples of BSE  
 400 model STFs. The duration of the prepared BSE model STFs ranged from 1–54 s (Figure 9c).  
 401 Although fluctuations in seismic energy ratios were recognized (Figure 9a), large amplifications  
 402 of seismic energies at distances of 5–20 km were commonly observed. The strength of the  
 403 envelope broadening appears to depend on the source duration (solid, dashed, and dotted lines in  
 404 Figure 9d). Parameters  $\tau$  and  $\tau_0$  are the half-value widths of the synthetic envelopes from  
 405 DONET1D and DONET1D', respectively. The BSE model STFs with shorter durations  
 406 exhibited strong envelope broadening (large  $(\tau-\tau_0)/\tau_0$ ), as shown by the results of an impulse STF  
 407 (bold blue line in Figure 9d). With increasing source duration, the effects of envelope broadening  
 408 caused by the thick sedimentary layer tended to be relatively weak (blue dashed and dotted lines).  
 409 For the longest duration STF case (blue dotted line), nearly similar half-value widths ( $(\tau-\tau_0)/\tau_0 \approx$   
 410 0) were measured in both models. If source durations are sufficiently longer than the envelope  
 411 widths of Green's functions, the strength of envelope broadening caused by thick sedimentary  
 412 layers becomes relatively weak; consequently, overestimations of source durations are negligible.

413



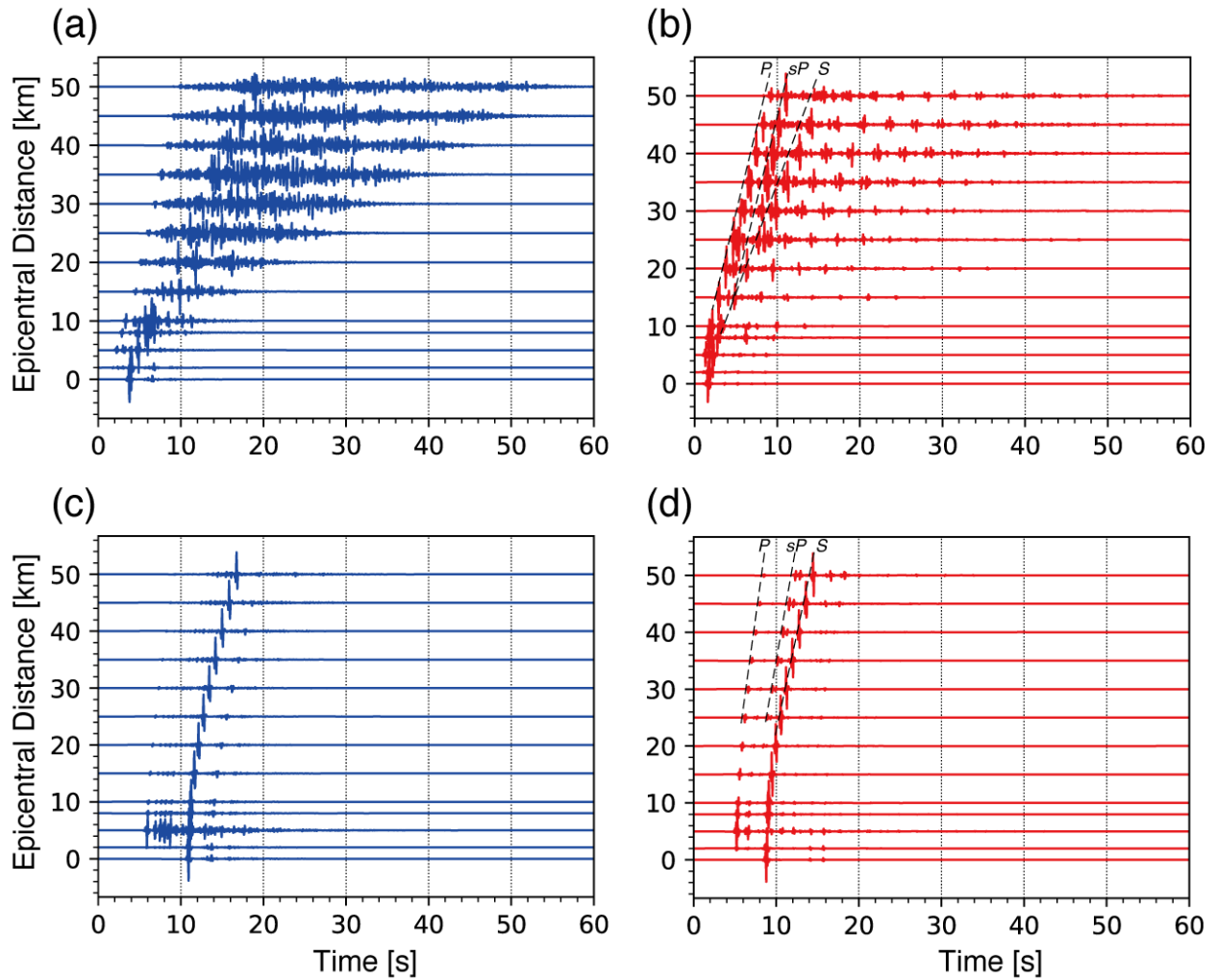
414

415 **Figure 3.** Spatial variations of site amplification factors at each frequency band. The upper and  
416 bottom panels are site amplification factors for vertical and horizontal components, respectively.  
417 The gray circles in the upper right panel are epicenters of slab earthquakes used in estimating site  
418 amplification factors. The diamond enclosed by the bold line is the reference site N.KMTF (the  
419 site amplification factor of N.KMTF was fixed as 1).

420

421

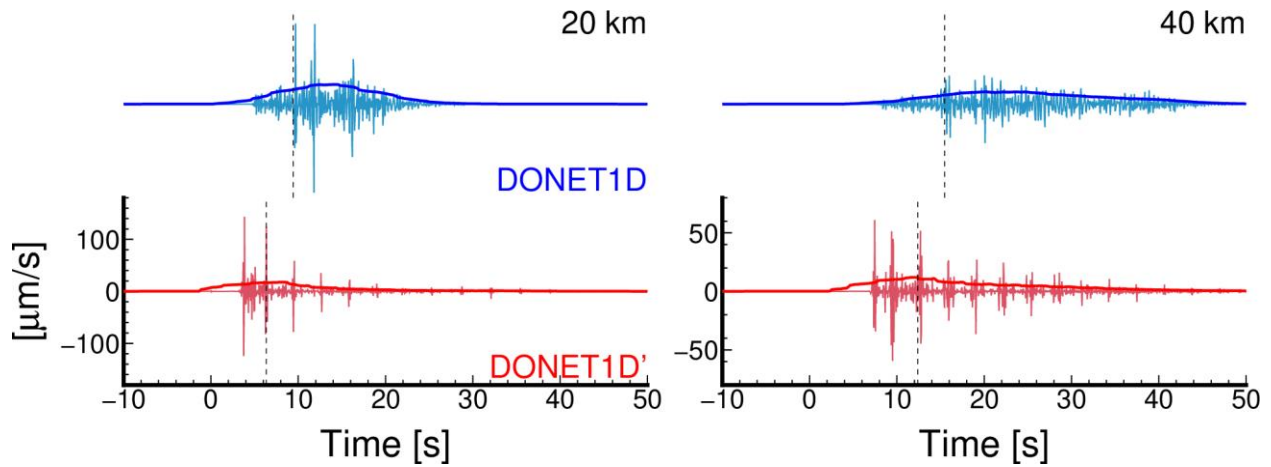
422



423

424 **Figure 4.** Radial component velocity seismograms synthesized using CPS. The seismic sources  
 425 in (a, b) and (c, d) are a shallow tremor and intraslab earthquake, respectively. The source time  
 426 functions of each case are an impulse. (a, c) DONET1D and (b, d) DONET1D'. We applied a  
 427 bandpass filter of 2–8 Hz, and maximum amplitudes at each trace were normalized.

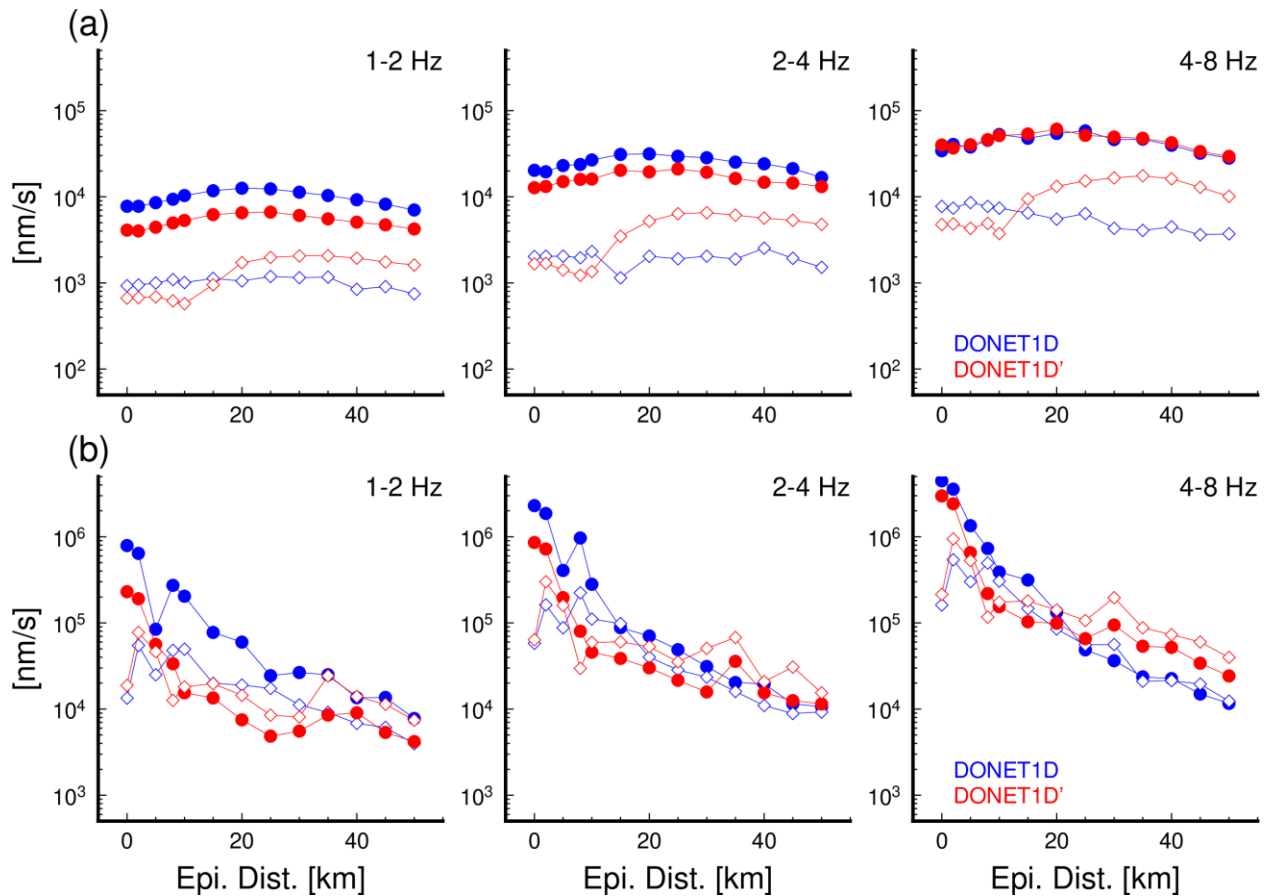
428



429

430 **Figure 5.** Examples of Green's functions at distances of 20 and 40 km for a shallow tremor  
 431 source. The radial component velocity traces were filtered with a passed frequency of 2–8 Hz.  
 432 The bold lines are smoothed velocity envelope traces. The black dashed lines represent  
 433 theoretical *S*-wave travel times in each model.

434

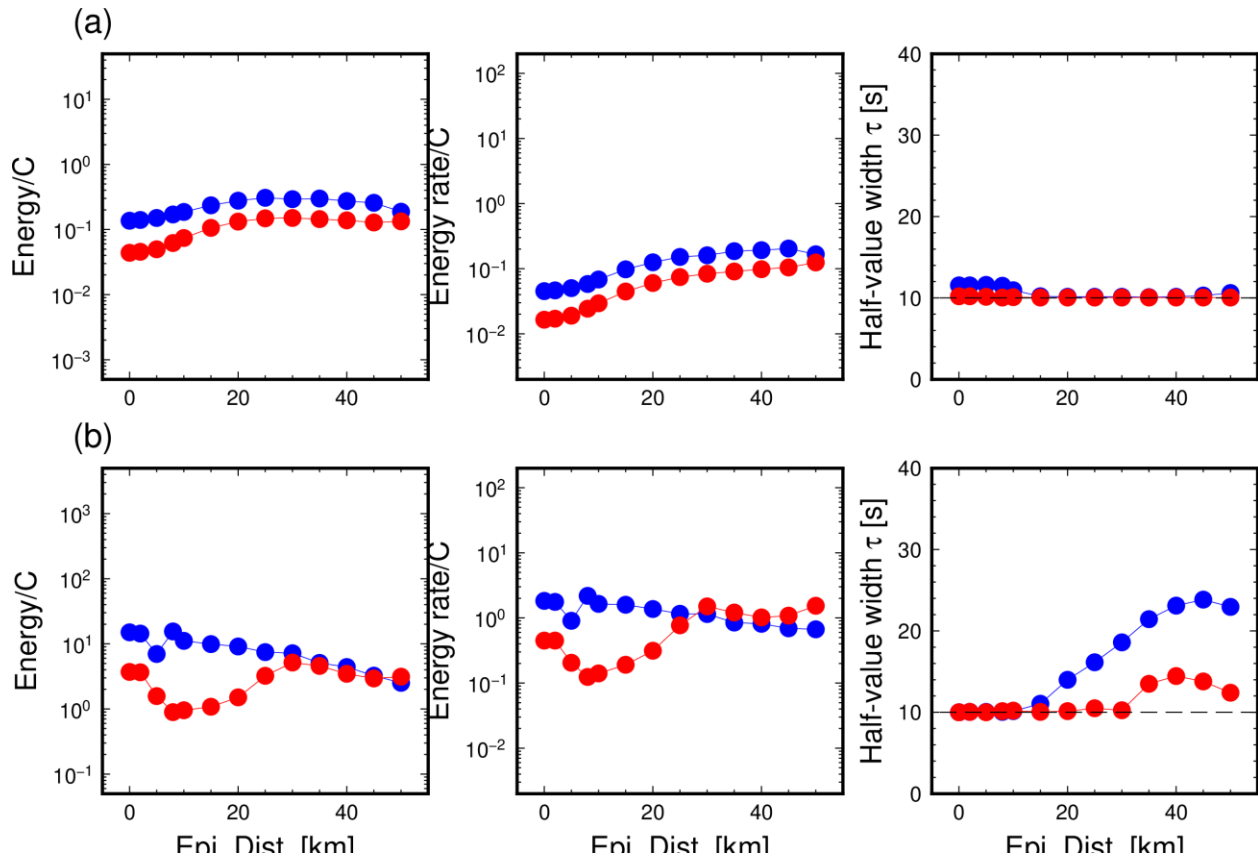


435

436 **Figure 6.** Maximum *S*-wave amplitudes at each frequency band from (a) intraslab earthquake  
 437 and (b) shallow tremor sources. The blue and red symbols are the maximum *S*-wave amplitudes

438 in DONET1D and DONET1D', respectively. The filled and open symbols are those in horizontal  
 439 and vertical components, respectively.

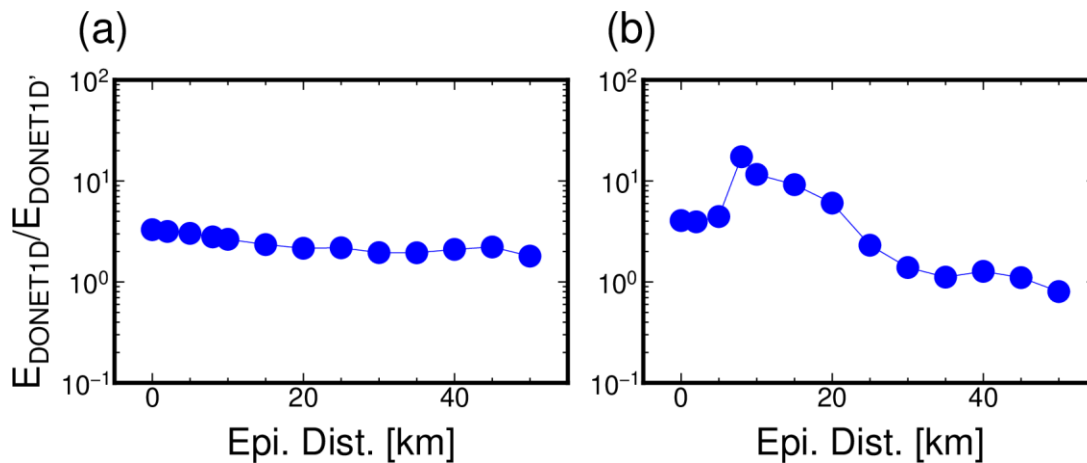
440



441

442 **Figure 7.** Normalized seismic energies of (a) intraslab earthquake and (b) shallow tremors.  
 443 Normalization factor  $C$  includes physical parameters and anelastic attenuation. The blue and red  
 444 symbols represent the results of DONET1D and DONET1D', respectively.

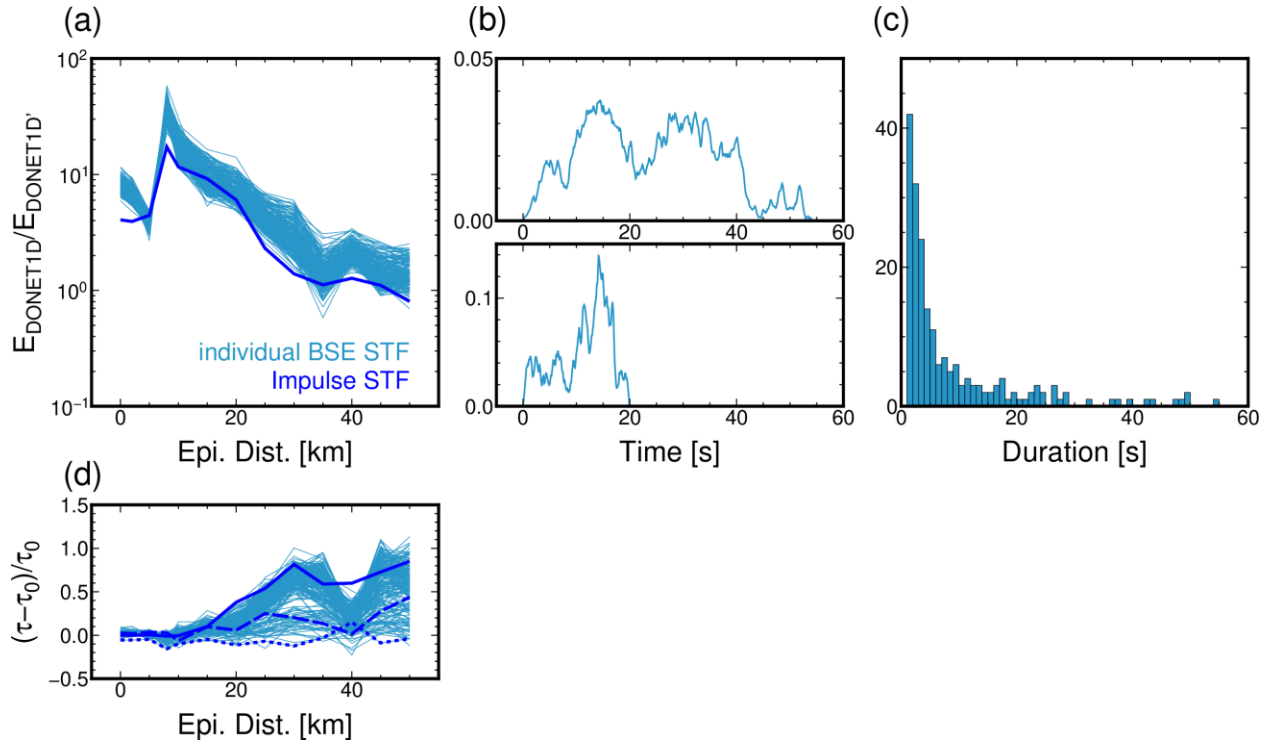
445



446

447 **Figure 8.** Ratio of seismic energies between DONET1D and DONET1D' for (a) intraslab  
 448 earthquake and (b) shallow tremor sources.

449



450

451 **Figure 9.** Ratio of seismic energies of shallow tremor using the Brownian slow earthquake  
 452 (BSE) model with a characteristic time of  $\alpha = 0.01 \text{ s}^{-1}$ . (a) The ratio of seismic energies between  
 453 DONET1D and DONET1D' for the BSE model and impulse STF (Green's function), (b)  
 454 examples of BSE model STF, and (c) durations of used BSE model STFs. The light blue lines in  
 455 (a) represent ratios of seismic energies between DONET1D and DONET1D' for individual BSE  
 456 model STFs. The blue bold line is the same as in Figure 8b. (d) Estimated half-value width ratio  
 457 between DONET1D ( $\tau$ ) and DONET1D' ( $\tau_0$ ). The blue bold, dashed, and dotted lines in (d) are  
 458 ratios of impulse STF, BSE model STF with a duration of 17 s, and the longest BSE model STF  
 459 (54 s), respectively.

460

461

## 462 **4 Discussion**

463 The characteristics of seismic energy amplification caused by thick sedimentary layers  
 464 differ between intraslab earthquakes and shallow tremors. Large amplifications at distances of 5–  
 465 20 km cannot be corrected using site amplification factors based on conventional methods.  
 466 Owing to the signal-to-noise ratio of shallow tremors at OBSs, near-source ( $\leq 20$  km) OBSs are  
 467 selected for analysis. Based on seismic energy amplifications due to thick sedimentary layers  
 468 (Figure 8b), we should correct additional 0.5–1 order amplifications in seismic energies of  
 469 shallow tremors in previous studies along the Nankai Trough. This amplification correction is  
 470 valid when shallow tremors occur at the plate interface.

471

### 472 **4.1. Effects of invalid rigidity assumption on seismic energy estimation**

473 Slow earthquake phenomena are considered slip phenomena at the plate boundary.  
 474 Although the precise determination of the source depths of shallow slow earthquakes remains  
 475 challenging, shallow VLFES tend to be located within underthrust sediments around the  
 476 décollement (Akuhara et al., 2020; Sugioka et al., 2012; Yamamoto et al., 2022). Underthrust  
 477 sediments are considered to have low seismic velocity (1–2 km/s). In this situation, is the  
 478 assumption of 33 GPa rigidity ( $V_S = 3.5$  km/s and  $\rho = 2.7$  g/cm<sup>3</sup>) in the conventional seismic  
 479 energy estimation valid? We investigated the structural dependency of the source region in the  
 480 seismic energy estimation. We synthesized Green's functions at depths of 6.0 and 9.0 km. The  
 481 former and latter sources are located within the underthrust sediment ( $V_S = 2.3$  km/s) and oceanic  
 482 crust layer 2 ( $V_S = 3.3$  km/s). We fixed a focal mechanism and a seismic moment of  $3.98 \times 10^{13}$   
 483 Nm, as in previous synthetics.

484 In all synthetics, relatively large amplifications were observed at distances of 5–20 km.  
 485 Based on these results, we concluded that amplifications caused by path effects of the thick  
 486 sedimentary layers were dominant at distances of 5–20 km because the reflected *S*-waves from  
 487 the plate interface had sufficient amplitudes. In such cases, the energies of the reflected *S*-waves  
 488 are contaminated within a half-value width time window of smooth envelopes; consequently, the  
 489 seismic energies of shallow tremors tend to be overestimated.

490 Although the effects of multiple *S*-wave reflections commonly appear at distances of 5–  
 491 20 km, the level of seismic energy amplification increases with decreasing source depth. This is  
 492 because of the differences in rigidity between DONET1D and DONET1D'. Although the seismic  
 493 moment was fixed as  $3.98 \times 10^{13}$  Nm, and the rigidity of DONET1D' was constant (28 GPa) at  
 494 depths shallower than 11 km, the rigidities of the source regions at depths of 6 and 9 km in  
 495 DONET1D were 12 and 28 GPa, respectively. Although a double-couple source could not be  
 496 strictly assumed at the plate boundary, the rigidity at a depth of 8.07 km (plate interface) was 28  
 497 GPa, just below the underthrust sediments (12 GPa). Thus, the intermediate features between the  
 498 6- and 9-km sources. These rigidity differences could be another cause of seismic energy  
 499 amplification, assuming far-field *S*-wave propagation in an infinite medium with a rigidity of 33  
 500 GPa. The precise spatial distribution of rigidity is also important for seismic moment estimation  
 501 (Figures 4, 5, and 7 in Takemura et al., 2021). Although the seismic moment is proportional to  
 502 the observed amplitudes, the seismic energy is calculated by temporal integration of the square  
 503 velocity amplitudes. Thus, the effects of incorrect rigidity assumptions are more severe in the  
 504 seismic energy estimation.

505

## 506 **4.2. Propagation path amplifications along the Japan Trench**

507 The seismic and scaled energies of slow earthquakes were also evaluated along the Japan  
508 Trench, offshore regions of northeastern Japan, and Hokkaido (Yabe et al., 2021). These were  
509 calculated using the OBS network (S-net), assuming far-field body wave propagation in an  
510 infinite medium. We also synthesized velocity seismograms using a 1D velocity model around  
511 the Japan Trench to validate their estimations. The 1D model was constructed from a 1D depth  
512 profile at 143.6 °E and 40.0 °N from the local 3D model of Koketsu et al. (2012). The region at  
513 143.6 °E and 40.0 °N is approximately the centroid of tremor activity. We refer to this model as  
514 NEJP1D. We also constructed NEJP1D' in which the physical parameters of the sedimentary  
515 layers in NEJP1D were replaced with those of the crust. The source of the tremor was located at  
516 a depth of 12.85 km. The ratios between NEJP1D and NEJP1D' (Figure 11a) were stable (3.5–7)  
517 compared with those along the Nankai Trough (Figure 8b). We also plotted energy  
518 amplifications for an intraslab earthquake (diamonds in the middle panel of Figure 11a). Because  
519 of differences in focal mechanisms and incident angles to the basement, amplifications for an  
520 intraslab earthquake were more stable and larger, but distant-independent features commonly  
521 appeared in both cases. The differences of seismic energy amplifications between tremors and  
522 intraslab earthquakes were weaker compared with those along the Nankai Trough (Figure 8).  
523 Thus, the conventional method, which assumes far-field body wave propagation, practically  
524 works in the Tohoku region. This is because the tremors occurred sufficiently deeper than the  
525 basement of the sedimentary layer (Figure 11b). The differences in the propagation paths  
526 between tremors along the Nankai Trough and Japan Trench are illustrated in Figures 1b and 11b.

527 The signal-to-noise ratio of shallow tremors is typically low at OBSs far from their  
528 sources. Thus, near-source ( $\leq 20$  km) OBS data are often selected in seismic energy estimations  
529 of shallow tremors. In addition, site amplifications from the conventional method (Figure 3) are  
530 mostly controlled by thin lower-velocity ( $< 0.6$  km/s) sediments just below stations. Based on the  
531 above synthetic studies and the selected use of near-source OBSs, we conclude that  
532 approximately 0.5–1.3 order overestimations can occur in the seismic energy estimation of  
533 shallow tremors along the Nankai Trough (Figures 8 and 10). These overestimations were caused  
534 by propagation path effects and an invalid rigidity assumption. Similar overestimations are  
535 expected for shallow slow earthquakes in the regions of Hikurangi, Mexico, and Costa Rica if  
536 near-source OBSs are used. Shallow slow earthquakes are located near the trough or shallower  
537 ( $\leq 10$  km) depths (Baba et al., 2021; Plata-Martinez et al., 2021; Todd et al., 2018; Walter et al.,  
538 2013). Although slow earthquakes are generally phenomena of faulting on the plate boundary,  
539 amplifications are typically more severe if shallow tremors occur within sedimentary layers.

540

## 541 **4.3. Scaled energy of seismic slow earthquakes at deep and shallow depths around Japan**

542 Based on the above results, we revisited the scaled energy of slow earthquakes. Figure 12  
543 shows the relationships between the seismic energy and moment rates for slow earthquakes in  
544 various regions. Deep slow earthquakes in the Nankai, Mexico, and Cascadia subduction zones  
545 were obtained from previous studies (Ide, 2016; Ide & Maury, 2018; Ide & Yabe, 2014). We also  
546 plotted the relationship between the moment and seismic energy rates of slow earthquakes along  
547 the Japan Trench (Yabe et al., 2021). Based on the effects of the thick sedimentary layer around  
548 the shallow slow earthquake sources along the Nankai Trough, we performed a 1 order

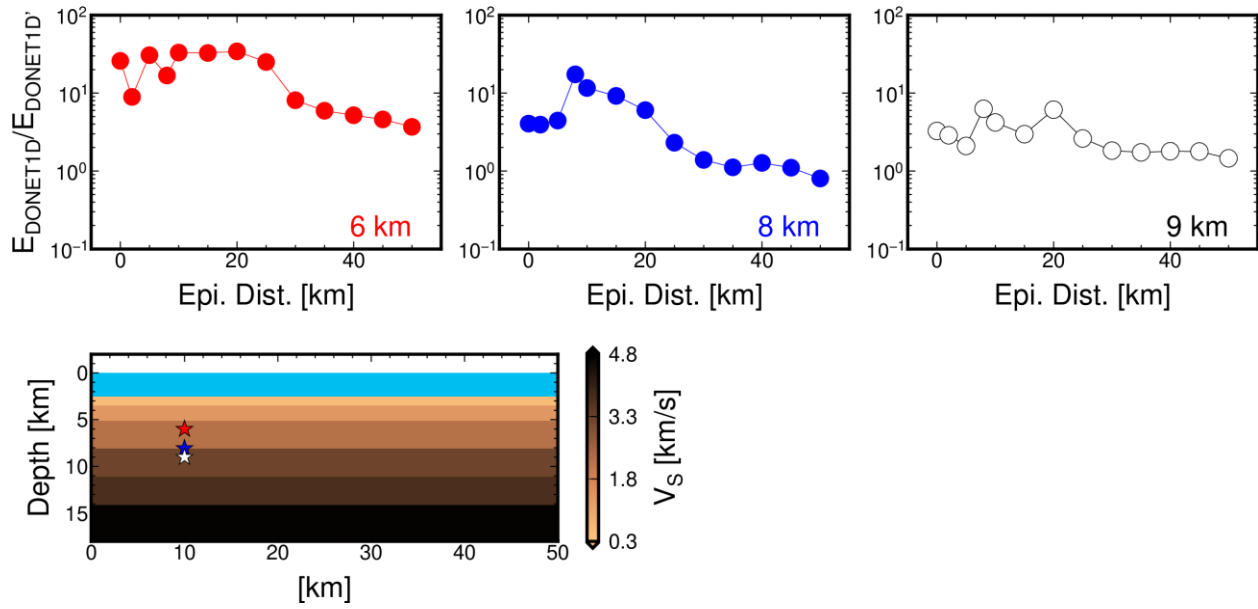
549 correction for the seismic energy rates of shallow tremor and a 0.3 order correction for the  
550 seismic moment rate of shallow VLFs along the Nankai Trough from the results in Yabe et al.  
551 (2019, 2021). The 0.3 order corrections of the seismic moment rates of the shallow VLFs were  
552 determined by the rigidity difference between the oceanic crust (28 GPa) and underthrust  
553 sediments (12 GPa). The rigidity of the oceanic crust is almost twice that of underthrust  
554 sediments, and a two-fold amplification of the VLFE signals is expected. Temperature and  
555 lithostatic pressure at deep depths are 150–500 °C and 0.7–1.7 GPa, which are significantly  
556 larger than those at shallower depths ( $< 150^{\circ}\text{C}$  and  $< 0.2$  GPa) (Behr & Bürgmann, 2021; Saffer  
557 & Wallace, 2015; Syracuse et al., 2010). Even for these large differences in tectonic  
558 environments, we concluded that the scaled energies of seismic slow earthquakes range from  $10^{10}$   
559 to  $10^9$ , irrespective of region and depth (filled symbols in Figure 12).

560 An  $Mo \propto T$  scaling law was suggested in 2007 (Ide et al., 2007) using limited catalogs.  
561 Recently, Ide & Beroza (2023) revisited the scaling law of slow earthquakes using the updated  
562 catalogs of slow earthquakes worldwide. They suggested an  $Mo \propto T$  upper-bound scaling law for  
563 deep slow earthquakes in various subduction zones. However, the relationships of detectable  
564 shallow VLFs between seismic moments and durations along Nankai Trough (Sugioka et al.,  
565 2012; Takemura et al., 2019; Takemura, Obara, et al., 2022) are slightly different with an  $Mo \propto$   
566  $T$  upper-bound scaling law for deep slow earthquakes. Shallow VLFs lie between scaling laws  
567 of ordinary ( $Mo \propto T^3$ ) and deep slow ( $Mo \propto T$ ) earthquakes. The detectability of VLFs along  
568 the Nankai Trough was evaluated in Takemura, Baba, Yabe, Yamashita, et al. (2022). Duration  
569 ranges were not different at different depths, but the seismic moments of shallow VLFs were 1–  
570 2 orders larger than those at deeper depths (Ide et al., 2008). A similar trend has been reported in  
571 Costa Rica (Baba et al., 2021). Other differences between shallow and deep slow earthquakes  
572 (durations and recurrent intervals of slow earthquake episodes, migration speeds, etc.) were  
573 summarized in a recent review paper (Takemura, Hamada, et al., 2023). Despite the different  
574 scaling laws between deep and shallow slow earthquakes, our study suggests that the scaled  
575 energies of seismic slow earthquakes are common ( $10^{10}$ – $10^9$ ), irrespective of depth and region.  
576 What factors cause the different distributions of seismic moments and durations at shallow and  
577 deep depths? Source analysis of seismic slow earthquakes under valid assumptions should be  
578 addressed in future studies to answer this question. The integration of seismological, geodetic,  
579 geological, and experimental studies is indispensable for investigating the source physics and  
580 tectonic environments of slow earthquakes.

581

582

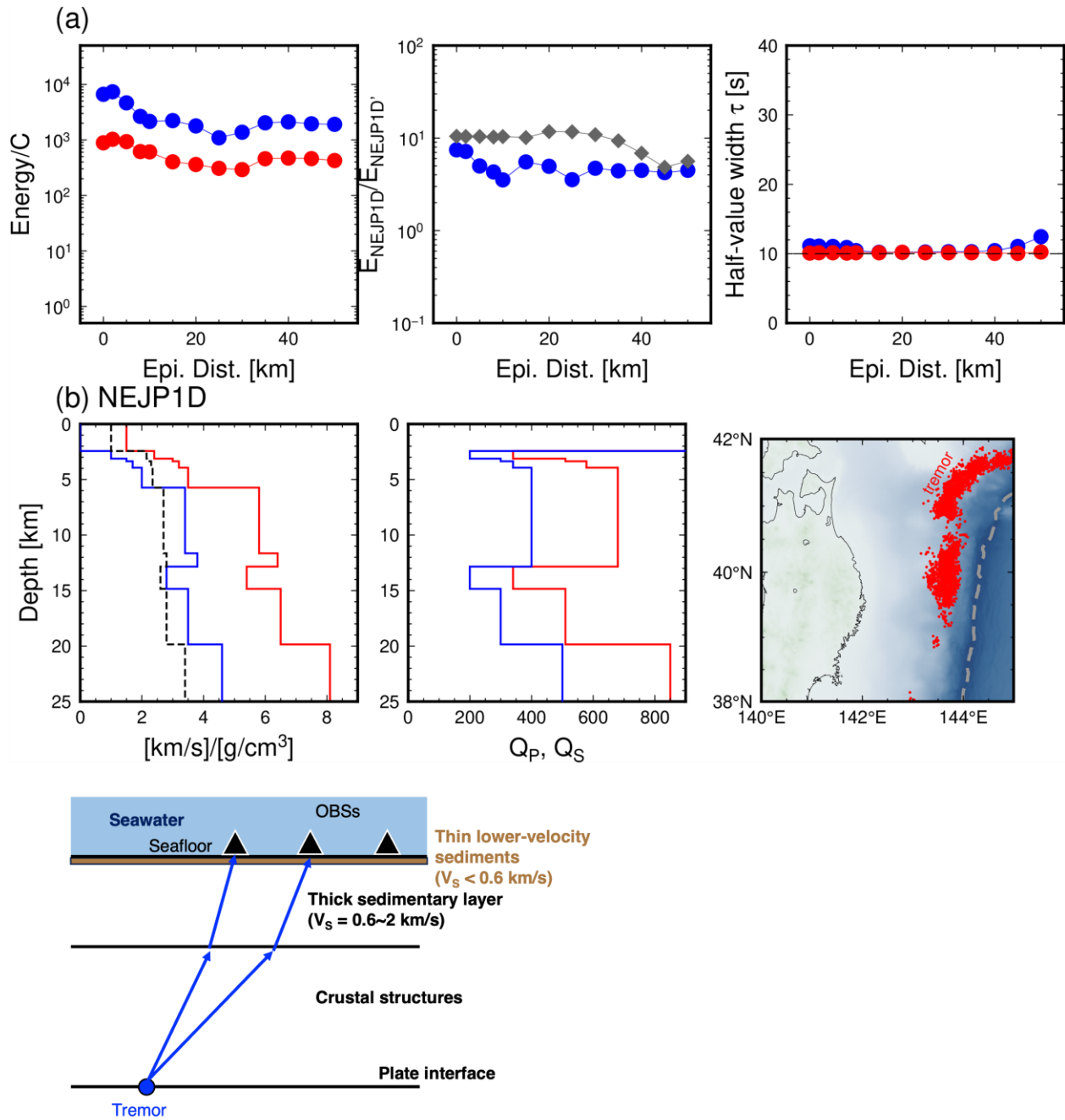
583



584

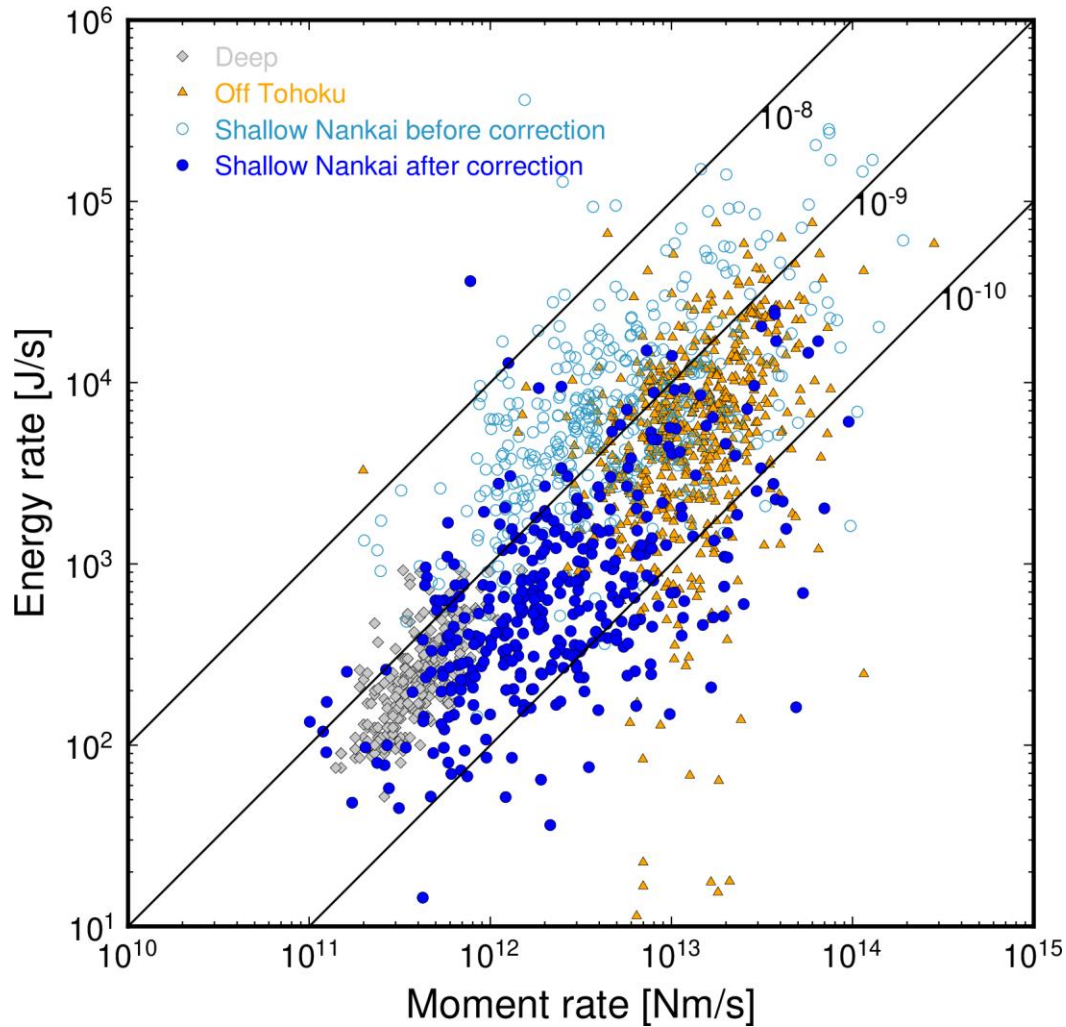
585 **Figure 10.** Seismic energies of shallow tremors at depths of 6 (within the sedimentary layer),  
 586 8.07 (plate boundary), and 9 km (within the 2<sup>nd</sup> layer of the oceanic crust).

587



588

589 **Figure 11.** Seismic energies of synthetic tremor envelopes along the Japan Trench. (a) Seismic  
 590 energies ( $E/C$ ), ratio of seismic energies, and half-value width (duration) of NEJP1D and  
 591 NEJP1D'. In the middle panel of (a), ratio of seismic energies of an intraslab earthquake (40 km  
 592 depth) between NEJP1D and NEJP1D' are also plotted by diamonds. (b) NEJP1D model. The  
 593 red and blue colors represent  $P$ - and  $S$ -waves, respectively. The dashed lines represent density as  
 594 a function of depth. The right panel in (b) is the map around the Japan Trench. Tremor epicenters  
 595 are referred from Nishikawa et al. (2019). The bottom panel in (b) is a schematic figure of  
 596 seismic wave propagation from the tremor off Tohoku.  
 597



598

599 **Figure 12.** Revisited relationships between the seismic energy rates of tremors and seismic  
 600 moments of accompanying VLFs. The gray diamonds indicate deep seismic slow earthquakes  
 601 in Mexico, Cascadia, and Nankai subduction zones (Ide, 2016; Ide & Maury, 2018; Ide & Yabe,  
 602 2014). The orange triangles indicate the seismic moment and energy rates of seismic slow  
 603 earthquakes off Tohoku from Yabe et al. (2021). The light blue open circles indicate the original  
 604 results of shallow slow earthquakes along the Nankai Trough (Yabe et al., 2019, 2021). The  
 605 blue-filled circles indicate corrected relationships between seismic moment and energy rates for  
 606 shallow slow earthquakes along the Nankai Trough.

607

608

## 609 5 Conclusions

610 Recent studies on high-frequency seismic wave propagation have revealed that the  
611 effective trapping of seismic waves within thick sedimentary layers affects the waveforms  
612 observed at OBSs, even for near-source distances. Large envelope broadening and amplification  
613 are expected in high-frequency seismograms of OBSs. Thus, in this study, we investigated the  
614 effects of the propagation path and site amplification on seismic energy estimations for shallow  
615 tremors along the Nankai Trough.

616 Assuming near-vertical incidents to OBSs and far-field *S*-wave propagation, we  
617 estimated frequency-dependent site amplifications at DONET stations; the amplification factors  
618 of DONET stations in the horizontal component ranged from 5 to 40. The synthetics for an  
619 intraslab earthquake assuming a local 1D velocity model with  $V_S \geq 0.6$  km/s are only 1–2 times  
620 the amplifications from a 1D model without sedimentary layers. This indicates that large  
621 amplifications at the DONET stations were primarily controlled by thin lower-velocity ( $< 0.6$   
622 km/s) sediments just below the DONET stations. For a shallow tremor source, 5–10 times the  
623 amplifications of seismic energy due to thick sedimentary layers appeared at near-source ( $\leq 20$   
624 km) distances irrespective of STF complexities. This amplification was caused by multiple  
625 reflected *S*-waves from the plate interface. Because the *S*-phase cannot be identified from typical  
626 tremor waveforms, smoothed velocity envelopes have been widely used in seismic energy  
627 analysis. In this case, multiple reflected *S*-waves were contaminated. If shallow tremors occur  
628 within underthrust sediments, the assumption of far-field *S*-wave propagation in an infinite  
629 medium with a rigidity of 33 GPa is invalid. The incorporation of precise rigidity around the  
630 source region is required.

631 Overestimations owing to thick sedimentary layers often occurred in the seismic energy  
632 estimations of shallow tremors near the trench. Similar overestimations using near-source ( $\leq 20$   
633 km) OBSs potentially occur in regions of Hikurangi, Costa Rica, and Mexico. Based on  
634 propagation path amplification at near-source OBSs and the invalid rigidity assumption,  
635 approximately 0.5–1.3 order overestimations can occur in the seismic energy estimation of  
636 shallow tremors along the Nankai Trough based on the conventional method. After correcting for  
637 overestimations of shallow tremor energy and VLFE moment rates in previous studies, the scaled  
638 energies of shallow seismic slow earthquakes along the Nankai Trough and Japan Trench and  
639 deep seismic slow earthquakes in various regions range from  $10^{-10}$  to  $10^{-9}$ . This means that the  
640 physical mechanisms governing seismic slow earthquakes can be the same, irrespective of region  
641 and source depth.

642

## 643 Acknowledgments

644 This study was supported by a JSPS KAKENHI Grant-in-Aid for Scientific Research (C), grant  
645 number JP21K03696, and a Grant-in-Aid for Scientific Research on Transformative Research  
646 Areas “Science of Slow-to-Fast earthquakes,” grant numbers JP21H05203 and JP21H05205. We  
647 conducted numerical simulations of seismic wave propagation in 3D models using the Earth  
648 Simulator on the *Japan Agency for Marine-Earth Science and Technology* and *Wisteria/BDEC-*  
649 *01 on the Information Technology Center, the University of Tokyo*. The calculation resources of  
650 *Wisteria/BDEC-01* were supported by *Earthquake Research Institute, the University of Tokyo*,

651 Joint Research Program 2023-S-A101. The authors also acknowledge two anonymous reviewers,  
 652 the associate editor and the editor Prof. R. Abercrombie, which helped to improve our  
 653 manuscript.

654

## 655 Open Research

656 We used DONET (National Research Institute for Earth Science and Disaster Resilience, 2019a)  
 657 and F-net (National Research Institute for Earth Science and Disaster Resilience, 2019b) data.  
 658 The Python package, HinetPy (Tian, 2020), was used to download the data. CPS (Herrmann,  
 659 2013) and OpenSWPC (Maeda et al., 2017) were used for waveform synthesis. Seismic analysis  
 660 codes (Goldstein & Snoke, 2005), obspy (Beyreuther et al., 2010), scipy (Virtanen et al., 2020),  
 661 numpy (Harris et al., 2020), and Generic Mapping Tools (Wessel et al., 2013) were used for  
 662 waveform analysis and image creation. The catalog of ordinary earthquakes used to estimate site  
 663 amplification was obtained from the JMA  
 664 (<https://www.data.jma.go.jp/egev/data/bulletin/index.html>). The catalogs of slow earthquakes  
 665 along the Nankai Trough were referred from the “Slow earthquake database” (Kano et al., 2018).  
 666 Estimated site amplification factors at DONET stations and Movies S1-S4 are available at a  
 667 Zenodo repository (Takemura, 2023).

668

669

## 670 References

- 671 Abercrombie, R. E. (1997). Near-surface attenuation and site effects from comparison of surface and deep borehole  
 672 recordings. *Bulletin of the Seismological Society of America*, 87(3), 731–744.  
 673 <https://doi.org/10.1785/BSSA0870030731>
- 674 Akuhara, T., Tsuji, T., & Tonegawa, T. (2020). Overpressured Underthrust Sediment in the Nankai Trough Forearc  
 675 Inferred From Transdimensional Inversion of High-Frequency Teleseismic Waveforms. *Geophysical Research*  
 676 *Letters*, 47(15), 0–3. <https://doi.org/10.1029/2020GL088280>
- 677 Annoura, S., Obara, K., & Maeda, T. (2016). Total energy of deep low-frequency tremor in the Nankai subduction  
 678 zone, southwest Japan. *Geophysical Research Letters*, 43(6), 2562–2567.  
 679 <https://doi.org/10.1002/2016GL067780>
- 680 Aoi, S., Asano, Y., Kunugi, T., Kimura, T., Uehira, K., Takahashi, N., et al. (2020). MOWLAS: NIED observation  
 681 network for earthquake, tsunami and volcano. *Earth, Planets and Space*, 72(1).  
 682 <https://doi.org/10.1186/s40623-020-01250-x>
- 683 Baba, S., Takeo, A., Obara, K., Matsuzawa, T., & Maeda, T. (2020). Comprehensive Detection of Very Low  
 684 Frequency Earthquakes Off the Hokkaido and Tohoku Pacific Coasts, Northeastern Japan. *Journal of*  
 685 *Geophysical Research: Solid Earth*, 125(1), 2019JB017988. <https://doi.org/10.1029/2019JB017988>
- 686 Baba, S., Obara, K., Takemura, S., Takeo, A., & Abers, G. A. (2021). Shallow Slow Earthquake Episodes Near the  
 687 Trench Axis off Costa Rica. *Journal of Geophysical Research: Solid Earth*, 126(9).  
 688 <https://doi.org/10.1029/2021JB021706>
- 689 Bartlow, N. M., Miyazaki, S., Bradley, A. M., & Segall, P. (2011). Space-time correlation of slip and tremor during  
 690 the 2009 Cascadia slow slip event. *Geophysical Research Letters*, 38(18), 1–6.  
 691 <https://doi.org/10.1029/2011GL048714>
- 692 Behr, W. M., & Bürgmann, R. (2021). What’s down there? The structures, materials and environment of deep-  
 693 seated slow slip and tremor. *Philosophical Transactions of the Royal Society A: Mathematical, Physical and*  
 694 *Engineering Sciences*, 379(2193), 20200218. <https://doi.org/10.1098/rsta.2020.0218>
- 695 Beroza, G. C., & Ide, S. (2011). Slow Earthquakes and Nonvolcanic Tremor. *Annual Review of Earth and Planetary*  
 696 *Sciences*, 39(1), 271–296. <https://doi.org/10.1146/annurev-earth-040809-152531>

- 697 Beyreuther, M., Barsch, R., Krischer, L., Megies, T., Behr, Y., & Wassermann, J. (2010). ObsPy: A Python Toolbox  
698 for Seismology. *Seismological Research Letters*, 81(3), 530–533. <https://doi.org/10.1785/gssrl.81.3.530>
- 699 Brocher, T. M. (2005). Empirical relations between elastic wavespeeds and density in the Earth's crust. *Bulletin of*  
700 *the Seismological Society of America*, 95(6), 2081–2092. <https://doi.org/10.1785/0120050077>
- 701 Brocher, T. M. (2008). Key elements of regional seismic velocity models for long period ground motion  
702 simulations. *Journal of Seismology*, 12(2), 217–221. <https://doi.org/10.1007/s10950-007-9061-3>
- 703 Brown, J. R., Beroza, G. C., Ide, S., Ohta, K., Shelly, D. R., Schwartz, S. Y., et al. (2009). Deep low-frequency  
704 earthquakes in tremor localize to the plate interface in multiple subduction zones. *Geophysical Research*  
705 *Letters*, 36(19), L19306. <https://doi.org/10.1029/2009GL040027>
- 706 Dixon, T. H., Jiang, Y., Malservisi, R., McCaffrey, R., Voss, N., Protti, M., & Gonzalez, V. (2014). Earthquake and  
707 tsunami forecasts: Relation of slow slip events to subsequent earthquake rupture. *Proceedings of the National*  
708 *Academy of Sciences*, 111(48), 17039–17044. <https://doi.org/10.1073/pnas.1412299111>
- 709 Eberhart-Phillips, D., Thurber, C., & Fletcher, J. B. (2014). Imaging P and S Attenuation in the Sacramento-San  
710 Joaquin Delta Region, Northern California. *Bulletin of the Seismological Society of America*, 104(5), 2322–  
711 2336. <https://doi.org/10.1785/0120130336>
- 712 Fichtner, A., Igel, H., Bunge, H. P., & Kennett, B. L. N. (2009). Simulation and inversion of seismic wave  
713 propagation on continental scales based on a spectral-element method. *Journal of Numerical Analysis,*  
714 *Industrial and Applied Mathematics*, 4(1–2), 11–22.
- 715 Goldstein, P., & Snoke, A. (2005). SAC Availability for the IRIS Community. Retrieved from  
716 <https://ds.iris.edu/ds/newsletter/vol7/no1/193/sac-availability-for-the-iris-community/>
- 717 Harris, C. R., Millman, K. J., van der Walt, S. J., Gommers, R., Virtanen, P., Cournapeau, D., et al. (2020). Array  
718 programming with NumPy. *Nature*, 585(7825), 357–362. <https://doi.org/10.1038/s41586-020-2649-2>
- 719 Herrmann, R. B. (2013). Computer Programs in Seismology: An Evolving Tool for Instruction and Research.  
720 *Seismological Research Letters*, 84(6), 1081–1088. <https://doi.org/10.1785/0220110096>
- 721 Ide, S. (2008). A Brownian walk model for slow earthquakes. *Geophysical Research Letters*, 35(17), L17301.  
722 <https://doi.org/10.1029/2008GL034821>
- 723 Ide, S. (2016). Characteristics of slow earthquakes in the very low frequency band: Application to the Cascadia  
724 subduction zone. *Journal of Geophysical Research: Solid Earth*, 121(8), 5942–5952.  
725 <https://doi.org/10.1002/2016JB013085>
- 726 Ide, S. (2021). Empirical Low-Frequency Earthquakes Synthesized From Tectonic Tremor Records. *Journal of*  
727 *Geophysical Research: Solid Earth*, 126(12). <https://doi.org/10.1029/2021JB022498>
- 728 Ide, S., & Beroza, G. C. (2001). Does apparent stress vary with earthquake size? *Geophysical Research Letters*,  
729 28(17), 3349–3352. <https://doi.org/10.1029/2001GL013106>
- 730 Ide, S., & Beroza, G. C. (2023). Slow earthquake scaling reconsidered as a boundary between distinct modes of  
731 rupture propagation. *Proceedings of the National Academy of Sciences*, 120(32).  
732 <https://doi.org/10.1073/pnas.2222102120>
- 733 Ide, S., & Maury, J. (2018). Seismic Moment, Seismic Energy, and Source Duration of Slow Earthquakes:  
734 Application of Brownian slow earthquake model to three major subduction zones. *Geophysical Research*  
735 *Letters*, 45(7), 3059–3067. <https://doi.org/10.1002/2018GL077461>
- 736 Ide, S., & Yabe, S. (2014). Universality of slow earthquakes in the very low frequency band. *Geophysical Research*  
737 *Letters*, 41(8), 2786–2793. <https://doi.org/10.1002/2014GL059712>
- 738 Ide, S., Beroza, G. C., Shelly, D. R., & Uchide, T. (2007). A scaling law for slow earthquakes. *Nature*, 447(7140),  
739 76–79. <https://doi.org/10.1038/nature05780>
- 740 Ide, S., Imanishi, K., Yoshida, Y., Beroza, G. C., & Shelly, D. R. (2008). Bridging the gap between seismically and  
741 geodetically detected slow earthquakes. *Geophysical Research Letters*, 35(10), 2–7.  
742 <https://doi.org/10.1029/2008GL034014>
- 743 Imperatori, W., & Mai, P. M. (2013). Broad-band near-field ground motion simulations in 3-dimensional scattering  
744 media. *Geophysical Journal International*, 192(2), 725–744. <https://doi.org/10.1093/gji/ggs041>
- 745 Ito, Y., Obara, K., Matsuzawa, T., & Maeda, T. (2009). Very low frequency earthquakes related to small asperities  
746 on the plate boundary interface at the locked to aseismic transition. *Journal of Geophysical Research: Solid*  
747 *Earth*, 114(B11), 1–16. <https://doi.org/10.1029/2008JB006036>
- 748 Itoh, Y., Aoki, Y., & Fukuda, J. (2022). Imaging evolution of Cascadia slow-slip event using high-rate GPS.  
749 *Scientific Reports*, 12(1), 7179. <https://doi.org/10.1038/s41598-022-10957-8>
- 750 Kamei, R., Pratt, R. G., & Tsuji, T. (2012). Waveform tomography imaging of a megasplay fault system in the  
751 seismogenic Nankai subduction zone. *Earth and Planetary Science Letters*, 317–318, 343–353.  
752 <https://doi.org/10.1016/j.epsl.2011.10.042>

- 753 Kanamori, H., & Rivera, L. (2006). Energy partitioning during an earthquake. *Geophysical Monograph Series*, 170,  
754 3–13. <https://doi.org/10.1029/170GM03>
- 755 Kano, M., Aso, N., Matsuzawa, T., Ide, S., Annoura, S., Arai, R., et al. (2018). Development of a slow earthquake  
756 database. *Seismological Research Letters*, 89(4), 1566–1575. <https://doi.org/10.1785/0220180021>
- 757 Kato, A., Obara, K., Igarashi, T., Tsuruoka, H., Nakagawa, S., & Hirata, N. (2012). Propagation of slow slip leading  
758 up to the 2011 Mw9.0 Tohoku-Oki earthquake. *Science*, 335(6069), 705–708.  
759 <https://doi.org/10.1126/science.1215141>
- 760 Kato, A., Fukuda, J., Kumazawa, T., & Nakagawa, S. (2016). Accelerated nucleation of the 2014 Iquique, Chile Mw  
761 8.2 Earthquake. *Scientific Reports*, 6(1), 24792. <https://doi.org/10.1038/srep24792>
- 762 Koketsu, K., Miyake, H., & Suzuki, H. (2012). Japan Integrated Velocity Structure Model Version 1. *Proceedings of*  
763 *the 15th World Conference on Earthquake Engineering*, 1–4. Retrieved from  
764 [http://www.iitk.ac.in/nicee/wcee/article/WCEE2012\\_1773.pdf](http://www.iitk.ac.in/nicee/wcee/article/WCEE2012_1773.pdf)
- 765 Komatitsch, D., Ritsema, J., & Tromp, J. (2002). Geophysics: The spectral-element method, beowulf computing,  
766 and global seismology. *Science*, 298(5599), 1737–1742. <https://doi.org/10.1126/science.1076024>
- 767 Kubo, H., Nakamura, T., Suzuki, W., Kimura, T., Kunugi, T., Takahashi, N., & Aoi, S. (2018). Site Amplification  
768 Characteristics at Nankai Seafloor Observation Network, DONET1, Japan, Evaluated Using Spectral  
769 Inversion. *Bulletin of the Seismological Society of America*, XX(Xx), 1–9. <https://doi.org/10.1785/0120170254>
- 770 Kubo, H., Nakamura, T., Suzuki, W., Kunugi, T., Takahashi, N., & Aoi, S. (2020). Site characteristics of DONET1  
771 seafloor observation network, Japan, evaluated by HVRS of coda and ambient noise. In *Proceedings of the*  
772 *17th World Conference on Earthquake Engineering*. Sendai, Japan.
- 773 Maeda, T., Takemura, S., & Furumura, T. (2017). OpenSWPC: An open-source integrated parallel simulation code  
774 for modeling seismic wave propagation in 3D heterogeneous viscoelastic media 4. *Seismology, Earth, Planets*  
775 *and Space*, 69(1). <https://doi.org/10.1186/s40623-017-0687-2>
- 776 Maury, J., Ide, S., Cruz-Atienza, V. M., Kostoglodov, V., González-Molina, G., & Pérez-Campos, X. (2016).  
777 Comparative study of tectonic tremor locations: Characterization of slow earthquakes in Guerrero, Mexico.  
778 *Journal of Geophysical Research: Solid Earth*, 121(7), 5136–5151. <https://doi.org/10.1002/2016JB013027>
- 779 Maury, J., Ide, S., Cruz-Atienza, V. M., & Kostoglodov, V. (2018). Spatiotemporal Variations in Slow Earthquakes  
780 Along the Mexican Subduction Zone. *Journal of Geophysical Research: Solid Earth*, 123(2), 1559–1575.  
781 <https://doi.org/10.1002/2017JB014690>
- 782 Morioka, H., Kumagai, H., & Maeda, T. (2017). Theoretical basis of the amplitude source location method for  
783 volcano-seismic signals. *Journal of Geophysical Research: Solid Earth*, 122(8), 6538–6551.  
784 <https://doi.org/10.1002/2017JB013997>
- 785 Nakano, Masara, Nakamura, T., Kamiya, S., Ohori, M., & Kaneda, Y. (2013). Intensive seismic activity around the  
786 Nankai trough revealed by DONET ocean-floor seismic observations. *Earth, Planets and Space*, 65(1), 5–15.  
787 <https://doi.org/10.5047/eps.2012.05.013>
- 788 Nakano, Masaru, Hori, T., Araki, E., Kodaira, S., & Ide, S. (2018). Shallow very-low-frequency earthquakes  
789 accompany slow slip events in the Nankai subduction zone. *Nature Communications*, 9(1), 984.  
790 <https://doi.org/10.1038/s41467-018-03431-5>
- 791 Nakano, Masaru, Yabe, S., Sugioka, H., Shinohara, M., & Ide, S. (2019). Event Size Distribution of Shallow  
792 Tectonic Tremor in the Nankai Trough. *Geophysical Research Letters*, 46(11), 5828–5836.  
793 <https://doi.org/10.1029/2019GL083029>
- 794 National Research Institute for Earth Science and Disaster Resilience. (2019a). NIED DONET.  
795 <https://doi.org/10.17598/NIED.0008>
- 796 National Research Institute for Earth Science and Disaster Resilience. (2019b). NIED F-net.  
797 <https://doi.org/10.17598/NIED.0005>
- 798 National Research Institute for Earth Science and Disaster Resilience. (2019c). NIED Hi-net.  
799 <https://doi.org/10.17598/NIED.0003>
- 800 National Research Institute for Earth Science and Disaster Resilience. (2019d). NIED S-net.  
801 <https://doi.org/10.17598/NIED.0007>
- 802 Nishikawa, T., Matsuzawa, T., Ohta, K., Uchida, N., Nishimura, T., & Ide, S. (2019). The slow earthquake spectrum  
803 in the Japan Trench illuminated by the S-net seafloor observatories. *Science*, 365(August), 808–813.  
804 <https://doi.org/10.1126/science.aax5618>
- 805 Nishikawa, Tomoaki, Ide, S., & Nishimura, T. (2023). A review on slow earthquakes in the Japan Trench. *Progress*  
806 *in Earth and Planetary Science*, 10(1), 1. <https://doi.org/10.1186/s40645-022-00528-w>
- 807 Obara, K. (2020). Characteristic activities of slow earthquakes in Japan. *Proceedings of the Japan Academy Series*  
808 *B: Physical and Biological Sciences*, 96(7), 297–315. <https://doi.org/10.2183/PJAB.96.022>

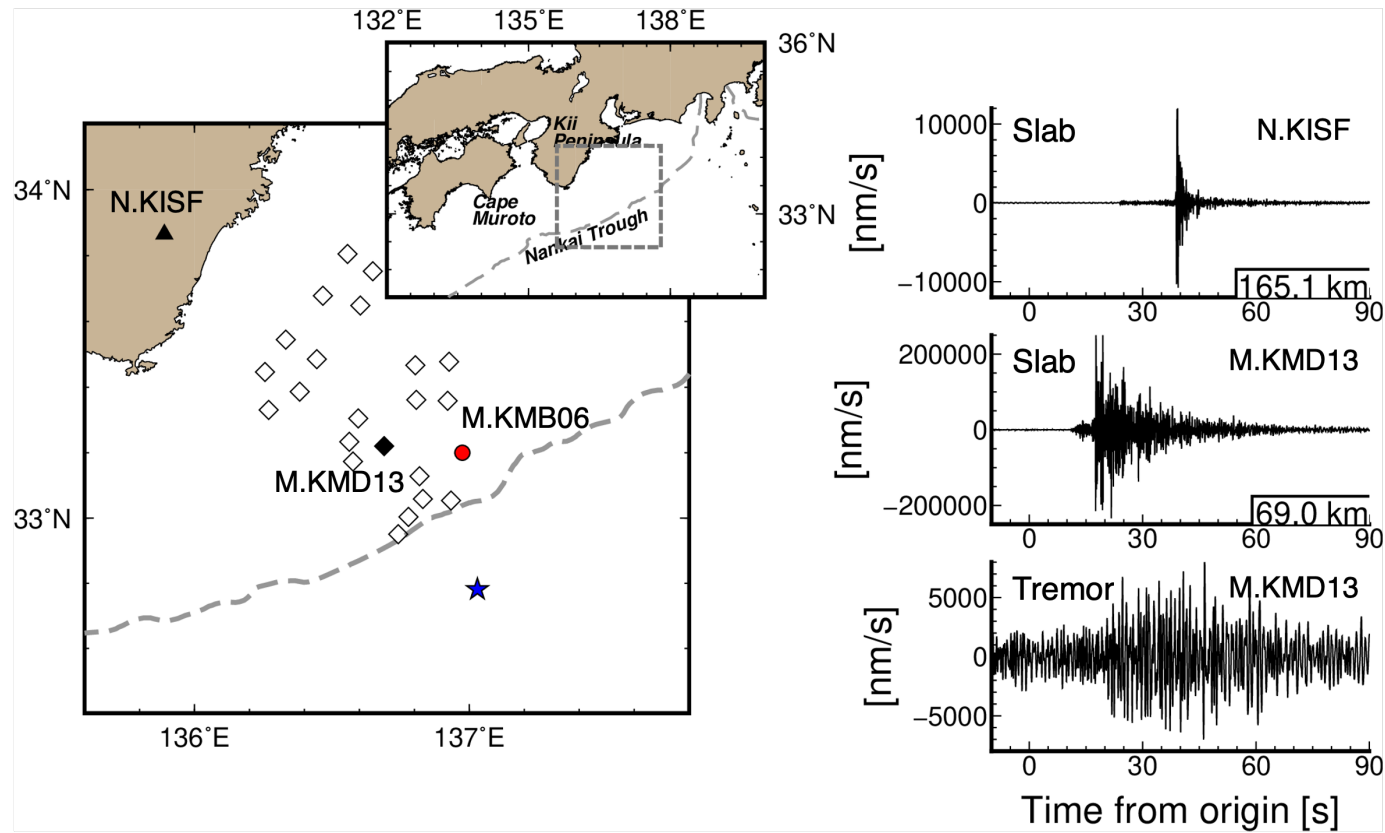
- 809 Obara, K., & Kato, A. (2016). Connecting slow earthquakes to huge earthquakes. *Science*, 353(6296), 253–257.  
810 <https://doi.org/10.1126/science.aaf1512>
- 811 Obara, K., Hirose, H., Yamamizu, F., & Kasahara, K. (2004). Episodic slow slip events accompanied by non-  
812 volcanic tremors in southwest Japan subduction zone. *Geophysical Research Letters*, 31(23).  
813 <https://doi.org/10.1029/2004GL020848>
- 814 Plata-Martinez, R., Ide, S., Shinohara, M., Garcia, E. S., Mizuno, N., Dominguez, L. A., et al. (2021). Shallow slow  
815 earthquakes to decipher future catastrophic earthquakes in the Guerrero seismic gap. *Nature Communications*,  
816 12(1), 3976. <https://doi.org/10.1038/s41467-021-24210-9>
- 817 Rogers, G., & Dragert, H. (2003). Episodic tremor and slip on the Cascadia subduction zone: the chatter of silent  
818 slip. *Science*, 300(5627), 1942–1943. <https://doi.org/10.1126/science.1084783>
- 819 Saffer, D. M., & Wallace, L. M. (2015). The frictional, hydrologic, metamorphic and thermal habitat of shallow  
820 slow earthquakes. *Nature Geoscience*, 8(8), 594–600. <https://doi.org/10.1038/ngeo2490>
- 821 Sato, H., Fehler, M. C., & Maeda, T. (2012). *Seismic Wave Propagation and Scattering in the Heterogeneous*  
822 *Earth : Second Edition*. Berlin, Heidelberg: Springer Berlin Heidelberg. [https://doi.org/10.1007/978-3-642-](https://doi.org/10.1007/978-3-642-23029-5_2)  
823 [23029-5\\_2](https://doi.org/10.1007/978-3-642-23029-5_2)
- 824 Schwartz, S. Y., & Rokosky, J. M. (2007). Slow slip events and seismic tremor at circum-Pacific subduction zones.  
825 *Reviews of Geophysics*, 45(3). <https://doi.org/10.1029/2006RG000208>
- 826 Shelly, D. R., Beroza, G. C., & Ide, S. (2007). Non-volcanic tremor and low-frequency earthquake swarms. *Nature*,  
827 446(7133), 305–307. <https://doi.org/10.1038/nature05666>
- 828 Sugioka, H., Okamoto, T., Nakamura, T., Ishihara, Y., Ito, A., Obana, K., et al. (2012). Tsunamigenic potential of  
829 the shallow subduction plate boundary inferred from slow seismic slip. *Nature Geoscience*, 5(6), 414–418.  
830 <https://doi.org/10.1038/ngeo1466>
- 831 Syracuse, E. M., van Keken, P. E., Abers, G. A., Suetsugu, D., Bina, C., Inoue, T., et al. (2010). The global range of  
832 subduction zone thermal models. *Physics of the Earth and Planetary Interiors*, 183(1–2), 73–90.  
833 <https://doi.org/10.1016/j.pepi.2010.02.004>
- 834 Takemoto, T., Furumura, T., Saito, T., Maeda, T., & Noguchi, S. (2012). Spatial- and frequency-dependent  
835 properties of site amplification factors in Japan derived by the coda normalization method. *Bulletin of the*  
836 *Seismological Society of America*, 102(4), 1462–1476. <https://doi.org/10.1785/0120110188>
- 837 Takemura, S., Furumura, T., & Saito, T. (2009). Distortion of the apparent *S*-wave radiation pattern in the high-  
838 frequency wavefield: Tottori-Ken Seibu, Japan, earthquake of 2000. *Geophysical Journal International*,  
839 178(2), 950–961. <https://doi.org/10.1111/j.1365-246X.2009.04210.x>
- 840 Takemura, Shunsuke. (2023). Estimated site amplifications at DONET stations, 1D velocity models, and movies for  
841 seismic wave propagation in a local 1D models [Data set]. <https://doi.org/10.5281/zenodo.10030902>
- 842 Takemura, Shunsuke, Kobayashi, M., & Yoshimoto, K. (2016). Prediction of maximum P- and S-wave amplitude  
843 distributions incorporating frequency- and distance-dependent characteristics of the observed apparent  
844 radiation patterns. *Earth, Planets and Space*, 68(1), 166. <https://doi.org/10.1186/s40623-016-0544-8>
- 845 Takemura, Shunsuke, Matsuzawa, T., Noda, A., Tonegawa, T., Asano, Y., Kimura, T., & Shiomi, K. (2019).  
846 Structural Characteristics of the Nankai Trough Shallow Plate Boundary Inferred From Shallow Very Low  
847 Frequency Earthquakes. *Geophysical Research Letters*, 46(8), 4192–4201.  
848 <https://doi.org/10.1029/2019GL082448>
- 849 Takemura, Shunsuke, Okuwaki, R., Kubota, T., Shiomi, K., Kimura, T., & Noda, A. (2020). Centroid moment  
850 tensor inversions of offshore earthquakes using a three-dimensional velocity structure model: slip distributions  
851 on the plate boundary along the Nankai Trough. *Geophysical Journal International*, 222(2), 1109–1125.  
852 <https://doi.org/10.1093/gji/ggaa238>
- 853 Takemura, Shunsuke, Yabe, S., & Emoto, K. (2020). Modelling high-frequency seismograms at ocean bottom  
854 seismometers: effects of heterogeneous structures on source parameter estimation for small offshore  
855 earthquakes and shallow low-frequency tremors. *Geophysical Journal International*, 223(3), 1708–1723.  
856 <https://doi.org/10.1093/gji/ggaa404>
- 857 Takemura, Shunsuke, Yoshimoto, K., & Shiomi, K. (2021). Long-period ground motion simulation using centroid  
858 moment tensor inversion solutions based on the regional three-dimensional model in the Kanto region, Japan.  
859 *Earth, Planets and Space*, 73(1), 15. <https://doi.org/10.1186/s40623-020-01348-2>
- 860 Takemura, Shunsuke, Baba, S., Yabe, S., Yamashita, Y., Shiomi, K., & Matsuzawa, T. (2022). Detectability  
861 analysis of very low frequency earthquakes: Methods and application in Nankai using F-net and DONET  
862 broadband seismometers. *Research Square*. Retrieved from <https://doi.org/10.21203/rs.3.rs-2351814/v1>
- 863 Takemura, Shunsuke, Baba, S., Yabe, S., Emoto, K., Shiomi, K., & Matsuzawa, T. (2022). Source Characteristics  
864 and Along-Strike Variations of Shallow Very Low Frequency Earthquake Swarms on the Nankai Trough

- 865 Shallow Plate Boundary. *Geophysical Research Letters*, 49(11), e2022GL097979.  
866 <https://doi.org/10.1029/2022GL097979>
- 867 Takemura, Shunsuke, Obara, K., Shiomi, K., & Baba, S. (2022). Spatiotemporal Variations of Shallow Very Low  
868 Frequency Earthquake Activity Southeast Off the Kii Peninsula, Along the Nankai Trough, Japan. *Journal of*  
869 *Geophysical Research: Solid Earth*, 127(3), e2021JB023073. <https://doi.org/10.1029/2021JB023073>
- 870 Takemura, Shunsuke, Hamada, Y., Okuda, H., Okada, Y., Okubo, K., Akuhara, T., et al. (2023). A review of  
871 shallow slow earthquakes along the Nankai Trough. *Earth, Planets and Space*, 75(1), 164.  
872 <https://doi.org/10.1186/s40623-023-01920-6>
- 873 Takemura, Shunsuke, Emoto, K., & Yamaya, L. (2023). High-frequency S and S-coda waves at ocean-bottom  
874 seismometers. *Earth, Planets and Space*, 75(1), 20. <https://doi.org/10.1186/s40623-023-01778-8>
- 875 Takeo, A., Idehara, K., Iritani, R., Tonegawa, T., Nagaoka, Y., Nishida, K., et al. (2010). Very broadband analysis  
876 of a swarm of very low frequency earthquakes and tremors beneath Kii Peninsula, SW Japan. *Geophysical*  
877 *Research Letters*, 37(6), L06311. <https://doi.org/10.1029/2010GL042586>
- 878 Tamaribuchi, K., Ogiso, M., & Noda, A. (2022). Spatiotemporal Distribution of Shallow Tremors along the Nankai  
879 Trough, Southwest Japan, as Determined from Waveform Amplitudes and Cross-Correlations. *Journal of*  
880 *Geophysical Research: Solid Earth*. <https://doi.org/10.1029/2022JB024403>
- 881 Tian, D. (2020). HinetPy: A Python package to request and process seismic waveform data from Hi-net.  
882 <https://doi.org/10.5281/zenodo.3885779>
- 883 Todd, E. K., Schwartz, S. Y., Mochizuki, K., Wallace, L. M., Sheehan, A. F., Webb, S. C., et al. (2018).  
884 Earthquakes and Tremor Linked to Seamount Subduction During Shallow Slow Slip at the Hikurangi Margin,  
885 New Zealand. *Journal of Geophysical Research: Solid Earth*. <https://doi.org/10.1029/2018JB016136>
- 886 Toh, A., Capdeville, Y., Chi, W. -C., & Ide, S. (2023). Strongly Scattering Medium Along Slow Earthquake Fault  
887 Zones Based on New Observations of Short-Duration Tremors. *Geophysical Research Letters*, 50(8).  
888 <https://doi.org/10.1029/2022GL101851>
- 889 Tonegawa, T., Araki, E., Kimura, T., Nakamura, T., Nakano, M., & Suzuki, K. (2017). Sporadic low-velocity  
890 volumes spatially correlate with shallow very low frequency earthquake clusters. *Nature Communications*,  
891 8(1), 2048. <https://doi.org/10.1038/s41467-017-02276-8>
- 892 Trugman, D. T., Chu, S. X., & Tsai, V. C. (2021). Earthquake Source Complexity Controls the Frequency  
893 Dependence of Near-Source Radiation Patterns. *Geophysical Research Letters*, 48(17).  
894 <https://doi.org/10.1029/2021GL095022>
- 895 Vaca, S., Vallée, M., Nocquet, J. M., Battaglia, J., & Régnier, M. (2018). Recurrent slow slip events as a barrier to  
896 the northward rupture propagation of the 2016 Pedernales earthquake (Central Ecuador). *Tectonophysics*, 724–  
897 725(November 2017), 80–92. <https://doi.org/10.1016/j.tecto.2017.12.012>
- 898 Virtanen, P., Gommers, R., Oliphant, T. E., Haberland, M., Reddy, T., Cournapeau, D., et al. (2020). SciPy 1.0:  
899 fundamental algorithms for scientific computing in Python. *Nature Methods*, 17(3), 261–272.  
900 <https://doi.org/10.1038/s41592-019-0686-2>
- 901 Voss, N., Dixon, T. H., Liu, Z., Malservisi, R., Protti, M., & Schwartz, S. (2018). Do slow slip events trigger large  
902 and great megathrust earthquakes ? *Science Advances*, 4(10), eaat8472.
- 903 Walter, J. I., Schwartz, S. Y., Protti, M., & Gonzalez, V. (2013). The synchronous occurrence of shallow tremor and  
904 very low frequency earthquakes offshore of the Nicoya Peninsula, Costa Rica. *Geophysical Research Letters*,  
905 40(8), 1517–1522. <https://doi.org/10.1002/grl.50213>
- 906 Wech, A. G. (2021). Cataloging Tectonic Tremor Energy Radiation in the Cascadia Subduction Zone. *Journal of*  
907 *Geophysical Research: Solid Earth*, 126(10). <https://doi.org/10.1029/2021JB022523>
- 908 Wessel, P., Smith, W. H. F., Scharroo, R., Luis, J., & Wobbe, F. (2013). Generic mapping tools: Improved version  
909 released. *Eos*, 94(45), 409–410. <https://doi.org/10.1002/2013EO450001>
- 910 Yabe, S., & Ide, S. (2014). Spatial distribution of seismic energy rate of tectonic tremors in subduction zones.  
911 *Journal of Geophysical Research: Solid Earth*, 119(11), 8171–8185. <https://doi.org/10.1002/2014JB011383>
- 912 Yabe, S., Tonegawa, T., & Nakano, M. (2019). Scaled Energy Estimation for Shallow Slow Earthquakes. *Journal of*  
913 *Geophysical Research: Solid Earth*, 124(2), 1507–1519. <https://doi.org/10.1029/2018JB016815>
- 914 Yabe, S., Baba, S., Tonegawa, T., Nakano, M., & Takemura, S. (2021). Seismic energy radiation and along-strike  
915 heterogeneities of shallow tectonic tremors at the Nankai Trough and Japan Trench. *Tectonophysics*, 800,  
916 228714. <https://doi.org/10.1016/j.tecto.2020.228714>
- 917 Yamamoto, Y., Ariyoshi, K., Yada, S., Nakano, M., & Hori, T. (2022). Spatio-temporal distribution of shallow very-  
918 low-frequency earthquakes between December 2020 and January 2021 in Kumano-nada, Nankai subduction  
919 zone, detected by a permanent seafloor seismic network. *Earth, Planets and Space*, 74(1), 14.  
920 <https://doi.org/10.1186/s40623-022-01573-x>

921 Yoshida, K., Emoto, K., Takemura, S., & Matsuzawa, T. (2023). Near-Source Waveform Modeling to Estimate  
922 Shallow Crustal Attenuation and Radiated Energy of Mw 2.0-4.5 Earthquakes. *ESS Open Archive*.  
923 <https://doi.org/10.22541/essoar.170326156.62618173/v1>  
924

Figure 1.

(a)



(b)

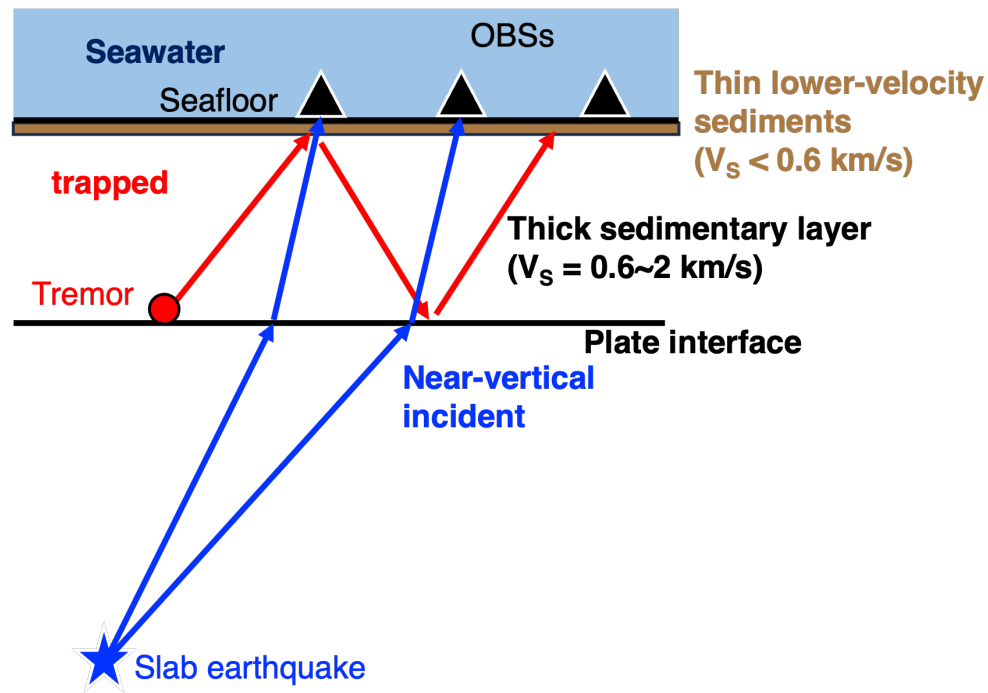
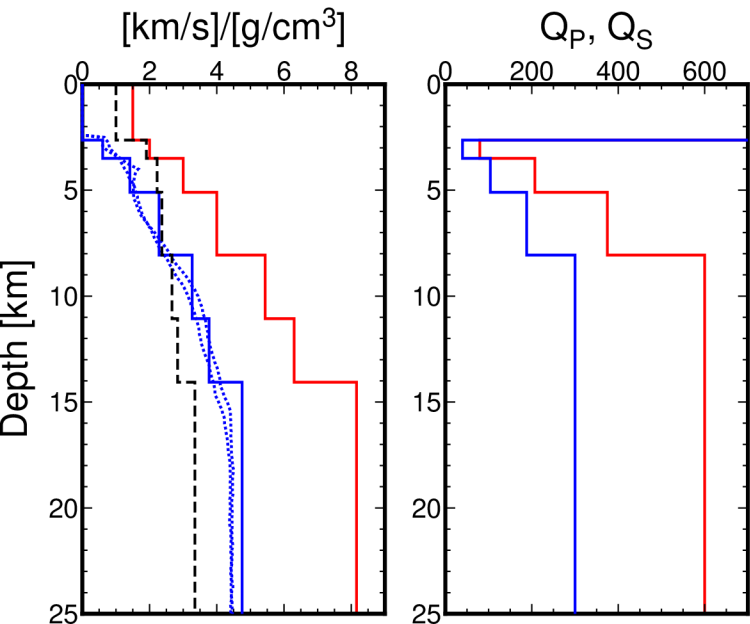


Figure 2.

(a) DONET1D



(b) DONET1D'

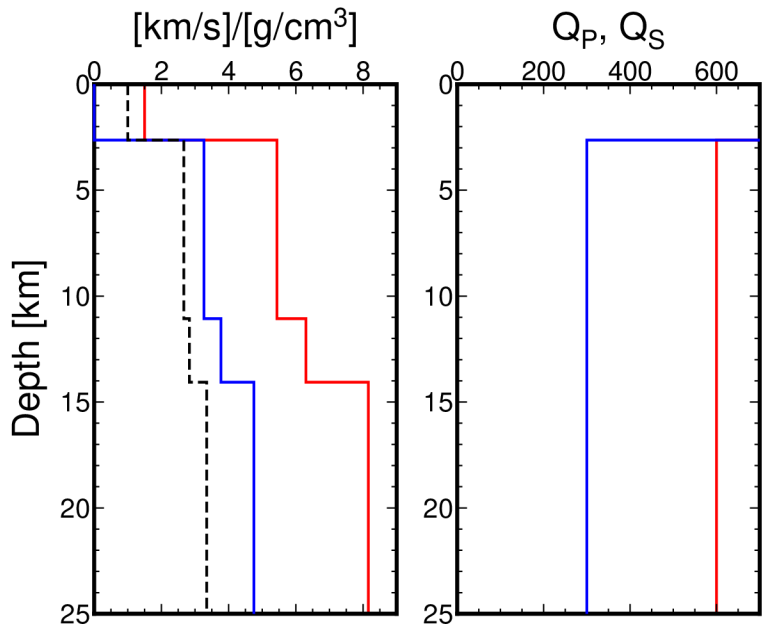


Figure 3.

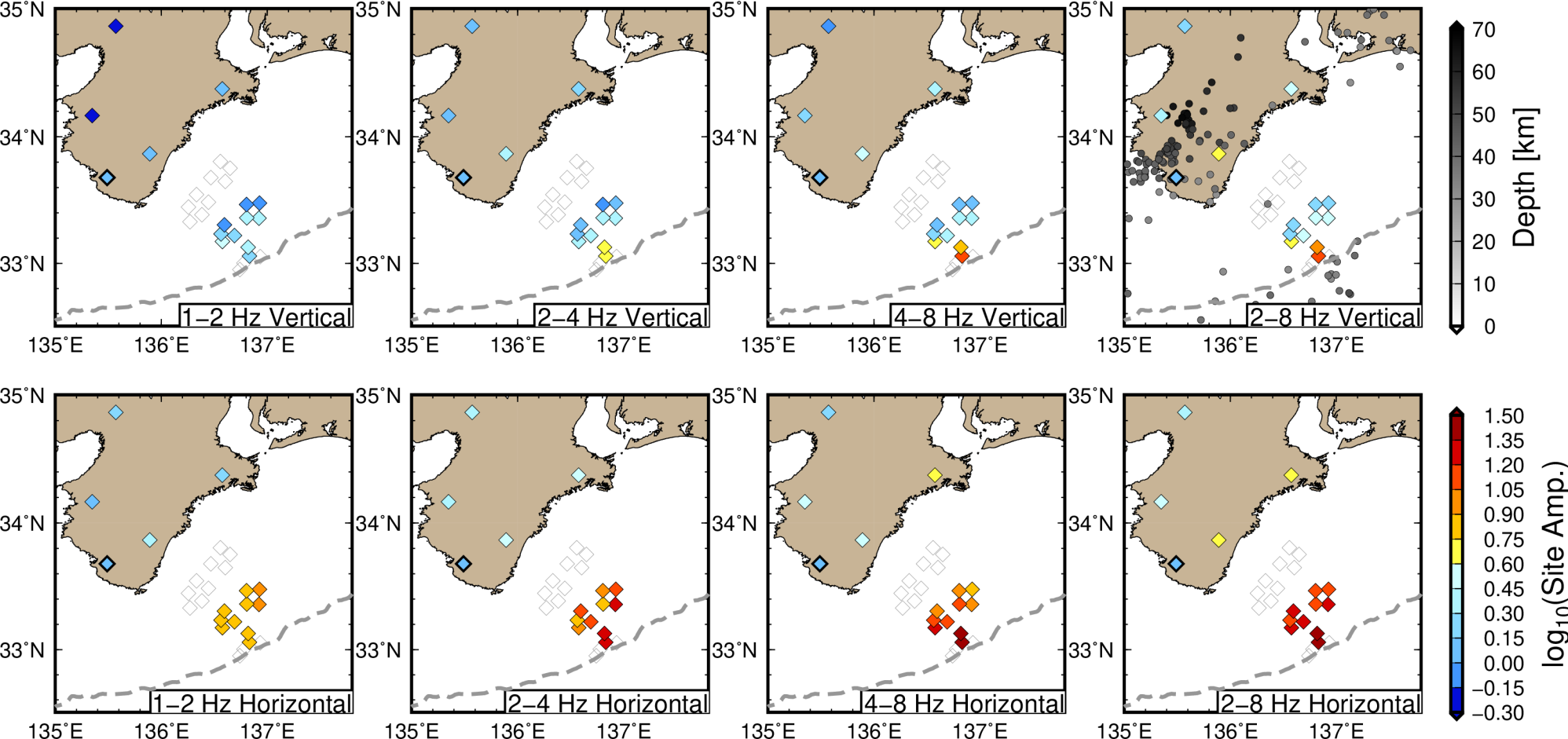


Figure 4.

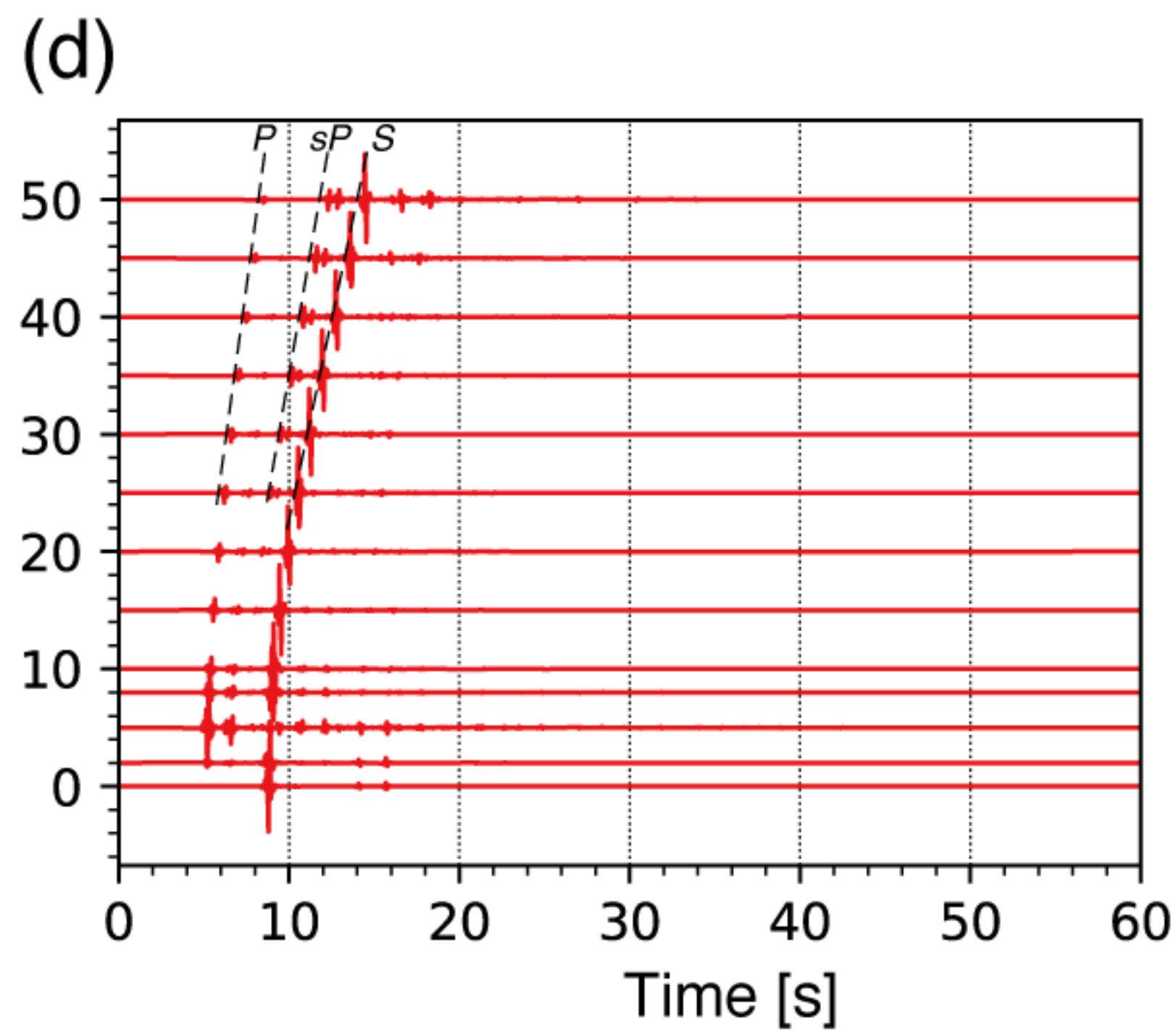
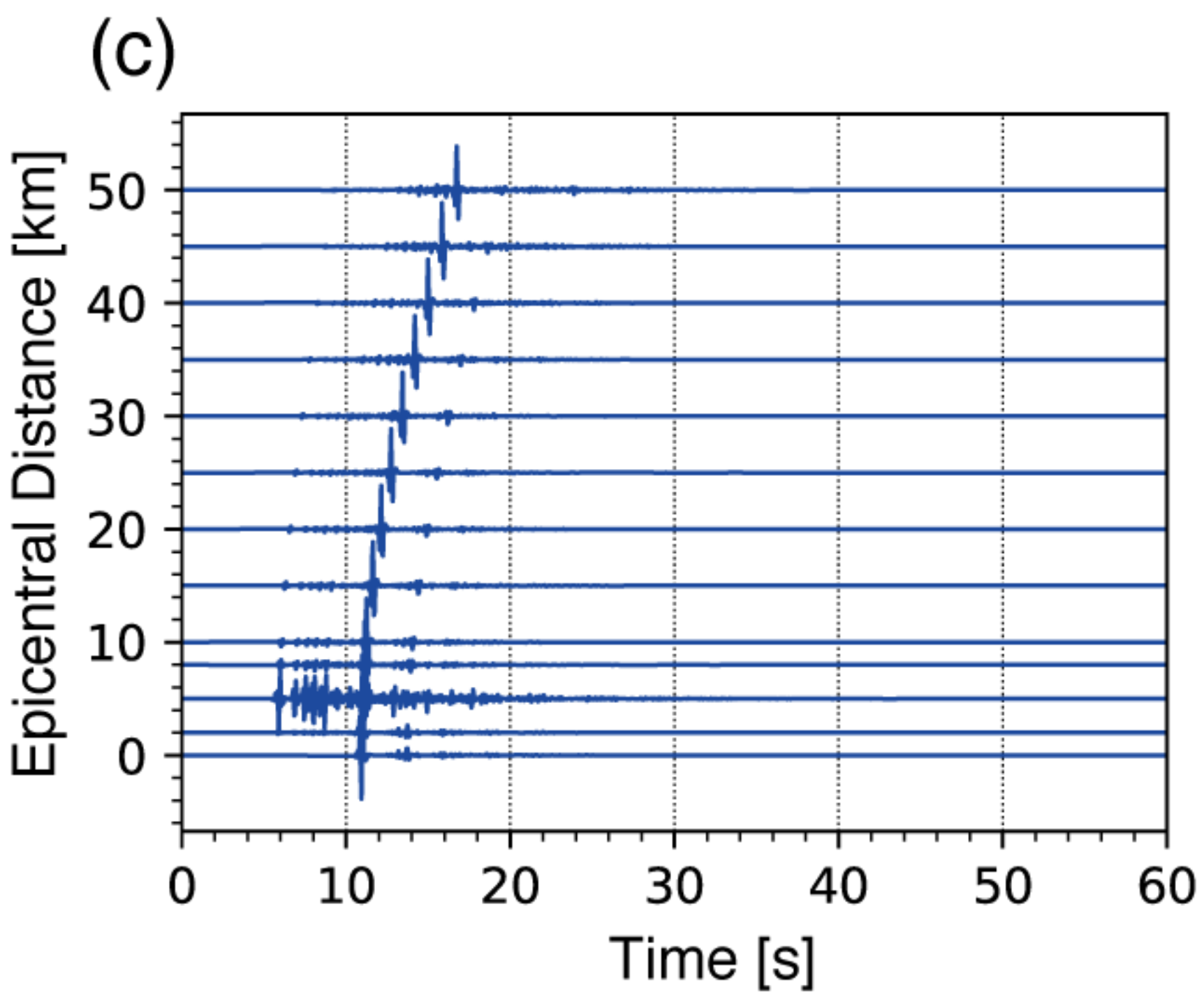
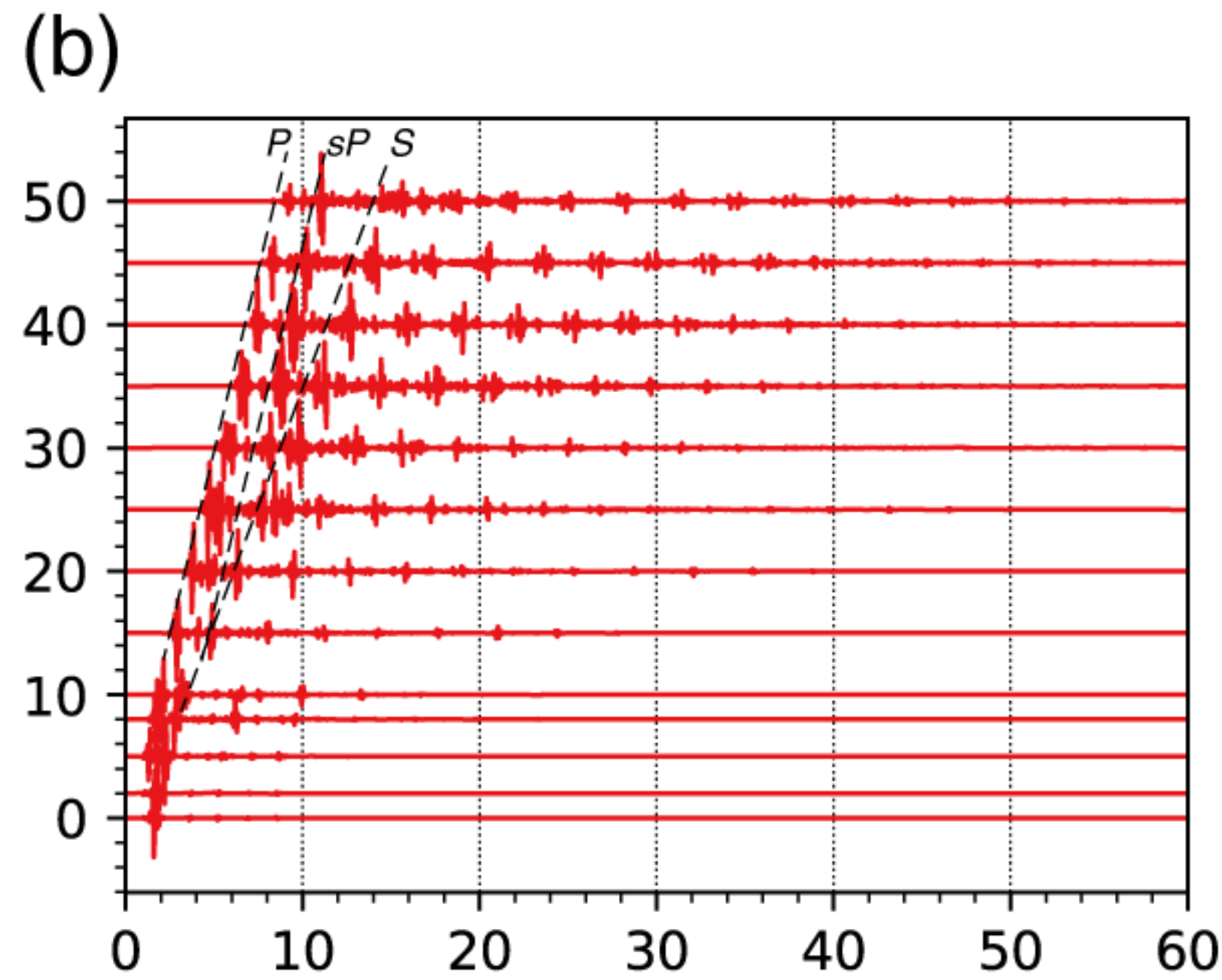
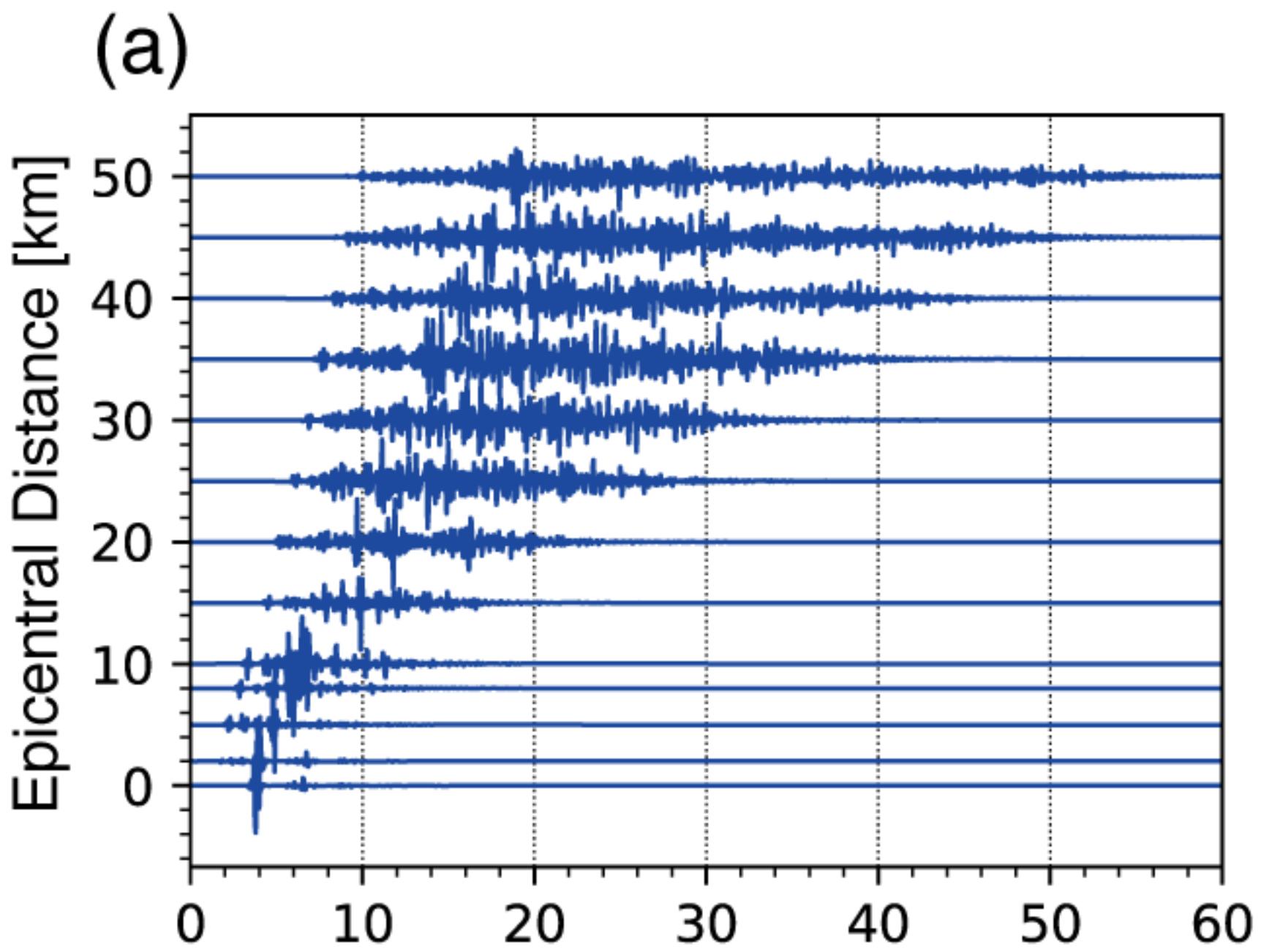


Figure 5.

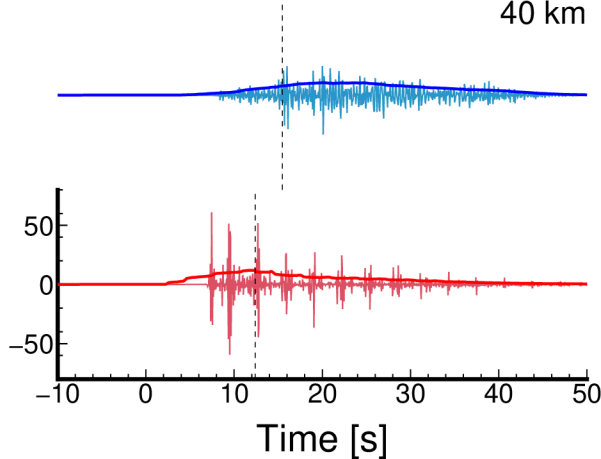
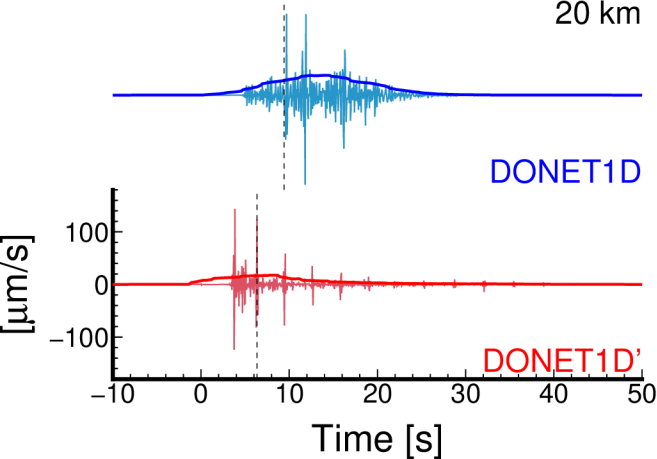


Figure 6.

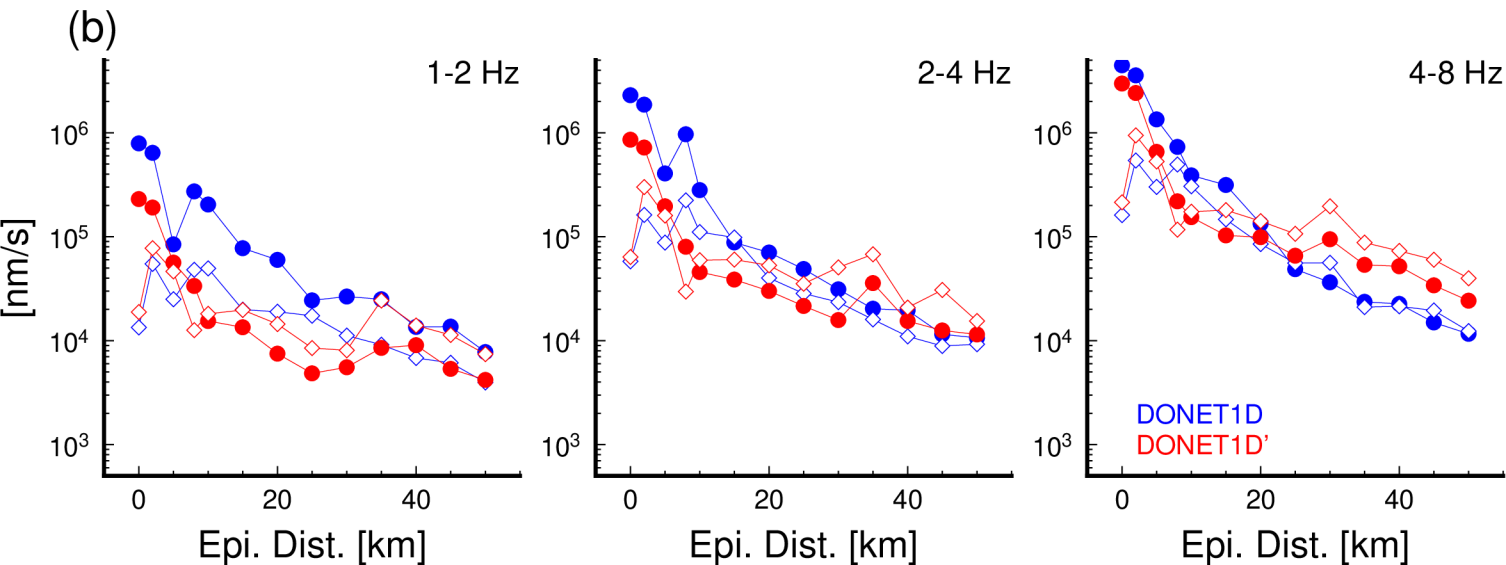
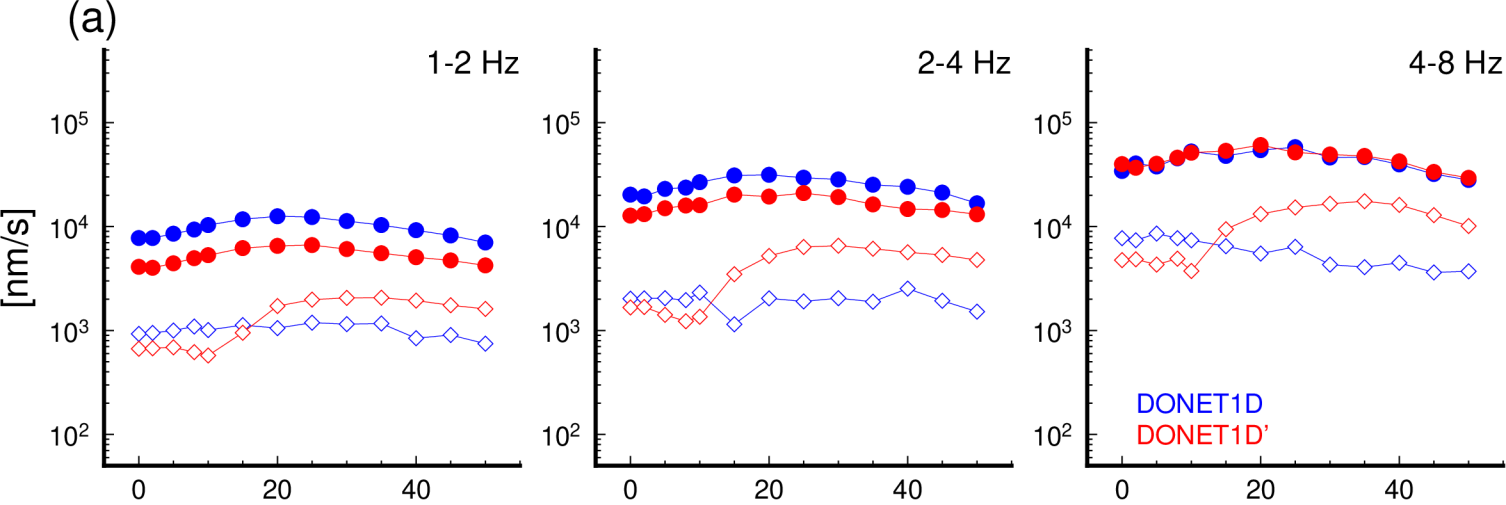
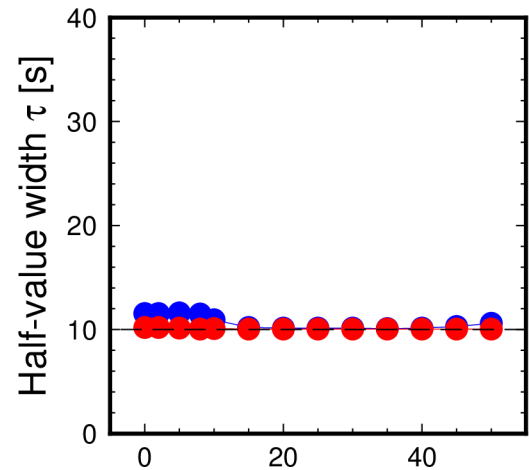
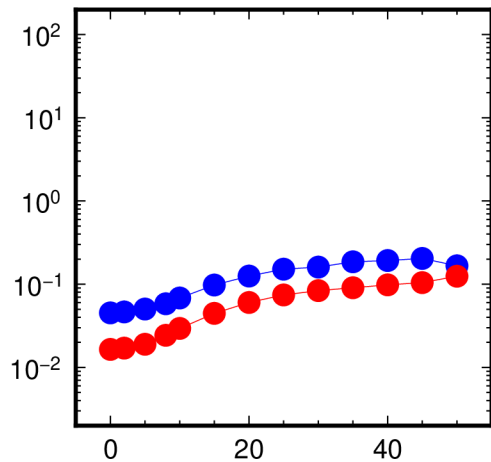
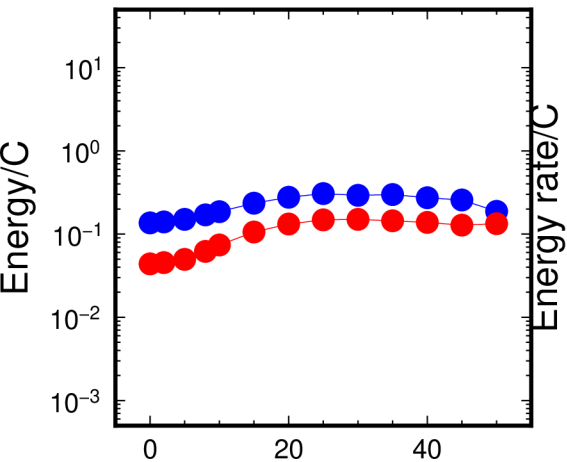


Figure 7.

(a)



(b)

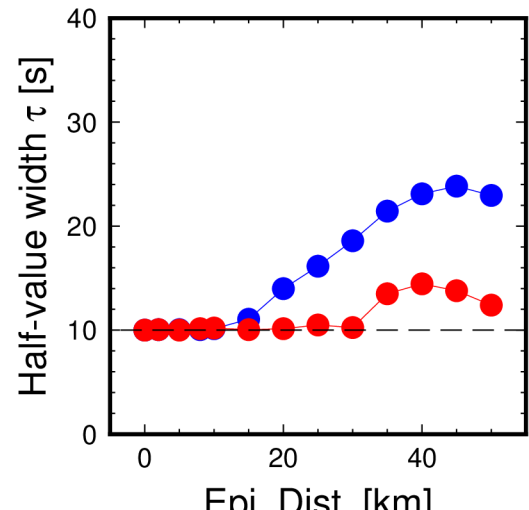
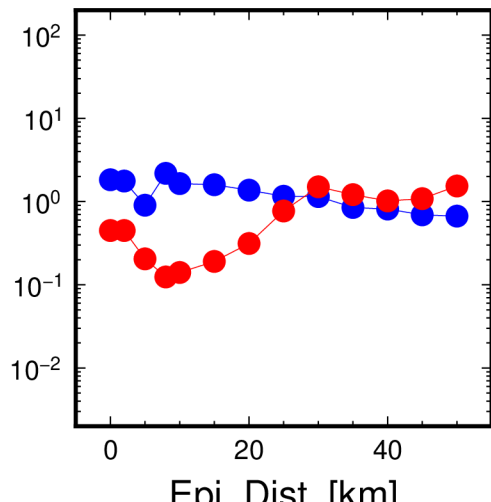
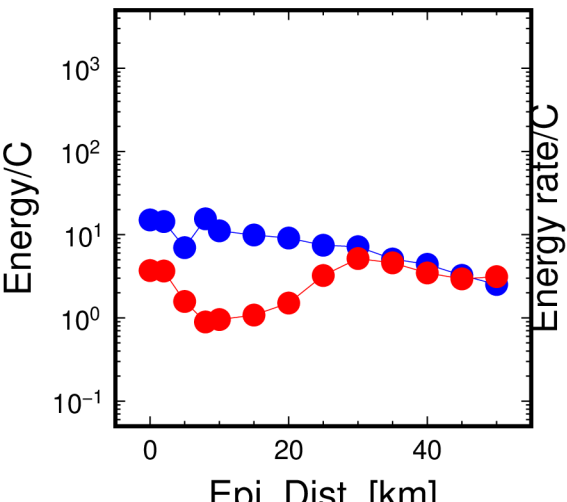


Figure 8.

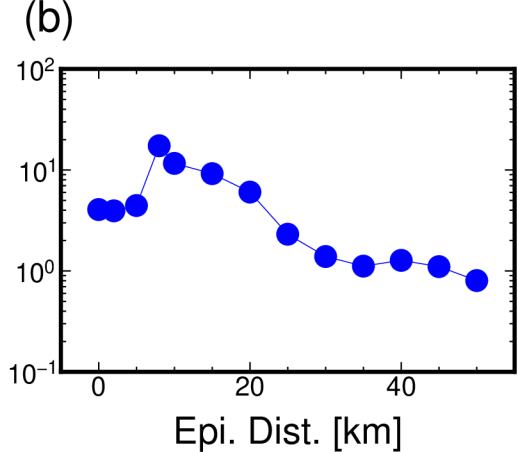
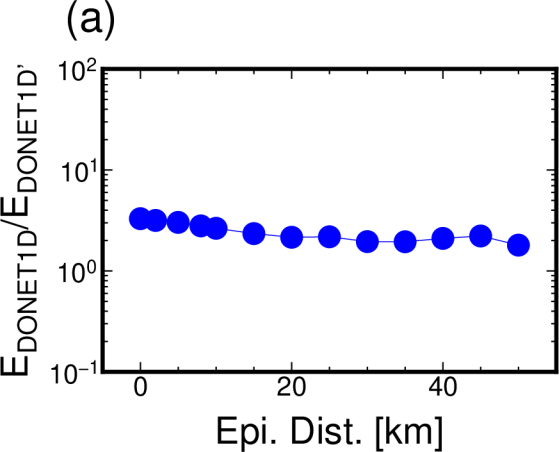


Figure 9.

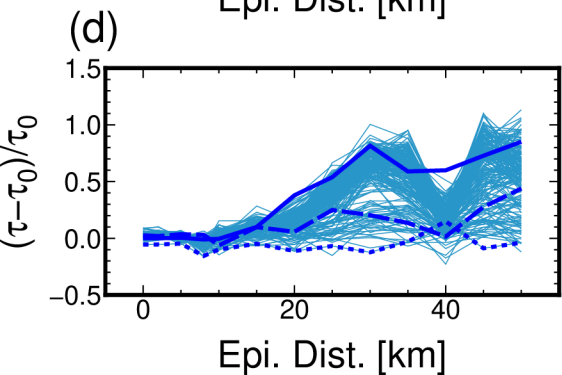
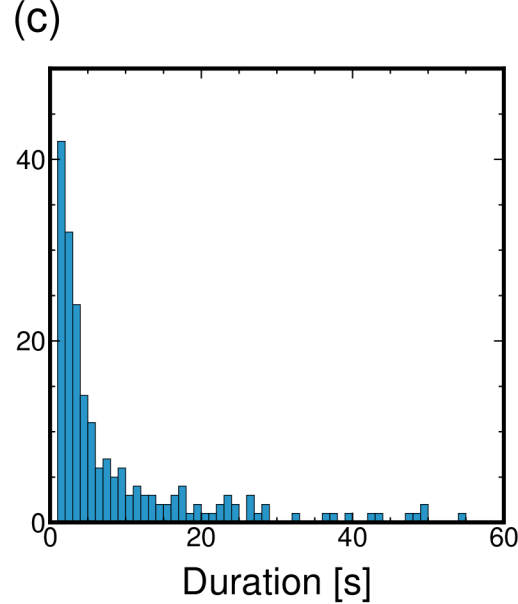
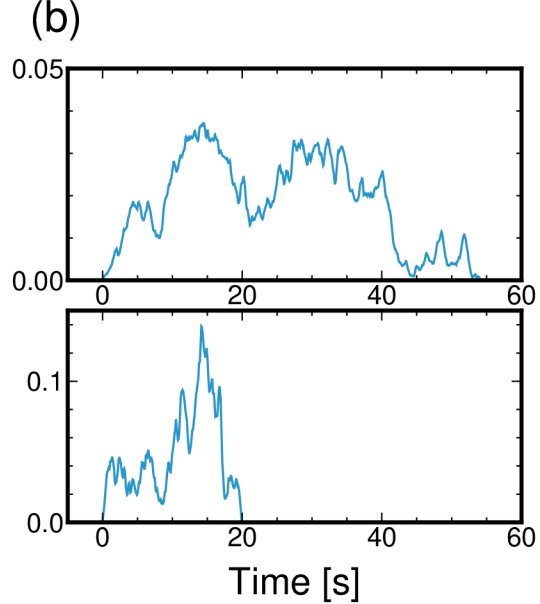
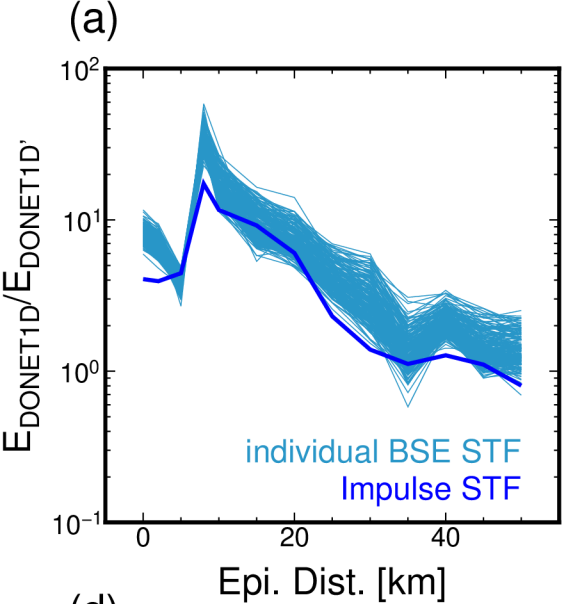


Figure 10.

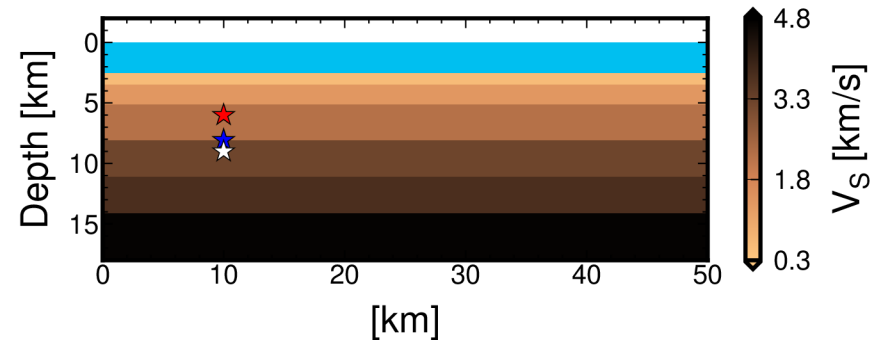
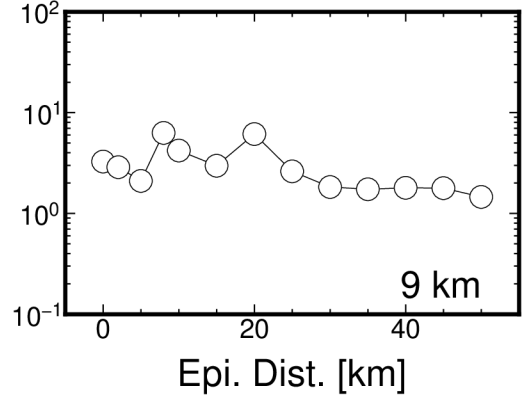
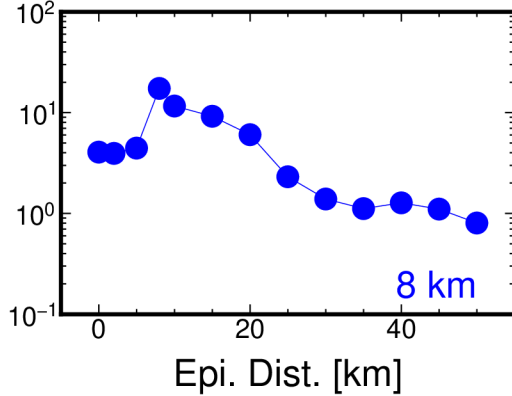
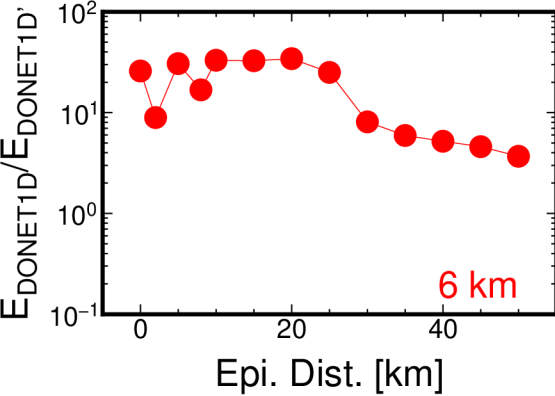


Figure 11.

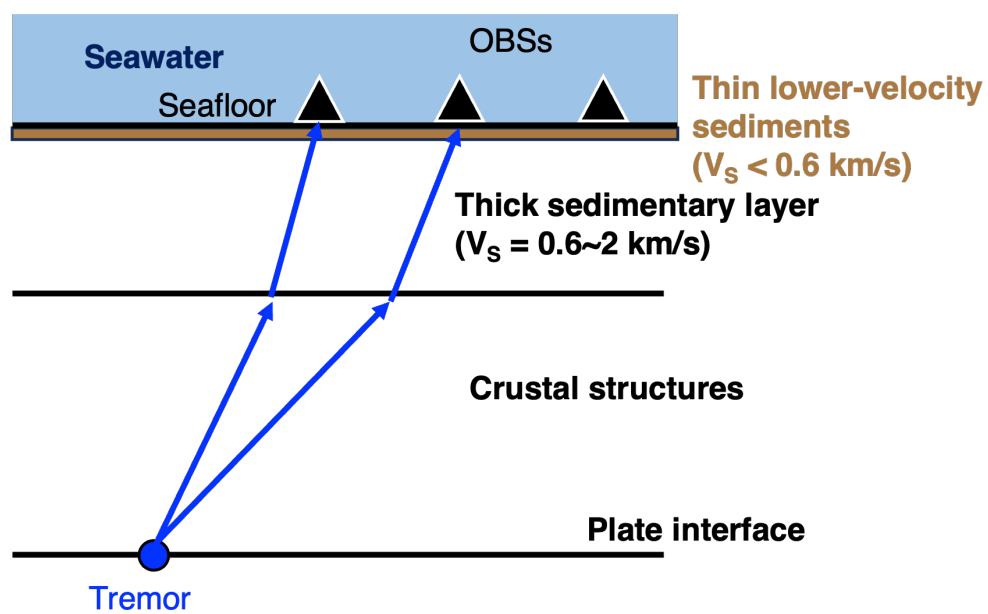
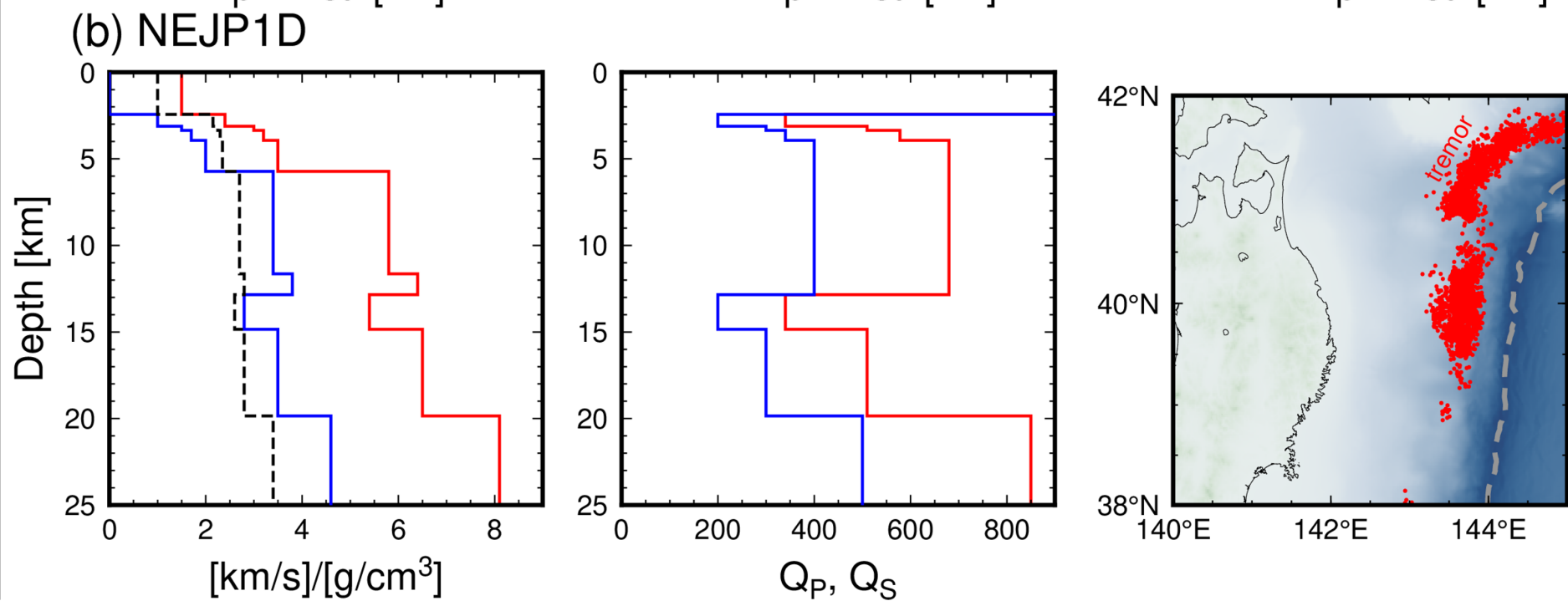
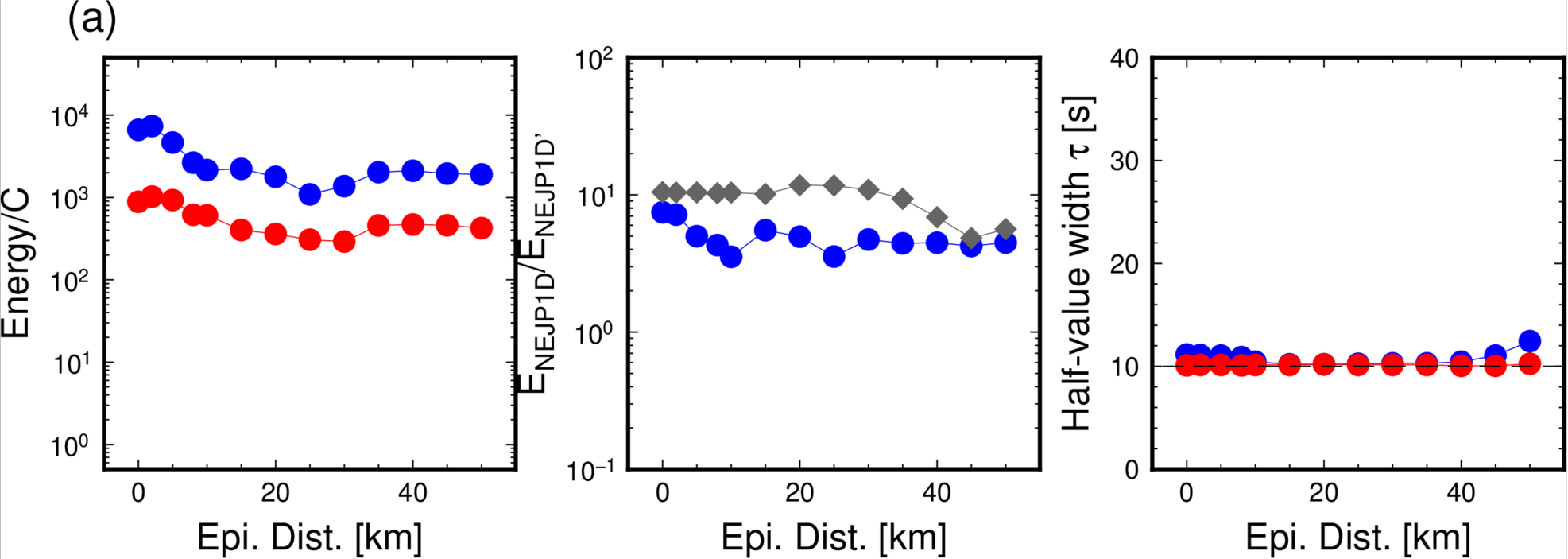
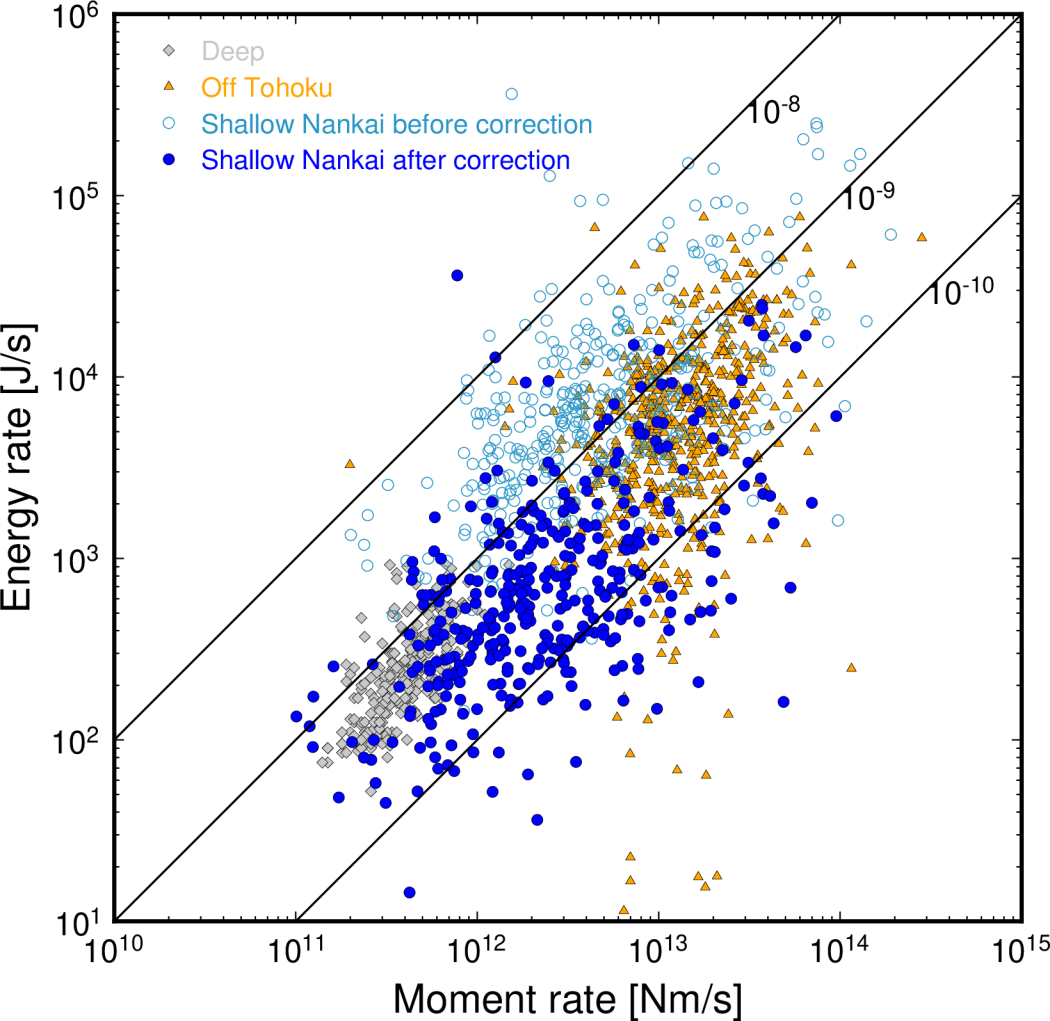


Figure 12.



## **Revisiting seismic energy of shallow tremors: amplifications due to site and propagation path effects near the Nankai Trough**

Shunsuke Takemura<sup>1</sup>, Kentaro Emoto<sup>2</sup>, and, Suguru Yabe<sup>3</sup>

<sup>1</sup> Earthquake Research Institute, University of Tokyo, 1-1-1 Yayoi, Bunkyo-ku, Tokyo 113-0032, Japan, <sup>2</sup> Geophysics, Graduate School of Science, Tohoku University, 6-3, Aramaki-aza-aoba, Aoba-ku, Sendai 980-8578, Japan, <sup>3</sup> Geological Survey of Japan, National Institute of Advanced Industrial Science and Technology, Tsukuba Central 7, 1-1-1 Higashi, Tsukuba, Ibaraki 305-8567, Japan

### **Contents of this file**

Table S1

Figure S1

### **Additional Supporting Information (Files uploaded separately)**

Caption for Figure S1

Captions for Movies S1 to S4

### **Introduction**

Figure S1 shows distance-dependent characteristics of seismic energy amplifications for DONET1Dq, where the  $Q_s$  of the shallowest layer is set as 20.

Simulated wavefields for shallow tremors and intraslab earthquakes in DONET1D and DONET1D' are shown in Movies S1–S4. Movies can be available using the VLC player [https://www.videolan.org/vlc/index.en\\_GB.html](https://www.videolan.org/vlc/index.en_GB.html). The intraslab earthquakes used to estimate the site amplification factors are listed in Table S1.

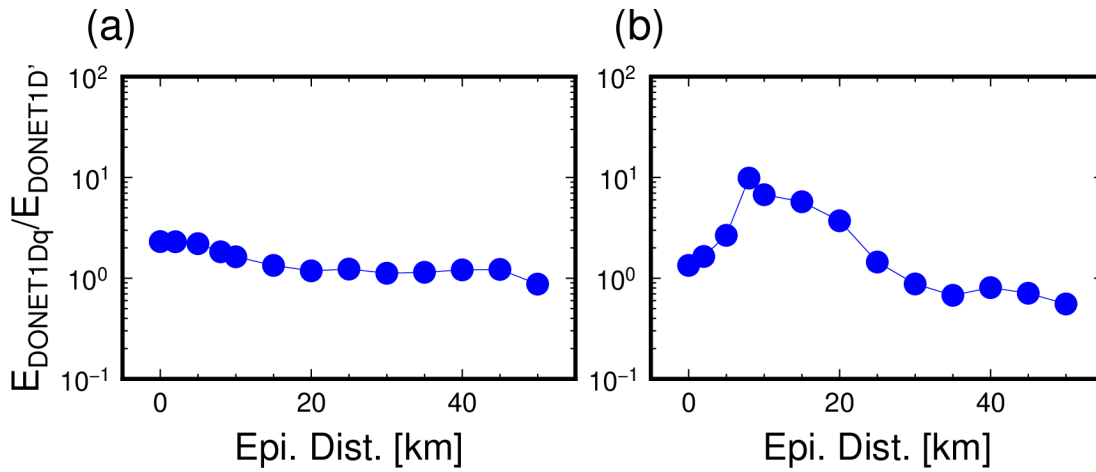


**Figure S1.** Ratio of seismic energies between DONET1Dq and DONET1D' for (a) intraslab earthquake and (b) shallow tremor sources. DONET1Dq is a similar 1D model of DONET1D, but  $Q_s$  value within the shallowest layer of DONET1Dq is 20.

**Movie S1.** Simulated wavefield for a shallow tremor in DONET1D. Red and green particles denote the divergence ( $P$ ) and rotation ( $S$ ) of the wavefield, respectively.

**Movie S2.** Simulated wavefield for a shallow tremor in DONET1D'. Red and green particles denote the divergence ( $P$ ) and rotation ( $S$ ) of the wavefield, respectively.

**Movie S3.** Simulated wavefield for an intraslab earthquake in DONET1D. Red and green particles denote the divergence ( $P$ ) and rotation ( $S$ ) of the wavefield, respectively.

**Movie S4.** Simulated wavefield for an intraslab earthquake in DONET1D'. Red and green particles denote the divergence ( $P$ ) and rotation ( $S$ ) of the wavefield, respectively.

**Table S1.** Source information for intraslab earthquakes used for site amplification estimation. The origin date and time are written in JST.

| <i>Date</i> | <i>Time</i> | <i>Longitude [°]</i> | <i>Latitude [°]</i> | <i>Depth [km]</i> | <i>M<sub>JMA</sub></i> |
|-------------|-------------|----------------------|---------------------|-------------------|------------------------|
| 2016-05-29  | 10:55:09.60 | 135.6115             | 34.2587             | 63.04             | 3.6                    |
| 2016-07-30  | 06:31:01.69 | 137.0077             | 33.0127             | 35.81             | 3.1                    |
| 2016-08-01  | 15:52:39.88 | 135.3287             | 33.8410             | 48.40             | 3.3                    |
| 2016-08-27  | 15:20:03.57 | 136.0072             | 34.0132             | 41.47             | 3.2                    |
| 2016-08-31  | 08:59:11.18 | 135.6160             | 33.8263             | 51.13             | 3.9                    |
| 2016-09-03  | 15:03:17.48 | 135.1423             | 33.7137             | 42.70             | 4.0                    |
| 2016-11-03  | 17:50:21.24 | 135.9723             | 32.0987             | 31.00             | 3.7                    |
| 2016-11-19  | 11:48:01.47 | 135.4635             | 33.8427             | 51.35             | 5.4                    |
| 2016-11-19  | 17:51:18.80 | 135.4757             | 33.8013             | 46.36             | 3.3                    |
| 2016-12-09  | 01:13:10.67 | 136.3970             | 34.2450             | 33.94             | 3.5                    |
| 2016-12-16  | 05:22:53.99 | 135.5888             | 34.1840             | 67.78             | 3.6                    |
| 2017-01-03  | 04:52:33.65 | 135.3233             | 33.8132             | 47.90             | 3.1                    |
| 2017-01-04  | 17:16:36.13 | 136.0728             | 34.6232             | 57.57             | 3.3                    |
| 2017-01-16  | 00:52:26.20 | 135.7475             | 34.1997             | 59.00             | 3.5                    |
| 2017-01-24  | 23:52:53.73 | 135.1577             | 33.6623             | 37.44             | 3.0                    |
| 2017-02-11  | 08:02:11.59 | 135.8538             | 32.1613             | 30.00             | 3.0                    |
| 2017-02-23  | 13:01:33.47 | 135.1200             | 33.8100             | 47.59             | 3.7                    |
| 2017-04-24  | 22:58:22.23 | 137.9095             | 34.8970             | 34.47             | 3.9                    |
| 2017-06-16  | 00:25:28.03 | 135.5653             | 34.1815             | 65.24             | 3.0                    |
| 2017-07-05  | 13:48:36.15 | 135.5068             | 34.1065             | 66.08             | 3.1                    |
| 2017-07-07  | 06:43:26.42 | 136.9525             | 32.9148             | 33.88             | 3.2                    |
| 2017-07-16  | 23:13:12.46 | 137.3163             | 34.9807             | 41.48             | 3.0                    |
| 2017-07-23  | 23:58:22.81 | 137.1037             | 34.8127             | 34.93             | 3.0                    |
| 2017-08-06  | 05:07:34.46 | 136.8163             | 32.3892             | 44.10             | 3.4                    |
| 2017-09-17  | 08:28:8.32  | 135.6072             | 34.1327             | 62.77             | 3.9                    |
| 2017-09-21  | 01:02:45.98 | 135.4465             | 33.9680             | 55.57             | 4.1                    |
| 2017-09-22  | 23:14:34.83 | 135.8982             | 33.9543             | 52.23             | 3.1                    |
| 2017-10-05  | 18:09:24.61 | 135.3287             | 33.6730             | 45.95             | 3.2                    |
| 2017-10-10  | 06:59:23.21 | 137.3517             | 34.9952             | 38.27             | 3.1                    |
| 2017-10-25  | 06:48:51.95 | 135.4492             | 33.7955             | 43.02             | 3.3                    |
| 2017-10-30  | 20:56:3.31  | 135.4495             | 33.8103             | 42.66             | 3.5                    |
| 2017-11-05  | 03:05:11.17 | 135.6110             | 34.0542             | 58.87             | 3.0                    |
| 2017-12-20  | 21:44:09.01 | 136.9515             | 32.8773             | 32.12             | 3.9                    |
| 2018-01-20  | 11:05:06.25 | 135.7225             | 32.5497             | 38.40             | 3.7                    |
| 2018-01-20  | 11:47:17.94 | 137.9612             | 32.0643             | 46.00             | 3.7                    |
| 2018-02-27  | 09:10:07.84 | 135.0333             | 32.7602             | 42.31             | 3.2                    |
| 2018-03-18  | 13:24:17.87 | 135.6997             | 33.6500             | 32.17             | 3.0                    |
| 2018-03-27  | 21:08:01.40 | 135.5690             | 33.6662             | 35.70             | 3.2                    |
| 2018-04-10  | 11:25:30.68 | 135.6928             | 32.1557             | 33.00             | 3.3                    |
| 2018-04-14  | 13:51:12.49 | 137.2903             | 34.9500             | 39.62             | 3.2                    |
| 2018-04-16  | 17:55:00.90 | 135.8097             | 33.4867             | 30.01             | 3.4                    |

|            |             |          |         |       |     |
|------------|-------------|----------|---------|-------|-----|
| 2018-05-12 | 12:40:53.50 | 136.7045 | 34.7423 | 40.20 | 3.8 |
| 2018-05-14 | 03:12:35.87 | 135.6238 | 34.0133 | 55.10 | 3.3 |
| 2018-05-28 | 15:03:22.18 | 136.0337 | 34.2258 | 52.73 | 3.3 |
| 2018-08-06 | 05:48:24.54 | 135.1603 | 33.8680 | 50.38 | 3.1 |
| 2018-08-14 | 20:51:00.92 | 137.4970 | 34.7520 | 37.22 | 3.9 |
| 2018-08-20 | 01:42:29.11 | 135.5930 | 34.1168 | 64.27 | 3.1 |
| 2018-10-27 | 20:51:50.57 | 135.8245 | 34.4250 | 62.24 | 4.2 |
| 2018-11-02 | 01:07:46.30 | 135.6375 | 34.1012 | 62.88 | 3.3 |
| 2018-11-05 | 08:19:16.85 | 135.2842 | 33.7275 | 45.11 | 4.6 |
| 2018-11-05 | 18:12:30.88 | 135.1957 | 33.7077 | 42.30 | 3.6 |
| 2018-11-06 | 03:39:01.58 | 135.1560 | 33.6433 | 42.77 | 3.2 |
| 2018-11-09 | 00:13:49.93 | 135.4572 | 33.8830 | 48.12 | 3.0 |
| 2018-12-03 | 17:08:23.13 | 135.4080 | 33.8662 | 48.00 | 4.0 |
| 2018-12-04 | 07:07:19.83 | 135.1980 | 33.6827 | 41.42 | 3.0 |
| 2019-01-25 | 18:08:03.52 | 136.9972 | 32.9090 | 33.89 | 3.5 |
| 2019-01-27 | 20:19:37.66 | 136.6713 | 32.0337 | 34.28 | 3.2 |
| 2019-02-12 | 22:49:57.04 | 135.7885 | 34.0170 | 48.01 | 3.3 |
| 2019-04-10 | 12:44:33.15 | 135.2033 | 33.8200 | 46.29 | 3.1 |
| 2019-04-14 | 01:29:14.25 | 135.7805 | 34.3572 | 58.24 | 3.2 |
| 2019-05-02 | 06:22:13.34 | 135.4898 | 33.9300 | 52.29 | 3.1 |
| 2019-05-14 | 10:50:01.19 | 137.1330 | 32.7535 | 42.05 | 3.4 |
| 2019-05-24 | 13:25:11.38 | 135.5797 | 34.0925 | 61.68 | 3.8 |
| 2019-05-26 | 16:59:37.08 | 137.9337 | 34.8473 | 30.40 | 3.2 |
| 2019-06-14 | 15:09:20.89 | 136.7683 | 32.6967 | 37.23 | 3.0 |
| 2019-06-24 | 01:13:42.49 | 136.1318 | 33.9458 | 44.33 | 3.1 |
| 2019-07-28 | 14:24:29.03 | 135.3892 | 33.8838 | 51.32 | 3.0 |
| 2019-09-07 | 19:38:20.53 | 137.2270 | 34.7012 | 30.40 | 3.2 |
| 2019-10-06 | 16:10:25.45 | 137.1738 | 33.0622 | 40.82 | 3.3 |
| 2019-10-24 | 03:11:55.73 | 135.3308 | 33.5642 | 31.37 | 3.8 |
| 2019-10-30 | 22:22:30.41 | 137.0157 | 34.8155 | 37.27 | 3.2 |
| 2019-10-31 | 19:20:38.60 | 135.1520 | 33.6778 | 37.00 | 3.6 |
| 2020-01-04 | 18:12:16.24 | 137.1328 | 34.4232 | 30.38 | 3.0 |
| 2020-01-09 | 06:29:23.65 | 137.4505 | 34.9502 | 40.48 | 3.0 |
| 2020-01-10 | 17:09:50.34 | 135.6445 | 34.0580 | 53.49 | 3.2 |
| 2020-01-14 | 12:44:09.98 | 137.8772 | 32.8767 | 50.63 | 3.3 |
| 2020-01-20 | 08:46:09.17 | 135.5055 | 33.9233 | 52.11 | 3.5 |
| 2020-01-23 | 16:13:07.98 | 137.8487 | 34.6848 | 33.90 | 3.7 |
| 2020-02-04 | 14:23:45.55 | 135.3710 | 33.7955 | 45.49 | 3.0 |
| 2020-02-24 | 19:32:36.22 | 136.2392 | 32.6712 | 40.26 | 3.1 |
| 2020-04-19 | 12:09:13.02 | 137.2342 | 34.7563 | 39.82 | 3.5 |
| 2020-05-22 | 03:19:12.47 | 137.0295 | 32.7815 | 39.61 | 3.7 |
| 2020-05-23 | 10:36:34.70 | 135.4628 | 33.5375 | 31.55 | 3.5 |
| 2020-05-29 | 06:24:36.14 | 135.9475 | 33.9307 | 42.34 | 3.5 |
| 2020-05-31 | 11:20:13.91 | 135.7135 | 33.9690 | 46.66 | 3.6 |
| 2020-06-09 | 14:12:14.98 | 135.9413 | 32.2078 | 37.00 | 3.5 |

|            |             |          |         |       |     |
|------------|-------------|----------|---------|-------|-----|
| 2020-06-14 | 10:25:54.53 | 135.4607 | 34.2367 | 64.58 | 3.2 |
| 2020-07-11 | 03:19:29.84 | 137.5643 | 34.6728 | 30.32 | 3.7 |
| 2020-07-11 | 03:43:44.02 | 137.5720 | 34.6697 | 30.18 | 3.0 |
| 2020-08-01 | 12:15:07.59 | 135.4473 | 33.7885 | 46.28 | 4.2 |
| 2020-08-09 | 20:32:49.80 | 136.8802 | 32.5308 | 41.99 | 3.0 |
| 2020-09-01 | 05:12:22.26 | 135.0435 | 33.3560 | 37.42 | 3.3 |
| 2020-09-11 | 18:27:55.32 | 135.8587 | 32.6990 | 32.63 | 3.3 |
| 2020-10-03 | 03:49:17.54 | 135.3870 | 33.8920 | 53.43 | 3.0 |
| 2020-10-26 | 06:34:59.34 | 135.5947 | 34.1735 | 66.66 | 4.0 |
| 2020-11-12 | 13:12:47.23 | 137.9518 | 32.6648 | 64.62 | 3.2 |
| 2020-12-25 | 07:16:19.93 | 135.8638 | 32.0208 | 64.04 | 3.3 |
| 2021-02-01 | 19:45:10.52 | 135.4368 | 33.8518 | 47.73 | 3.1 |
| 2021-02-08 | 02:26:23.34 | 135.2100 | 33.7835 | 46.10 | 3.8 |
| 2021-02-23 | 09:35:53.13 | 135.0290 | 33.7835 | 44.90 | 3.4 |
| 2021-04-02 | 06:22:11.72 | 135.4140 | 33.8773 | 46.75 | 3.4 |
| 2021-04-05 | 06:22:00.37 | 137.6985 | 34.6755 | 35.77 | 4.3 |
| 2021-04-05 | 14:16:39.49 | 136.3770 | 32.7467 | 41.21 | 3.0 |
| 2021-04-06 | 21:58:05.63 | 135.2333 | 33.7983 | 45.80 | 3.2 |
| 2021-04-10 | 19:17:26.72 | 135.4383 | 33.9092 | 52.61 | 3.5 |
| 2021-05-26 | 08:57:40.61 | 135.4085 | 33.9293 | 51.00 | 3.9 |
| 2021-06-10 | 22:15:54.09 | 135.0388 | 33.7208 | 38.79 | 3.5 |
| 2021-06-14 | 02:17:21.12 | 135.5453 | 34.1493 | 68.00 | 3.3 |
| 2021-06-30 | 07:04:09.70 | 135.3375 | 33.8623 | 52.00 | 3.2 |
| 2021-09-01 | 02:55:12.83 | 135.3603 | 33.8063 | 45.72 | 3.8 |
| 2021-09-09 | 11:18:05.54 | 135.8680 | 33.5433 | 30.78 | 3.2 |
| 2021-10-15 | 06:38:37.47 | 136.5473 | 32.9495 | 31.57 | 3.0 |
| 2021-10-15 | 16:53:28.62 | 136.0990 | 34.7732 | 56.38 | 3.6 |
| 2021-10-18 | 15:21:34.75 | 135.0762 | 33.7322 | 40.33 | 3.5 |
| 2021-11-15 | 13:11:48.94 | 135.2893 | 33.7845 | 43.20 | 3.0 |
| 2021-12-04 | 05:07:40.79 | 135.1378 | 33.8000 | 46.19 | 3.0 |
| 2021-12-09 | 15:25:13.07 | 135.4017 | 34.1677 | 66.95 | 3.5 |
| 2022-01-07 | 01:59:13.07 | 135.4020 | 33.9028 | 52.28 | 3.8 |
| 2022-01-09 | 18:00:56.39 | 137.2000 | 33.1753 | 39.40 | 3.3 |
| 2022-01-18 | 08:16:42.29 | 137.6012 | 34.5488 | 34.71 | 3.6 |
| 2022-01-28 | 00:25:08.05 | 135.5803 | 34.1048 | 58.69 | 3.9 |
| 2022-01-30 | 08:26:50.43 | 135.7095 | 33.9617 | 45.02 | 3.6 |
| 2022-01-30 | 15:45:04.10 | 135.9325 | 32.9343 | 31.26 | 3.3 |
| 2022-03-09 | 03:12:27.59 | 135.2288 | 33.3425 | 32.35 | 3.2 |
| 2022-03-21 | 06:44:36.16 | 136.9233 | 32.9030 | 37.38 | 3.4 |
| 2022-04-08 | 05:30:29.68 | 135.8563 | 33.5895 | 38.87 | 3.1 |
| 2022-04-09 | 11:13:21.24 | 135.4008 | 33.9040 | 52.26 | 3.7 |
| 2022-04-16 | 15:18:56.00 | 137.1197 | 32.7652 | 49.40 | 3.7 |
| 2022-05-02 | 12:50:23.75 | 135.2712 | 32.2723 | 52.10 | 3.0 |
| 2022-06-15 | 09:58:53.71 | 135.1987 | 33.7297 | 41.92 | 3.1 |
| 2022-06-26 | 06:31:25.37 | 135.9982 | 34.2227 | 55.02 | 3.4 |

|            |             |          |         |       |     |
|------------|-------------|----------|---------|-------|-----|
| 2022-06-28 | 19:16:04.18 | 135.0877 | 33.6450 | 41.91 | 3.4 |
| 2022-07-03 | 00:32:48.01 | 136.3540 | 33.4698 | 36.78 | 3.1 |
| 2022-07-15 | 17:50:33.08 | 136.9657 | 33.0387 | 38.00 | 3.1 |
| 2022-07-28 | 02:04:23.37 | 135.3247 | 33.8228 | 46.76 | 3.1 |
| 2022-09-30 | 16:14:37.42 | 135.4380 | 33.6640 | 40.94 | 3.1 |
| 2022-10-03 | 11:41:57.60 | 136.2500 | 32.1622 | 62.32 | 3.1 |
| 2022-10-28 | 14:58:23.16 | 135.1922 | 33.6812 | 40.63 | 3.1 |
| 2022-11-10 | 09:50:45.33 | 135.4818 | 33.8702 | 46.07 | 3.3 |
| 2022-12-16 | 03:07:17.55 | 135.8105 | 33.7022 | 34.28 | 3.2 |